

Vol.25/ 3  
JUNE, 2013

# ISRAPS Bulletin

NSRP-2013 SPECIAL ISSUE



Guest Editor  
Aloke Das

A Publication of  
Indian Society For  
Radiation & Photochemical Sciences



## ISRAPS EXECUTIVE COUNCIL 2012-2014

### *President:*

Prof. B. S. M. Rao

### *Vice-Presidents*

Dr D. K. Palit

Dr A. V. Sapre

### *Secretary*

Dr. T. K. Ghanty

### *Joint Secretary*

Prof. Sanjay Wategaonkar

### *Treasurer*

Dr. C. N. Patra

### *Executive Members*

Prof. (Smt) Samita Basu

Dr. (Smt) S. Dhanya

Dr. P. D. Naik

Dr. S. K. Sarkar

Dr. A. C. Bhasikuttan

Dr. H. N. Ghosh

Dr. (Smt.) K. I. Priyadarsini

Dr. Lalit Varshney

Prof. Anindya Datta

Dr. T. Mukherjee

Dr. P. Ramamurthy

Dr R..K. Vatsa

### *Co-opted Members*

Dr. S. Adhikari

Dr. Sudhir Kapoor

Dr. J. P. Mittal

Prof. V. Jayatirtha Rao

Dr. T. Bandyopadhyay

Dr. Manmohan Kumar

Dr D. B. Naik

Dr. Atanu Barik

Dr. Avinash Kumbhar

Dr. Sukhendu Nath

### ISRAPS Editorial Committee:

*S. K. Sarkar*

*P. N. Bajaj*

*K. I. Priyadarshini*

*Tusar Bandyopadhyay*



**INDIAN SOCIETY FOR RADIATION AND PHOTOCHEMICAL SCIENCES**

(Reg. No. 617/1985, GBBSD, Bombay; Trust No. F-10965) (Affiliated to IARR)

**Radiation & Photochemistry Division**

**Bhabha Atomic Research Centre, Mumbai - 400 085**

**Member Enrolment Form**

1. Name in Block Letters:
2. Date of Birth:
3. Highest Academic Qualification:
4. Present Position:
5. Addresses:

<b>Photograph</b>
-------------------

Office	Residence
Put your address here	Put your address here
Telephone	Telephone
Fax	Fax
E-mail	E-mail

6. Address for Correspondence: Office / Residence
7. Category of Membership Applied for: Annual / Life / corporate member
8. Remittance (DD only) payable to ISRAPS, Mumbai

Category	Fees	Admission fee	Total Amount
Annual	Rs 200/-	Rs 100/-	Rs 300/-
Life Member	Rs 1500/-	Rs 100/-	Rs 1600/-
Corporate Member	Rs 20000/-	Rs 1000/-	Rs 21000/-

9. Brief Resume of activities and research interests:
10. List of memberships of other professional bodies, if any:
11. List of prizes/awards/fellowships received, if any:
12. Number of Publications:

I agree to abide by the constitution and bye-laws, and rules and regulations of the SOCIETY.

Place:

Signature

Date

## Message from the President and the Secretary

---

Dear Members of ISRAPS and Readers,

Greetings from the Executive Council of ISRAPS!

ISRAPS has been actively involved in organizing various symposia, discussion meetings, publications of bulletin pertinent to the recent developments in the field of Radiation & Photochemistry.

In the first few months of 2013, our efforts have been focused in organizing National Symposium on Radiation & Photochemistry, which was held during March 20-22, 2013 at the Department of Chemistry, North Eastern Hill University, Shillong. The symposium was organized jointly by ISRAPS and the Department of Chemistry, NEHU. Twenty two invited talks were delivered by the leading researchers in the areas of radiation and photochemistry. Young researchers presented their work through posters, where lots of interactions were there. On behalf of the ISRAPS and the Symposium Organising Committee, we invite all those working in radiation and photochemistry and related areas to participate in the symposium and make the event a great success.

In the past few months, our efforts have been focused on the preparation for organizing Trombay Symposium on Radiation & Photochemistry to be held during January 6-9, 2014 at BARC Training School Hostel, Mumbai. More than forty invited talks are expected to be presented by leading researchers in the areas of radiation and photochemistry. On behalf of the ISRAPS and the Symposium Organising Committee, we invite all those working in radiation and photochemistry and related areas to participate in the symposium and make the event a grand success.

This is a special issue of ISRAPS Bulletin, which is being published based on the Discussion Meeting, held in April-2012 at IISER Pune. Finally, we would like to thank Dr. Alope Das, the Guest Editor of this special issue, for his enormous efforts in bringing out a rich issue of ISRAPS bulletin containing five articles on Radiation & Photochemistry. Thanks are also due to all the authors for contributing articles.

Finally, we wish to express our gratitude to all members of ISRAPS for their continued support and cooperation in carrying out the activities of the society.



**(Dr. B.S.M. Rao)**  
*President*



**(Dr. Tapan K. Ghanty)**  
*Secretary*



## *Editorial*

# ISRAPS Bulletin

A Publication of  
Indian Society for Radiation and Photochemical Sciences

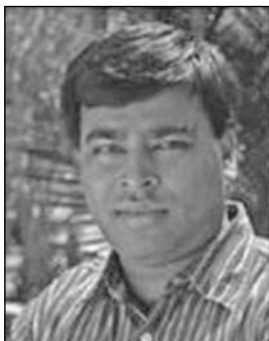
Dear ISRAPS Members

## **Spectroscopy and Dynamics**

Research on Spectroscopy and Dynamics of molecules as well as molecular processes (chemical and biological) are the key to understand the structures of the molecules and the detailed mechanism of the molecular processes. With the advent of ultrashort laser pulses (femtosecond and attosecond) and advanced spectroscopic techniques as well as theoretical tools, scientists are able to reach their dream goal on microscopic level understanding of chemical reactions (Chemical Reaction Dynamics) i.e. watching the dance (motion) of atoms as well as electrons in molecules during chemical reactions. Study of ultrafast excited state dynamics of molecules and ions also shed light on the complex mechanism of the decay of photoexcited molecular systems.

The current issue of the ISRAPS bulletin is a collection of the articles from a few speakers who presented at the Mini symposium on "Spectroscopy and Dynamics" organized by IISER (Indian Institute of Science Education and Research) Pune on April 20, 2012. Thus the themed issue of "Spectroscopy and Dynamics" of the bulletin encompasses a broad range of research areas in spectroscopy and dynamics including femtosecond dynamics of intermolecular charge transfer and exciton migration, femtosecond stimulated Raman spectroscopy to monitor chemical reaction dynamics, molecular mechanism of DNA-Drug intercalation dynamics, and laser based spectroscopic techniques to investigate photodissociation dynamics. I am sure that ISRAPS members as well as other readers will find this bulletin very much interesting by going through some of the recent research activities on Spectroscopy and Dynamics. I sincerely thank the authors for their contribution of the articles on their current research activities. I acknowledge Professor K. N. Ganesh, Director, IISER Pune for his kind support to hold this symposium at IISER Pune. I also appreciate the deliberate help of all Chemistry faculties at IISER Pune to organize this symposium.

**Aloke Das** (Guest Editor)  
Indian Institute of Science Education and Research (IISER)  
Pune, Maharashtra, India



*Alope Das obtained his M. Sc. in Chemistry from Jadaopur University in 1996 and completed his Ph. D. work under the supervision of Professor Tapas Chakraborty at the Indian Institute of Technology Kanpur in 2002. His Ph. D. thesis was on the laser spectroscopy of aromatic clusters in a supersonic jet. He went to Purdue University for doing postdoctoral work with Professor Timothy S. Zwier during 2002-2004. During his stay there, he worked on mass-selected conformation specific UV and IR spectroscopy of flexible aromatic molecules and clusters in the gas phase. Subsequently, he moved to the Advanced Light Source (ALS) of Lawrence Berkeley National Laboratory, California to work on mode-specific photoionization dynamics of complex polyatomic molecules using VUV synchrotron radiation. At the ALS, he worked since 2004-2007 under the supervision of Professor Erwin D. Poliakoff from Louisiana State University. He joined Indian Institute of Science Education and Research (IISER) Pune as an Assistant Professor in October 2007 and currently he is an Associate Professor there. His current research involves molecular level understanding of non-covalent interactions present in biomolecules and materials by studying the complexes of their building blocks using jet-cooled laser desorption REMPI (Resonantly Enhance Multiphoton Ionization) Time of Flight Mass spectrometry and quantum chemistry calculations.*

## Contents

Message from the President and Secretary, ISRAPs	1
Editor's Desk	2
Femtosecond Dynamics of Intramolecular Charge Transfer and Exciton Migration <i>Dipak K. Palit</i>	6
Femtosecond Stimulated Raman Spectroscopy: A potential tool to monitor chemical reaction dynamics <i>Ajay Jha &amp; Jyotishman Dasgupta</i>	16
Molecular Mechanism of DNA-Drug Intercalation: Structural and Dynamical Events, Role of Water and Entropy <i>Wilbee D. Sasikala and Arnab Mukherjee</i>	26
Laser Based Spectroscopic Techniques to Investigate Photodissociation Dynamics <i>Prakash D. Naik, Hari P. Upadhyaya, Awadhesh Kumar</i>	40
Hydrogen Energy	52



# Femtosecond Dynamics of Intramolecular Charge Transfer and Exciton Migration

Dipak K. Palit

*Radiation & Photochemistry Division, Bhabha Atomic Research Centre, Mumbai 400 085*

## Abstract

Three Fundamental Processes in Chemistry are breaking and forming of chemical bonds, geometrical change or conformational relaxation and exchange of electrons and protons. The driving force is induced orbital interactions leading to atomic charge redistribution, which changes the acidity or electronic affinity of the involved atoms, groups or molecules. All these processes occur with awesome rapidity. Whether in isolation or in any other phase, this ultrafast transformation is a dynamic process involving the mechanical motion of electrons and atomic nuclei. The speed of atomic motion is  $\sim 1$  km/second and, hence, to record atomic-scale dynamics over a distance of an Angström, the average time required is  $\sim 100$  femtosecond (fs). The very act of such atomic motions as reactions unfold and pass through their transition states is the focus of the field of femtochemistry. With fs time resolution we can “freeze” structures far from equilibrium and prior to their vibrational and rotational motions, or reactivity [1]. In addition, when the reaction is conducted in solution, dynamical response of the solvent molecules, such as solvent reorganization responding to charge redistribution. frictional force against configurational changes as well as specific interaction, such as intermolecular hydrogen bonding, significantly affect the course of chemical reactions [2]. In this article, we will discuss the femtosecond dynamics in two important chemical systems.

## *Dynamics of Intramolecular Charge Transfer:*

Photoinduced intramolecular charge transfer (PICT) process in molecules containing electron donor and acceptor moieties is the most well-studied phenomenon in chemical physics, because this process is responsible for the functioning of many of the photonic devices [3, 4]. Electronic communication between the chromophores based on inter-chromophoric electronic coupling, is the key for design and construction of efficient molecular electronic devices. For the development of new materials with improved user defined photo-responsive properties, it is essential to understand the photophysics and structure - function relationship in such kind of molecules.

Understanding the structure and dynamics of intramolecular charge transfer (ICT) in the excited states of numerous donor (D) - acceptor (A) substituted aromatic molecules, D-Ar-A, has been the subject of extensive theoretical and

experimental investigations. Conformational relaxation in the excited states of this class of molecules has been the standing controversial issue in the area of chemical physics. Lippert et al. (1959) observed the dual fluorescence of N,N-dimethylaminobenzonitrile (DMABN), the simplest D-Ar-A molecule, and described the ICT structure in terms of a quinonoidal and hence planar resonance structure [5]. However, Grabowski, Rokiewicz and Rettig hypothesized that the dual fluorescence of DMABN originates from the locally excited (LE) and twisted-ICT or TICT states and explained that in the TICT state, the N,N-dialkylamino group is twisted over  $90^\circ$  relative to the plane of the phenyl ring and is hence orbitally decoupled from the benzonitrile moiety following the principle of minimum overlap [6]. However, in many cases, either of these two states may be nonluminescent because of ultrafast nonradiative deactivation of this transient state.

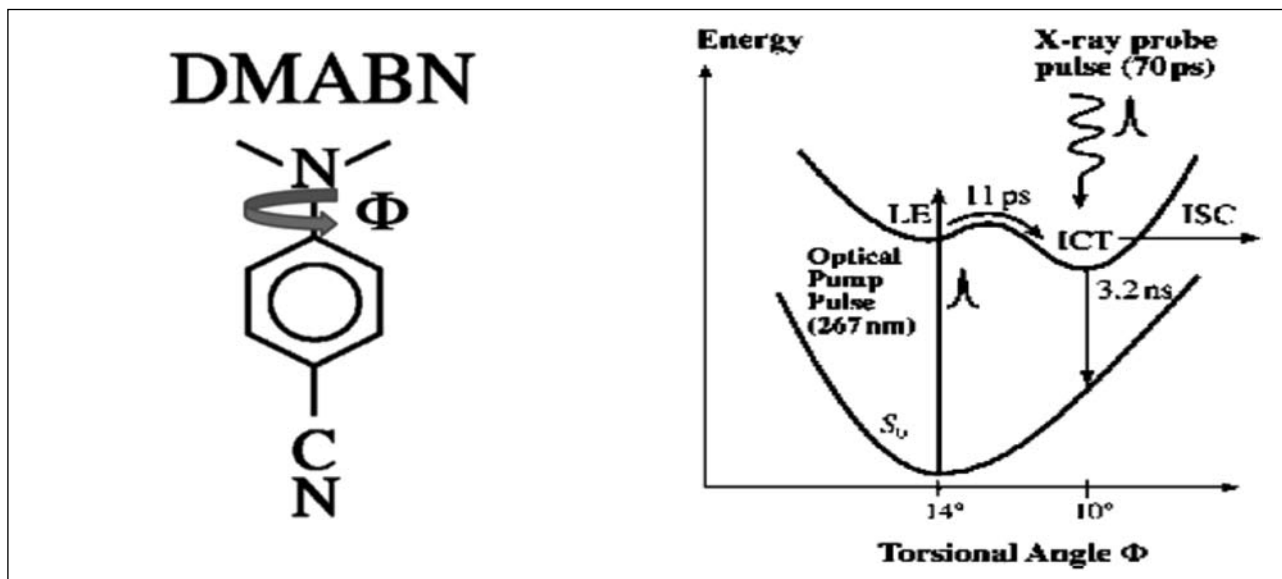


Figure 1A: Twisting of the Dimethylamino group (Grabowski, Rokiewicz and Rettig model, Ref. 6)

Figure 1B: PICT model proposed by Zachariasse and co-workers (Ref. 7).

Recently, Zachariasse and co-workers used the time-resolved x-ray spectroscopy to study the ICT dynamics of differently substituted DMABN derivatives and hypothesized the 'planar ICT (PICT) model [7, 8, 9]. They established the fact that the torsional angle of the dialkylamino group with respect to the plane of the phenyl ring of dialkyl benzonitrile decreases from  $14^\circ$  in the electronic ground state to  $10^\circ$  in the equilibrated ICT state, i.e. the ICT state has an overall planar structure. However, it has been now well established that the D-Ar-A molecules, in which the N,N-dethylaniline group, which is a strong electron donor, is coupled to a relatively weak acceptor group, e.g. the carbonyl group, the twisting of the donor group is barrierless and the formation of the dimethylaniline twisted TICT state is a favourable process [10, 11, 12].

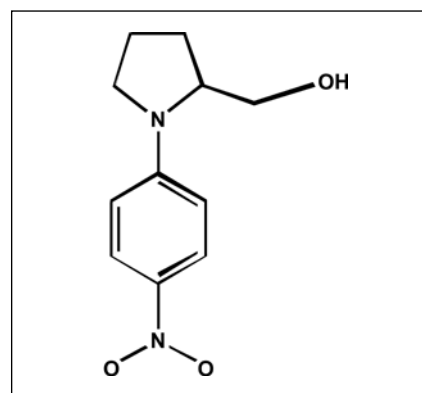
On the other hand, Hamaguchi et. al., for the first time, observed a  $\sim 120 \text{ cm}^{-1}$  of downshift for the  $\text{C}\equiv\text{N}$  stretch during the charge transfer process forming the ICT state and explained the fact by hypothesizing the configurational relaxation involving the cyano group [13]. Theoretical calculations of Sinha and Yates as well as Dobkowski et. al. predicted the charge transfer induced twisting of the nitro group,

which is a strong electron acceptor, in the excited states of nitro aromatics [14, 15]. This fact was later experimentally established by Ernsting and coworkers [16]. Sobolowski & Domcke extended the concept of conformation relaxation involving the acceptor group by hypothesizing the rehybridization-ICT (RICT):model by predicting that an excess of negative charge on the acceptor group causes a change of hybridization of the carbon or nitrogen atom rather than twisting of the amino group [17]. For the sake of completion of this discussion, we should another hypothesis proposed by Gorse and Pesquer predicting the wagging [18], but not the complete twisting of the donor group, known as WICT [19].

Further, because of the larger dipole moment of the TICT state as compared to that of the LE state, solvent reorganization is an obvious process to follow the charge transfer process. Both the intramolecular twisting and solvent reorganization or solvation dynamics are ultrafast and strongly coupled to favor the formation of the TICT state only in polar solvents. Several models have been proposed to explain the solvent influence on the intramolecular charge transfer and the twisting process [6].

**Nitro-twisting in nitroaromatics:** As discussed in the previous section, twisting of the nitro group in the excited state of nitroaniline was first considered by Sinha and Yates, who showed that the dipole moment of the excited state, in which the nitro group is twisted, is larger than that having the coplanar conformation [15]. Recently, Ernsting and coworkers investigated the relaxation dynamics of the  $S_1$  state of *p*-nitroaniline (*p*NA) using ultrafast transient absorption spectroscopic technique as well as using semiempirical theoretical calculations for the optimized geometries of both the ground and the excited states to suggest that nitro twisting is an important coordinate to induce efficient internal conversion (IC) process [20]. Following photoexcitation, the excited state evolves along this coordinate to encounter with an isoenergetic point with the ground state, where vibronic coupling facilitates very rapid IC to the ground state. Ultrafast relaxation of the  $S_1$  state of *p*NA taking place in sub-1 ps time domain has been described by the occurrence of several consecutive processes, such as vibrational relaxation, solvation, nitro twisting and internal conversion. Structure of the excited state of *p*NA with the twisted nitro group has also been established using time dependent density functional theory (TDDFT) with solvation model [17, 20]. In addition, the fact that twisting of the nitro group, and not that of the donor group, is the only conformational relaxation process taking place in the excited states of nitroaromatics has been established in the cases of *p*-nitro-dimethylaniline as well as in 7-nitro-2-aminofluorene and 7-nitro-2-dimethylaminofluorene [19]. In these molecules, nitro twisting is the process responsible for efficient nonradiative relaxation of the excited state. On the other hand, the efficient ISC process has been shown to be the major relaxation process responsible for the ultrafast nonradiative decay of the excited states of many other nitroaromatics, e.g. nitronaphthalene, nitroanthracene, nitropyrene, because of the presence of low-lying  $n-\pi^*$  state [21].

Although several reports published in recent times establish occurrence of the nitro twisting process in different donor acceptor aromatic systems, there are a few questions remain to be answered. Firstly, why does the nitro (acceptor) group twisting is important instead of the donor group? Secondly, how does it dependent on solvent polarity and viscosity? Thirdly, What are the factors favoring IC via nitro twisting in some of the nitroaromatics over the competitive ISC process? Finally, can the nitro twisting be considered a TICT process or a mere charge transfer induced twisting? Recently, we investigated the dynamics of the excited state of 1-(*p*-nitrophenyl)-2-hydroxymethyl-pyrrolidine (*p*-NPP) (scheme 1) employing subpicosecond transient absorption spectroscopic technique and quantum chemical calculations using time dependent density functional theory (TD-DFT) [22]. Our results of transient absorption experiments in different solvents of varying polarity and viscosity answer the second and third queries and the other two issues have been addressed by the theoretical calculations.



Scheme 1: Structure of 1-(*p*-nitrophenyl)-2-hydroxymethyl-pyrrolidine (*p*-NPP).

Following photoexcitation using 400 nm light, conformational relaxation via twisting of the nitro group, internal conversion (IC) and the intersystem crossing (ISC) processes have been established to be the three major relaxation pathways responsible for the ultrafast deactivation of the excited singlet ( $S_1$ ) state. Relative probability of occurrence of these processes have been shown

to be extremely sensitive to solvent polarity, because of alteration of the relative energies of the excited states both in the singlet and triplet manifolds. In the solvents of lower polarity, the ISC is predominant over the other two processes, because of near isoenergeticity of the  $S_1(\pi\pi^*)$  and  $T_3(n\pi^*)$  levels and crossing of the potential energy surfaces (PESs) of these two states, before the nitro group undergoes twisting. In the solvents of very large polarity, the energy of the  $S_1(\pi\pi^*)$  state becomes lower than that of both the  $T_3(n\pi^*)$  and  $T_2(n\pi^*/\pi\pi^*)$  states, but that of the  $T_1(\pi\pi^*)$  state and the nitro twisting and the IC processes are predominant over the ISC, and hence the triplet yield is nearly negligible. However, in the solvents of medium polarity, the PESs of the  $S_1$  and  $T_2$  states intersect and the excited state deactivation process is directed to both the IC and ISC channels and twisting of the nitro group is also an important process. Following the ISC process, the excited molecule undergoes the internal conversion and solvation in the triplet manifold. On the other hand, the IC process produces the vibrationally hot molecules with the twisted nitro group in the Franck-Condon region of the ground electronic ( $S_0$ ) state. Subsequently, reverse nitro twisting process takes place via dissipation of the excess

vibrational energy to the solvent or vibrational cooling.

Consideration of the chemical structure of *p*-NPP molecule clearly suggests the only conformational relaxation process observed in this study may involve the twisting of either the 2-hydroxymethyl-pyrrolidine group or the nitro group. Our experimental results do not distinguish between these two kinds of processes. To resolve this issue, we have carried out theoretical quantum chemical calculations using time-dependent density functional theory (TDDFT) to examine the possibility of either of these two intramolecular motions. Geometry optimized structures of the molecule reveal that in the ground state, all the three chromophoric groups, namely, 2-hydroxymethyl-pyrrolidine, the phenyl and the nitro groups, in the molecule reside on the same plane. While, in the optimized structure of the  $S_1$  state, the nitro group is twisted at a plane perpendicular to that on which the other two groups reside. The TDDFT calculations show that the excitation to the  $S_1$  state is strongly allowed (oscillator strength  $\sim 0.44$ ) with the main contribution from the transition from the HOMO to the LUMO in the gas phase as well as in the polar solvents. HOMO is largely localized on

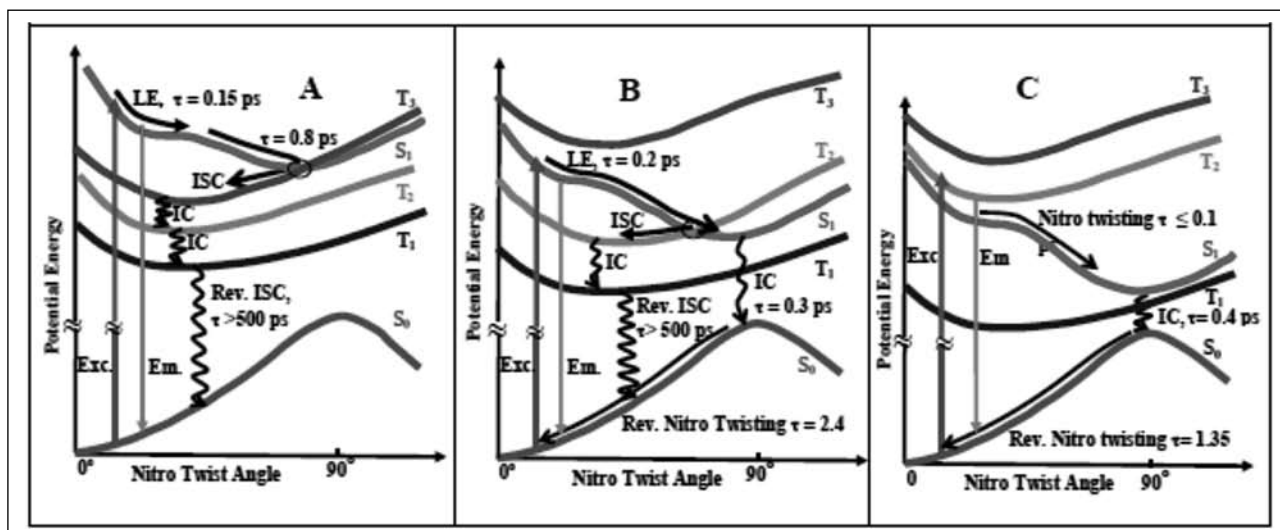


**Figure 2:** Schematic potential energy surface (PES) diagrams to illustrate the different photophysical processes occurring in the excited states of *p*-NPP in solvents of low polarity (A), medium polarity (B) and large polarity (C) (source J. Phys. Chem. A ...)

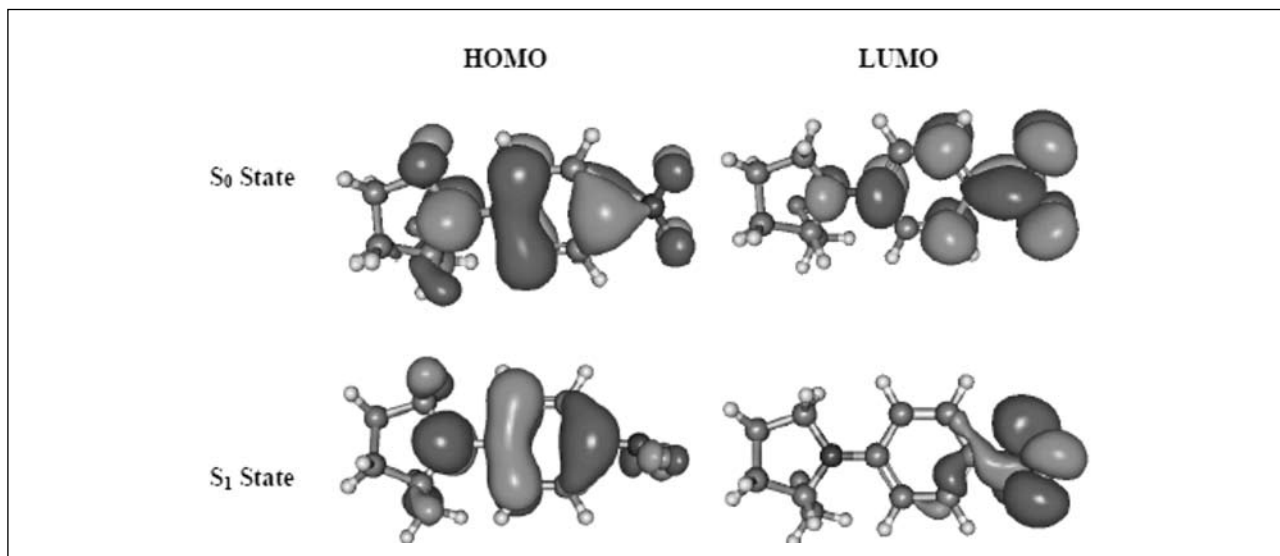


**Figure 3:** HOMO - LUMO pictures of the optimized ground and the first excited singlet states of p-NPP.

the pyrrolidine and the phenyl rings whereas the LUMO is largely localized at the nitro group. This suggests that the  $S_1$  state has a strong ICT character and explains the strong solvent polarity dependence of the absorption and fluorescence spectra.

However, considering the possibility that structural relaxation in the  $S_1$  state may occur via twisting of either the 2-hydroxymethyl-pyrrolidine group or the nitro group, we calculated the potential energy surfaces for both the ground ( $S_0$ ) and the  $S_1$  states as a function of both the twisting coordinates. Excited state potential energy surface indicated that twisting of the 2-hydroxymethyl-pyrrolidine group is associated with a large barrier ( $\sim 0.14$  eV) existing at the twisting angle of  $40^\circ$ , while that twisting of the nitro group in the  $S_1$  state is a barrierless process. Geometry optimization of the  $S_1$  state also led to a structure in which the nitro group resides on a plane perpendicular to that of the rest of the molecule. Therefore, the bulky and stronger donor group has not much effect on the conformational relaxation of the excited state of p-NPP.

**Exciton Dynamics of Zn-Phthalocyanine Nano-aggregates in Strong Hydrogen Bonding Solvents:** Molecular assemblies of

chromophores play crucial roles in the nature's most important systems, including light harvesting in photosynthesis and are important in technological applications. Phthalocyanines (PC) and metallophthalocyanines (MPC) have been established to be an important class of compounds because of their very special electronic properties and high thermal and chemical stability, which promise potential applications in wide varieties of fields [23]. PCs have strong tendency to form aggregates through self-assembly [24 - 27]. Such assemblies of PCs play important role in nonlinear optical techniques such as optical switching and optical power limiting devices, organic semiconductors etc. Most evident advantages with PCs are their large nonlinear optical coefficients and ultrafast response time [28, 29].

In the case of metal phthalocyanines, formation and characteristics of the aggregates largely depend on the central metal atom, nature of the peripheral substituents and solvent environment. Depending on all these factors, formation of both or any one of the J or H type of aggregates is possible. Zinc-phthalocyanine, namely, {zinc-2,9,16,23-tetra-tert-butyl-29H, 31H- phthalocyanine} or ZnPC (Scheme I) exists only as monomer in normal organic solvents,

like DMSO and DMF [28, 30]. Though formation of aggregates of ZnPC in aqueous medium is possible, but that needs special technique, such as microwave or reprecipitation method [28]. We have observed formation of novel aggregates of ZnPC in strong hydrogen bonding solvents. These aggregates show characteristic blue shifted absorption band as compared to the monomer absorption, revealing their H-type character. We have characterized these aggregates with the help of steady state photophysical techniques as well as the atomic force microscopy (AFM). In addition, the ultrafast dynamics in the excited states of ZnPC in the monomeric form as well as in the nanoaggregates have been investigated using sub-picosecond transient absorption spectroscopic technique [31].

In DMSO, the shape of the absorption spectrum is nearly independent of concentration and it consists of a broad Soret band or B-band in the 300 - 450 nm with the maximum at ca 352 nm and another stronger but more sharp band in the 600 - 750 nm with the maximum at ca 678 nm, which is assigned to the Q-band. The B- and the Q-bands correspond to the  $S_2 \leftarrow S_0$  and  $S_1 \leftarrow S_0$  transitions, respectively. The Q-band also consists of two vibronic bands of very low intensity. These are the typical characteristics of the monomeric ZnPC species existing in DMSO. In strong hydrogen bonding solvents, HFIP, the intensity of the B band is comparable with that of the Q band and the maximum is blue shifted as compared to that observed in DMSO, in which the Q-band is much stronger than the B-band. In addition, in HFIP, the Q-band is much broader as compared to that in DMSO. The origin of the single broad Q-band with the maximum at ca 633 nm in HFIP can be assigned to the formation of H-type nanoaggregates. Monomeric ZnPC is reasonably good fluorescent and the quantum yield of fluorescence measured in ethanol is 0.26.<sup>72</sup> Following photoexcitation using 350 nm light to the  $S_2$  state, we observe the emission from both the  $S_2$  and the  $S_1$  states with the maxima at ca 432 and 694 nm, respectively. However,  $S_2$  emission is about ten times weaker than that of the  $S_1$

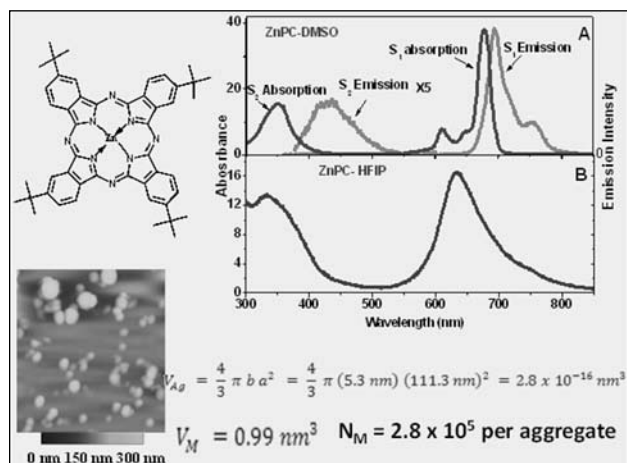


**Figure 4:** Chemical Structure of {Zinc 2,9,16,23-tetra-tert-butyl-29H, 31H-phthalocyanine} (ZnPC), Absorption and emission spectra of ZnPC monomer in DMSO and nano-aggregate in HFIP. AFM picture of ZnPC nano-aggregate in HFIP and its size analysis ( $V_{Ag}$  is the average volume of a nano-aggregate particle,  $V_M$  is the van der Waal volume of the monomer and  $N_M$  is the average number of monomer molecules in a nano-aggregate particle.)

emission. H-aggregate formed in HFIP is nearly non-fluorescent.

Transient absorption (TA) spectroscopic technique has been used to investigate the excited relaxation processes in monomeric ZnPC in DMSO. The photophysical processes involved in the relaxation of ZnPC molecule in the excited

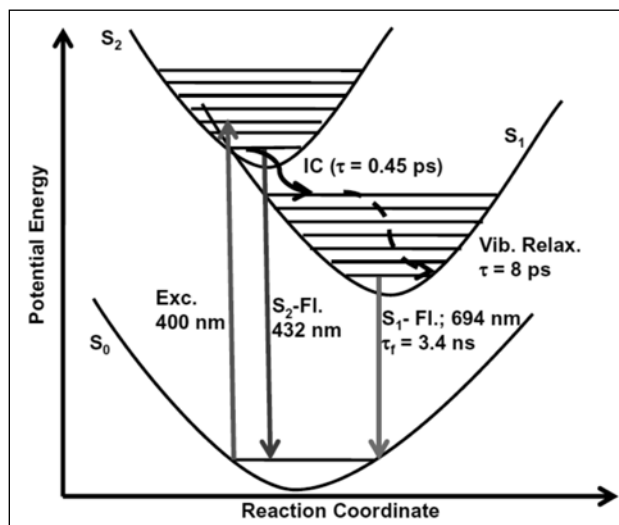


**Figure 5:** Oversimplified PES diagram depicting the excited state relaxation dynamics of ZnPC in DMSO. In this figure, an additional channel of the  $S_1$  state decay by ISC process has not been shown.

states following its photoexcitation to the  $S_2$  state are shown in Figure 5. The  $S_2$  state decays with the lifetime of about 0.4 ps to populate the higher vibrational levels of the  $S_1$  state. The excess vibrational energy is redistributed among the different intramolecular vibrational modes in the  $S_1$  state and / or dissipated to the solvent modes with a lifetime of about 8 ps. The lifetime of the vibrationally relaxed  $S_1$  state is about 3.4 ns.

TA spectrum of ZnPC nano-aggregates in HFIP or water is characterized by a strong and very broad bleaching band and two weak ESA bands, which follow the similar decay dynamics. The excited state dynamics of the nanoaggregates are nonexponential and the temporal profiles could be fitted well with three exponential decay functions with the similar lifetimes of the components through the entire wavelength region. The excited state of the ZnPC nanoaggregate shows much faster recovery to the ground state (within about 100 ps) as compared to that of the monomer, measured in DMSO. The faster dynamics can be assigned to the new nonradiative energy relaxation channels that become effective upon aggregation. The photophysical processes involved in the relaxation of the excited states of ZnPC nano-aggregates in HFIP have been schematically represented in Figure 7.

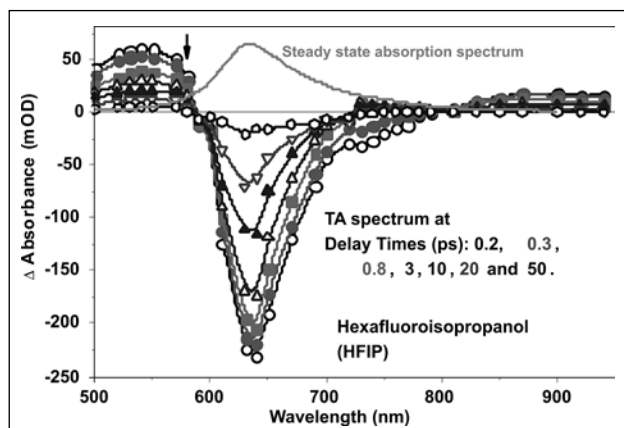


**Figure 6:** Time-resolved TA spectra recorded following photoexcitation of  $5 \times 10^{-5} \text{ mol dm}^{-3}$  of ZnPC in HFIP using 400 nm light.

Study of excitation density dependence of the lifetimes of three components reveals that the lifetimes of two ultrafast components increase significantly with decrease in excitation density, while the lifetime of the longest component ( $\sim 27$  ps) is nearly independent of the excitation density (see Table 1). The later has been assigned to that of monomeric  $S_1$ -exciton. The excitation density dependence of the other two lifetimes arises due to nonexponential decay of the  $S_1$ -excitons because of time-dependent bimolecular annihilation reaction.

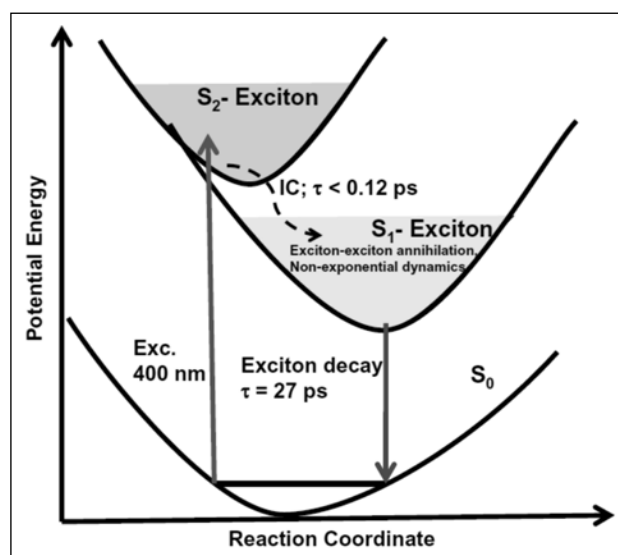


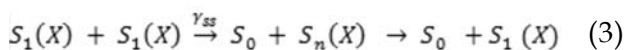
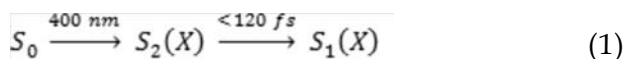
**Figure 7:** Oversimplified PES diagram depicting the excited state relaxation dynamics of ZnPC nanoaggregate

**Table 1: Intensity dependence of the lifetimes of three components measured at 630 nm.**

Excitation density ( $\text{GW}/\text{cm}^2$ )	$\tau_1$ (ps)	$\tau_2$ (ps)	$\tau_3$ (ps)
7.64	0.25	2.6	21
5.0	0.48	5.8	25
2.5	0.6	7.8	24
0.93	0.89	10.8	26

We followed the approach of Paillotin et. al. [32] to analyse the exciton dynamics. We write the following reaction scheme for the creation and decay of the  $S_1$ -exciton

(which has been represented as  $S_1(X)$  in the following equations) in ZnPC nanoaggregates in HFIP:



At low excitation density, when the number density of  $S_1$ -excitons produced in an aggregation unit is such that the distance between two of them is larger than a certain diffusion radius, say  $R_a$  (vide infra), the decay of the  $S_1$ -exciton is mono-exponential with the rate constant of  $k_s$  (reaction 2). However, higher excitation densities produce larger number densities of the  $S_1$ -excitons and when two or more  $S_1$ -excitons are within the diffusion radius  $R_a$ , they can migrate into the vicinity of one another and undergo exciton - exciton annihilation reaction, as represented by the reaction (3). Reaction 3 represents a bimolecular fusion process in which a  $S_1$ -exciton transfers its energy to another neighboring  $S_1$ -exciton creating a higher energy  $S_n$ -exciton, which decays nonradiatively to regenerate the  $S_1$ -exciton.

Therefore, we can write a kinetic equation of a continuum model for bimolecular quenching of excitons (Equation 4) assuming the fact that the rate of formation of the  $S_1$ -exciton is much faster as compared to the decay rates:

$$\frac{d[S_1(X)]}{dt} = -k_s[S_1(X)] - \frac{1}{2} \gamma_{ss} [S_1(X)]^2 \quad (4)$$

$$\text{or, } \frac{d[S_1(X)]}{dt} / [S_1(X)] = -k_s - \frac{1}{2} \gamma_{ss} [S_1(X)] \quad (5)$$

Here  $[S_1(X)]$  represents the number of  $S_1$ -excitons in an aggregate or domain. The kinetic measurements yield the change of  $\Delta[A]$  vs time,

i.e.,  $d[\Delta A] / dt$ . At the low degrees of excitation used in our experiments,  $\Delta[A]$  is directly proportional to density of excitations. Thus we can write,

$$\frac{d\Delta A}{dt} / \Delta A = -k_s - \frac{1}{2} \gamma'_{ss} \Delta A \quad (6)$$

Here  $\gamma'_{ss}$  is related to  $\gamma_{ss}$  by equation 7,

$$\gamma_{ss} (\text{cm}^3 \text{ s}^{-1}) = \frac{\gamma_{ss}}{[S_1(X)]/V_{Ag}} = \frac{\gamma_{ss}}{\rho(X)} \quad (7)$$

$V_{Ag}$  is the volume of a nanoaggregate ( $2.75 \times 10^{-16} \text{ cm}^3$ ) and  $\rho(X)$  is the excitation density or the number of excitons generated in unit volume of the aggregate. Now, we may obtain the rate constant for the monomolecular decay rate constant,  $k_s$  from the intercept and the annihilation rate constant  $\gamma_{ss}$  as the slope of a plot of  $[(d\Delta A / dt) / \Delta A]$  vs  $\Delta A$  [32].

In Figure 8A, we have shown three of such plots for the transient bleach signals recorded at 630 nm using different excitation densities (includes the lowest, the medium and the highest excitation densities). We find that at low  $\Delta A$  values, all three curves are parallel to the x-axis, which represents the annihilation-free conditions at low excitation densities and that the monomolecular decay rate  $k_s$  can be obtained from the intercept. From the intercept value of  $3.7 \pm 0.5 \times 10^{10} \text{ s}^{-1}$ , the lifetime of the annihilation free  $S_1$ -exciton ( $\tau$ ) is determined as  $27.4 \pm 4 \text{ ps}$ . This value agrees well with the value of  $\tau_3$  (Table 1), which is independent of excitation density of photoexcitation.

However, at higher  $\Delta A$  values, the slopes of the curves are larger and the slope increases as the excitation density or the number density of  $S_1$ -excitons or  $\rho(X)$ , is increased. This suggests the occurrence of the annihilation process at higher excitation densities. Moreover, the curves obtained by  $(d\Delta A / dt) / \Delta A$  vs  $\Delta A$  plot indicate an onset of annihilation reaction (marked by an arrow in Figure 8A). The onset

of annihilation corresponds to the value of  $\Delta A \sim 0.015$  for all three curves and this corresponds to the excitation density of  $4.35 \times 10^{12}$  per pulse or  $2.12 \times 10^4$  photons absorbed per aggregate. This is the excitation density corresponding to one exciton created within the annihilation reaction radius,  $R_a$ .

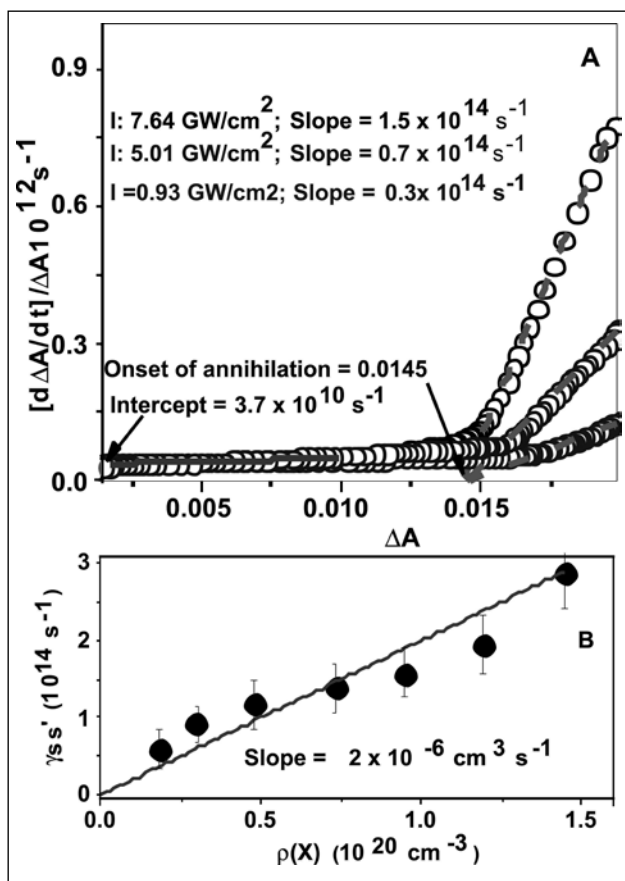


**Figure 8:** (A)  $[(d\Delta A/dt)/\Delta A]$  vs  $\Delta A$  plot at three different excitation intensities. (B) plot of  $\gamma_{ss}$  vs  $\rho(X)$  as per equation 6. Error associated with the values of the slopes of the curves is about 20%.

Now the slopes of the curves at the higher  $\Delta A$  region provide the values of  $\gamma_{ss}$  at different excitation densities (insets of Figure 8A) and the larger slope of the curves at higher excitation densities suggest stronger annihilation reaction. In Figure 8B, we have plotted  $\gamma_{ss}$  vs  $\rho(X)$  (Equation 6) and the slope of the linear curve provides the value of the annihilation rate constant ( $\gamma_{ss}$ ) as  $2.0 \pm 0.4 \times 10^{-6} \text{ cm}^3 \text{ s}^{-1}$ .

The annihilation rate constant,  $\gamma_{ss}$ , can be used to estimate the excitation migration parameters for diffusive migration controlled exciton – exciton annihilation reaction.<sup>53, 80, 81</sup>

$$\gamma_{ss} = 8\pi D R_a \quad (8)$$

And

$$\tau_{hop} = \frac{R_a^2}{D} \quad (9)$$

Where 'D' is the excitation diffusion coefficient and  $\tau_{hop}$  is the hopping time, assuming that the excitons are localized and moving mainly by an incoherent hopping process. Now considering the value of the onset of annihilation reaction is  $2.12 \times 10^4$  photons per particle or aggregate and the volume of the aggregate,  $V_{Ag} = 2.75 \times 10^5 \text{ nm}^3$  (vide supra), the value of  $R_a$  could be estimated as 1.84 nm or  $1.84 \times 10^{-7} \text{ cm}$ . Therefore, we calculate the diffusion coefficient (D) to be about  $0.43 \text{ cm}^2 \text{ s}^{-1}$  or  $4.3 \times 10^{-5} \text{ m}^2 \text{ s}^{-1}$  using equation 9 and the value of  $\tau_{hop}$  to be  $7.8 \times 10^{-14} \text{ s}$  or 78 fs. This rough estimation, which gives an upper limit for  $\tau_{hop}$ , suggests ultrafast exciton dynamics in the H-aggregate of ZnPC. The large hopping rate ( $k_{hop} = \tau_{hop}^{-1} \sim 1.3 \times 10^{13} \text{ s}^{-1}$ ) obviously can be correlated with a very high transfer rate, which should be correlated with the small distances between molecules and the strong excitonic interaction. Based on these values, we can estimate the diffusion length, L, for the  $S_1$ -exciton, which is defined as [33],

$$L = \sqrt{\left(\frac{dR_a^2}{\tau_{hop}}\right)} \quad (10)$$

where the coordination number,  $d = 6$  for three dimensional structures. Using the value of  $\tau$  as 27.4 ps, the value of L can be estimated to be at least 85 nm. This large value of exciton diffusion length indicates that the exciton migrates over a large domain containing several hundred thousand ZnPC molecules. Larger diffusion rate and longer diffusion length can be tentatively attributed to an improvement

of the columnar continuity through hydrogen bonding bridges formed by the solvents between two phthalocyanine molecules in a hexagonal column.

**Acknowledgement:** My sincere acknowledgements are due to Shri Rajib Ghosh and Ms. Snehal Kakade, who are the co-authors of the original papers, for their valuable contribution in the work presented here.

## References

- Ahmed H. Zewail, 'Femtochemistry: Past, present, and future', *Pure Appl. Chem.*, 72 (2000) 2219-2231.
- James T. Hynes (1985). "Chemical Reaction Dynamics in Solution". *Ann. Rev. Phys. Chem* 36: 573-597.
- M. Kasha, In *Molecular Electronic Devices*; F. L. Carter, R. E. Siatkowski, and H. Wohltjen, Eds.; Elsevier Science Publishers: New York, 1988; p 107-121.
- S. Kim, J. Seo, H. K. Jung, J. J. Kim and S. Y. Park, *Adv. Mater.* 17 (2005) 2077.
- E. Lippert, W. Lüder, F. Moll, W. Nägele, H. Boos, H. Prigge, and I. Seibold-Blankenstein, *Angew. Chem.* 73 (1961) 695.
- Z. R. Grabowski, K. Rotkiewicz, and W. Rettig, *Chem. Rev.* 103 (2003) 3899.
- S. Tretchert and K. A. Zachariasse *J. Am. Chem. Soc.* 126 (2004) 5593.
- K. A. Zachariasse, S. I. Druzhinin, W. Bosch and R. Machinick, *J. Am. Chem. Soc.* 126 (2004) 1705.
- S. I. Druzhinin, P. Meyer, P. D. Stalke, M. Noltemeyer and K. A. Zachariasse, *J. Am. Chem. Soc.* 132 (2010) 7730.
- C. Singh, B. Modak, J. A. Mondal and Dipak K. Palit, *J. Phys. Chem. A* 115 (2011) 8183-8196.
- J. A. Mondal, H. N. Ghosh, T. K. Ghanty, T. Mukherjee and Dipak K. Palit, *J. Phys. Chem. A* 110 (2006) 3432-3446.
- R. Ghosh and D. K. Palit, *Phys. Chem. Chem. Phys.* (2012) (communicated).
- H. Hamaguchi and M. Hashimoto, *M. J. Phys. Chem.* 99 (1995) 7875.
- Dobkowski et. al. *J. Luminescence* (1989).
- H. K. Sinha and K. Yates, *K. J. Chem. Phys.* 93 (1990) 7085; *Can. J. Chem.* 89 (1991) 550.
- V. M. Farztdinov, R. Schanz, S. A. Kovalenko and N. P. Ernsting, *J. Phys. Chem.* 104 (2000) 11486.
- A. L. Sobolewski and W. Domcke, *Chem. Phys. Lett.* 250 (1996) 428; 259 (1996) 119.
- Gorse and Pesquer, *J. Phys. Chem.* 99 (1995) 4039.
- Palit et. al. *J. Phys. Chem. A (Letters)*, 111 (2007) 6122-6126.
- S. A. Kovalenko, R. Schanz, V. M. Farztsinov, H. Hening and N. P. Ernsting, *Chem. Phys. Lett.* 312 (2000), 312.
- C. L. Thomsen, J. Thogersen and S. R. Keiding, *S. R. J. Phys. Chem. A* 102 (1998) 1062.
- R. Ghosh and D. K. Palit, *J. Phys. Chem. A* 116 (2012) 1993-2005.
- M. Fournier, C. Pe'pin, D. Haude, R. Ouellet and J. E van Lier, *Photochem. Photobiol. Sci.* 3 (2004) 120-126.
- C. Nitschke, S. M. O'Flaherty, M. Kroll and W. J. Blau, *J. Phys. Chem. B*, 108 (2004) 1287-1295.
- E. V. Keuren, A. Bone and C. Ma, *Langmuir*, 24 (2008) 6079-6084.
- C. Farren, S. FitzGerald, A. Beeby and M. R. Bryce, *Chem. Commun.* 2002, 572- 573.
- Y. Tamaki, T. Asahi, H. Masuhara, *J. Phys. Chem. A* 106 (2002) 2135-2139.
- S. V. Rao, N. Venkatram, L. Giribabu and D. N. Rao, *J. Appl. Phys.* 105 (2009) 0531091-105391-6.
- D. Chaudhuri, D. Li, Y. Che, E. Shafran, J. M. Gerton, L. Zang and J. M. Lupton, *Nano Lett.* 11 (2011) 488-492.
- L. Howe and J. Z. Zhang, *J. Phys. Chem. A.* 101 (1997) 3207-3213.
- S. Kakade, R. Ghosh and D. K. Palit, *J. Phys. Chem. C* 116 (2012) 15155 - 15166.
- G. Paillotin, C. E. Swenberg, J. Breton and N. E. Geacintov, *Biophys. J.* 25 (1979) 513-533.
- E. J. W. List, U. Scherf, K. Müllen, W. Graupner, C. -H. Kim and J. Shinar, *J. Phys. Rev. B* 66 (2002) 235203(1-5).



**Dipak K. Palit** joined then Chemistry Division, Bhabha Atomic Research Centre, Mumbai, in 1983 after completion of the one year Orientation course of the BARC Training School in Chemistry Discipline. Since then he has been associated with the photo & radiation chemistry group of BARC. Over the years he has developed the ultrafast time-resolved spectroscopic techniques to study the dynamics of light and high energy radiation induced chemical processes in condensed phase. In recognition to his work in this field, he has been awarded L. M. Yeddanapalli Memorial Award of Indian Chemical Society (1999), Bronze Medal of the Chemical research Society of India (2001) and the Homi Bhabha Award for Science & Technology and Gold Medal of DAE, India (2002). He is a Fellow of the Indian Academy of Sciences (F. A. Sc.) and the National Academy of Sciences of India (F. N. A. Sc.).

# Femtosecond Stimulated Raman Spectroscopy: A potential tool to monitor chemical reaction dynamics

Ajay Jha & Jyotishman Dasgupta\*

Department of Chemical Sciences, Tata Institute of Fundamental Research, Mumbai-400005, India

\*Email: dasgupta@tifr.res.in

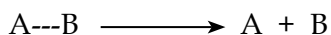
## Abstract

Tracing nuclear trajectories to follow chemical reaction dynamics can give mechanistic insight that in turn can be capitalized to manoeuvre them. Femtosecond stimulated Raman spectroscopy (FSRS) has revolutionized the field of ultrafast structural dynamics due to its high spectral ( $\sim 10 \text{ cm}^{-1}$ ) and temporal ( $\sim 50 \text{ fs}$ ) resolution. This three-pulse nonlinear spectroscopic technique gives coherent Raman signals, free from fluorescence background with heterodyne detection along the probe pulse direction. This enables one to monitor vibrational dynamics in the excited electronic states through Raman spectroscopy even in cases of highly fluorescent molecules. This chapter describes briefly the technical details of FSRS, and then goes on to describe its utilization to probe the multidimensional potential energy landscape associated with photoinduced electron transfer (ET) reactions.

## Introduction

Chemists have always dreamt of achieving complete thermodynamic and kinetic control over photochemical reactions to achieve desired products. In order to attain this control, we need to have a complete understanding of the reaction mechanism which requires exquisite mapping of the reaction trajectory over a complex potential energy landscape. Studying reaction pathways in variety of complex molecular systems has been one of the major areas of research in the past few decades. Different kinds of photochemical reactions ranging from electron transfer (ET) in photochemical devices<sup>1</sup> to the charge separation processes in photosynthetic machinery of plants,<sup>2</sup> have extensively been studied by the researchers using various spectroscopic tools to gain valuable insight on the reaction trajectories.

To illustrate the complexities of the trajectory, consider a case of simple chemical reaction involving a fundamental bond breaking step as shown below:



This reaction can easily be tracked by monitoring the changes in stretching frequency of A---B bond. In this case, the reaction coordinate is purely the interatomic distance between atoms A and B. But for chemical reactions like ET, the reaction coordinate may have contribution from many concerted or sequential nuclear displacements. Especially ultrafast ET reactions often results from a highly optimized geometry of Donor-Acceptor which precise tracking of nuclear configurations via both the localized and global molecular motions. Since molecular vibrations form the basis of such motions, vibrational spectroscopy can quantify reactive nuclear displacements thereby providing a detailed picture of structural changes that contribute towards the chemical reaction coordinate.

With the advent of modern ultrafast lasers systems<sup>3</sup> and advanced detector technology, it has been possible to study these ultrafast processes using transient electronic spectroscopic techniques like fluorescence upconversion and transient pump-probe spectroscopy.<sup>1,4,5</sup> These techniques have given wealth of information regarding timescales of ET and nature of states.

However, due to the inherent linewidths of electronic transitions in the condensed phase, transient absorption and fluorescence measurements are relatively insensitive to subtle changes in molecular structure during reactions. Vibrational transitions on the other hand have advantage of greater spectral resolution and along with ultrahigh sensitivity towards bond making or breaking. This makes vibrational spectroscopy an ideal tool for mapping structural dynamics during course of a reaction.

Time resolved vibrational techniques like CARS,<sup>6</sup> ISRS,<sup>7</sup> Femtosecond pump-probe IR,<sup>8,9</sup> multidimensional techniques based on vibrational echoes<sup>10</sup> etc. have been used to map the multidimensional potential energy landscapes. Although they are giving substantial information still suffer from either the time resolution, frequency range and /or available bandwidth.

Over the last decade, a new spectroscopic tool named FSRS (femtosecond stimulated Raman spectroscopy) has been developed by Yoshizawa, Mathies and others that can monitor the reaction dynamics in condensed phase without having above mentioned constraints.<sup>11-14</sup> FSRS with its high time ( $\sim 50$  fs) and spectral resolution ( $10 \text{ cm}^{-1}$ ), and frequency range ( $2000 \text{ cm}^{-1}$ ) has shown great potential to capture dynamical vibrational structural information.

The schematic for FSRS is depicted in Figure 1. FSRS pulse timing diagram shows it is a three pulse ultrafast technique involving two femtosecond pulses and one picosecond pulse. A femtosecond actinic pump drives the photochemistry in the reactant molecule(s). To interrogate the structure at different points in the reaction phase space, two more pulses are utilized: a picosecond narrow band Raman pump and another femtosecond broad band probe pulse with a given time delay,  $\Delta T$  after excitation with actinic pump pulse. A combination of Raman pump and probe pulses creates vibrational coherence between  $|n\rangle$  and the  $|n+1\rangle$  states in the excited state. During free induction decay of this coherence, another field interaction with the Raman pump pulse leads to the emission of the Stokes' shifted Raman photons in the probe direction that makes FSRS a self-heterodyned technique.<sup>15</sup> Time resolution of the experiment is given by the cross-correlation of the actinic and probe pulses measured by optical Kerr effect. Rapid data acquisition time and excellent signal to noise are added advantage to this technique. Stimulated nature of detection makes signals free from incoherent fluorescence background. These unique advantages of FSRS has been used to acquire vibrational structural information in various systems, including demonstration of isomerization reaction coordinate in rhodopsin,<sup>16</sup> bacteriorhodopsin,<sup>17,18</sup> phytochrome<sup>19</sup> and the excited state proton transfer reaction in GFP.<sup>20</sup> These studies have justified FSRS as a potent structural tool for probing chemical reaction dynamics.

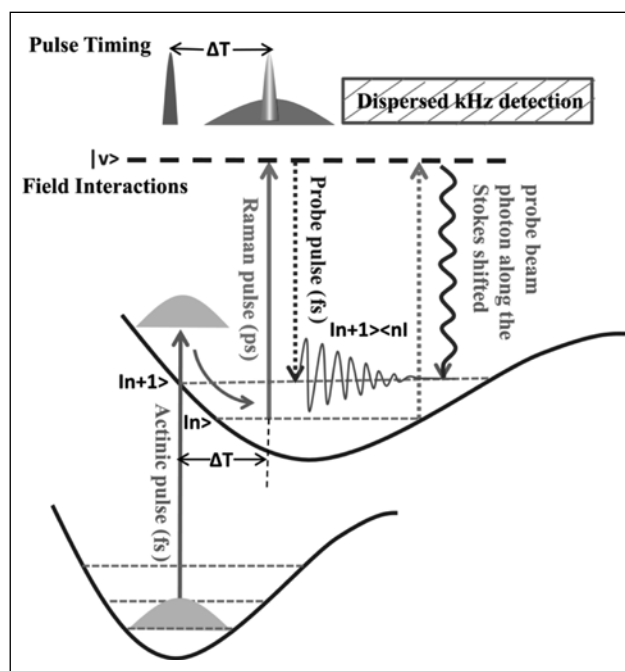
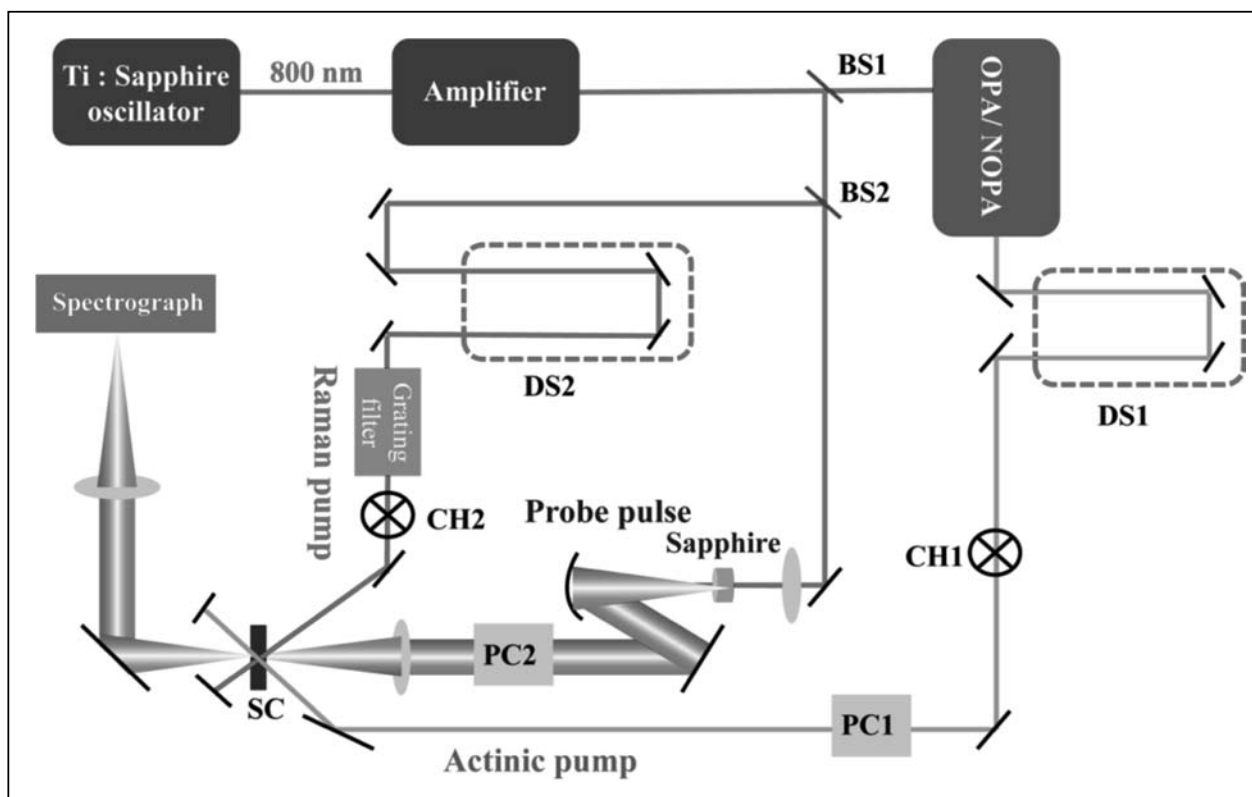


Figure 1. Concept of FSRS: A femtosecond actinic pulse (light blue pulse) creates an excited state population. A picosecond narrowband Raman pulse (red pulse) and a femtosecond broadband probe pulse (rainbow coloured pulse) creating vibrational coherence in the excited state which is detected in the form of Raman photon after another interaction with the Raman pulse.



**Figure 2.** Schematic representation of FSRS system detailing essential optical components. The fundamental of the laser is split into three pulses as shown above. The picosecond Raman pump is obtained by a grating filter while the probe is generated by continuum generation in the sapphire plate (CH = chopper; BS = beam splitter; DS = delay stage; PC = prism compressor and SC = sample cell).

### FSRS implementation

Since FSRS is a femtosecond time-resolved technique, the optical pulses can be derived from any commercial amplified Ti:sapphire laser system. The fundamental pulse at 800 nm out of a regenerative amplifier is divided up into three portions to produce pulses which are finally focused on the sample to implement the FSRS scheme (shown in Figure 2). We describe the three pulses and the detection scheme needed for the time-resolved FSRS process in subsequent sections.

**Actinic Pulse:** The actinic pump pulse (~25 fs) can be generated using a conventional noncollinear optical parametric amplifier (NOPA) if the fundamental source is ~100 fs amplifier system. Through the mixing of a 400 nm pump pulse with the sapphire-generated continuum

seed pulse in a nonlinear beta barium borate (BBO) type-II crystal<sup>21</sup>. The mixing conditions can be varied via both the temporal overlap between the beams and the crystal angle to tune the color from 470 to 730 nm with varying bandwidths. After the NOPA generation, the actinic pulse is compressed down to 25–35 fs using a prism compressor. Recently with the advances in laser technology, stable commercial OPA's (shown in Figure 2) have also become popular choice for generating the actinic pulse.

**Probe pulse:** The weakest of the three pulses is the broadband continuum pulse generated from a sapphire plate also known as the probe pulse in this experiment. The probe pulse initiates and ultimately carries the stimulated Raman photon. Using a requisite filter and a prism compressor, a tunable 20 fs probe pulse can be used for

Stokes or anti-Stokes measurements. The pulse compression is imperative to get good stimulated Raman spectra.

*Raman pump pulse:* The Raman pump pulse form the backbone of this technique and has to be generated with highest efficiency as possible. The cheapest way to generate it would be to spectrally filter the broadband femtosecond fundamental and compress to derive a narrowband picosecond pulse from suitable grating arrangement. This has been the popular choice due to the ease of generation although it is a highly inefficient process. However, for the observation of both resonance enhancement and collection of weak intensities of important low-frequency modes it is advisable to generate a tunable Raman pump. The technology of generating tunable picosecond pulses from a femtosecond source has recently been developed by various groups. Ideas range from implementation of second harmonic bandwidth compressor for generation of blue Raman lines from 370-440 nm<sup>12</sup> to usage of dual-stage NOPA for narrow bandwidth amplification for 470-650 nm lines.<sup>22</sup> It will be evident through our illustrative examples how the ability to resonantly enhance the vibrational signatures ultimately leads to FSRS detection of molecules with small Raman cross-sections.

*Dispersed detection:* The most critical issue in any form of Raman spectroscopy is the development of an efficient data collection scheme. In FSRS the detection is not time-resolved and is typically done using a grating spectrograph which disperses the probe onto a diode array or a CCD detector. Typically most of the experiments reported to date have used dual photodiode arrays (PDA) which are ideally suited for the collection of large photon fluxes ( $10^9$ – $10^{11}$  counts) due to large well depth.<sup>11</sup> However due to the poor signal-to-noise ratio of PDA's, multiple averages have to be carried out, which reduces the duty cycle of detection process. Recently due to the development of fast and superior CCD technology, this methodology now can easily be implemented to allow detection of low-noise

unsaturated spectra at kHz repetition rates. A single FSRS spectrum which is obtained by normalizing the Raman pulse-on with the Raman pulse-off data can now be recorded within 2 ms while keeping sample exposure limited to only a few picoseconds. As an example, Raman spectrum of cyclohexane with  $S/N \sim 10^3$  can be obtained within a second under optimized beam geometry conditions.

### Applications of FSRS in Electron Transfer Reactions

There have been excellent reviews written on FSRS describing the theoretical<sup>25</sup> and experimental details.<sup>15, 23-24</sup> This chapter has been written with the aim of describing how FSRS has been used to study one of the most fundamental chemical reactions, ultrafast electron transfer (UFET). Implementing spatial and temporal control on ET reactions is critical for photocatalytic applications and molecule-based devices such as solar cells. Ultrafast ET reactions are special in the aspect that here solvents motions are frozen in the reaction timescales.<sup>26</sup> Thus, to clearly enunciate the mechanistic aspects of ultrafast ET reactions, it is essential to follow the structural changes in electron donor and acceptor molecules that drive these electron transfer reactions. To illustrate the potential of FSRS towards understanding of these ultrafast processes three recent examples from literature has been taken: (1) Intermolecular ET between pyromellitic dianhydride (PMDA) and hexamethylbenzene (HMB); (2) Intramolecular ET reaction in 4-(dimethylamino)benzonitrile and (3) Interfacial ET reactions involving coumarin dye attached to TiO<sub>2</sub>. These three examples will illustrate the potential of FSRS towards understanding of these ultrafast processes

#### 1. Structural Dynamics of Ultrafast Intermolecular Electron Transfer

Non-covalent complexes exhibiting fast and efficient ET processes have been long desired by chemists for constructing supramolecular architectures with tunable functionalities. Therefore, it is important to unravel the basic

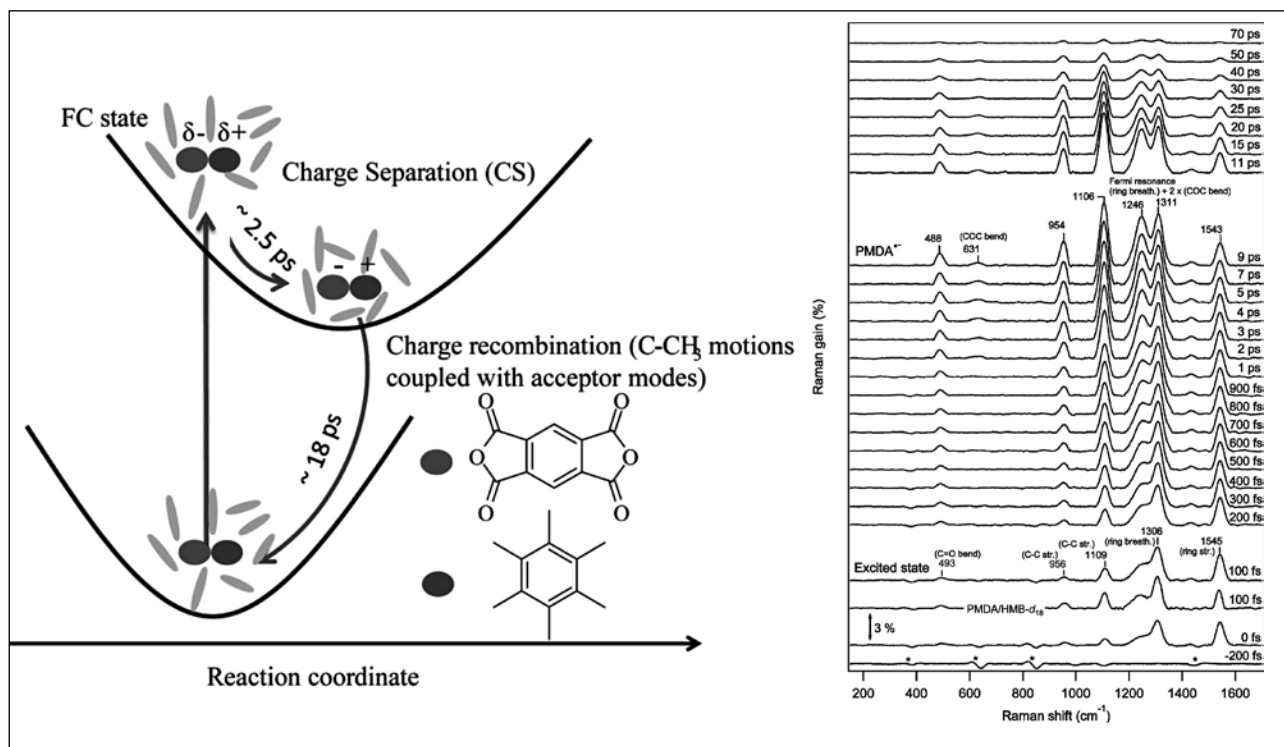


Figure 3. Left: Model diagram representing CT timescales in case of PMDA/HMB complex in ethylacetate. Right: FSRS spectra of PMDA/HMB complex in ethylacetate after excitation at 400 nm and Raman pump at 625 nm. Figure taken from reference 32. (permission required)

design rules for such ET reactions. Motivated by such principles 1:1 non-covalent complex of donor-acceptor as been extensively studied by various experimental and theoretical groups. PMDA is a typical organic electron acceptor that gives a new absorption band ascribed to the CT complex when mixed with electron donors like HMB. Mataga and co-workers found non-Marcus behaviour in charge recombination of the PMDA/donor complexes.<sup>27-29</sup> Experimental observations proposed linear decrease of log of the charge recombination rate with free energy gap function which was interpreted as arising from FC vibrational overlap between high-frequency modes of the contact ion pair (CIP) and the ground state.<sup>30-31</sup> But there was no experimental observation of any vibrational structural dynamics. For direct experimental observation of these dynamical molecular perspectives of charge transfer process, one needs to pursue the structural information by following

the inter- and intra-molecular vibrations that modulate the electronic coupling and correlated Franck-Condon (FC) factors.

Fujisawa et. al. have used FSRS to monitor the structural dynamics of non-covalent charge transfer (CT) complex of pyromellitic dianhydride (PMDA) and hexamethylbenzene (HMB) in two different solvents, ethylacetate and acetonitrile.<sup>32</sup>

Spontaneous Raman spectrum of the PMDA/HMB complex in ethylacetate demonstrated weak resonance enhancement of PMDA modes in comparison to HMB upon excitation into the CT absorption band indicating limited structural changes in PMDA relative to that of HMB. Observed Raman peaks of CT complex at 455, 1301 and 1575  $\text{cm}^{-1}$  were assigned to the C-CH<sub>3</sub> deformation, ring breathing stretch and ring stretch of the donor HMB respectively. Time-resolved FSRS of the PMDA/HMB complex in

ethylacetate showed splitting of ring breathing mode at 1246/1311  $\text{cm}^{-1}$  and an increase in the intensity of the C-C stretch at 1106  $\text{cm}^{-1}$ . No change in Raman bands during charge recombination (CR) suggested that the intracomplex structural rearrangement is completed during charge separation (CS). Kinetic analysis showed that the time constants for the CS and CR are  $2.5 \pm 0.2$  ps and  $18.9 \pm 1.3$  ps, respectively. Deuterium substitution of the donor (HMB- $d_{18}$ ) did not affect the charge separation but showed kinetic isotope effect (KIE) of 1.4 for the CR, indicating coupling of the methyl hydrogen motions with the acceptor modes to moderate charge recombination. Similar observations for KIE were seen for FSRS of the CT complex in acetonitrile except for changes in the time constants for CS ( $\sim 0.5$  ps) and CR ( $5.3 \pm 0.4$  ps). KIE of 1.4 has been assigned to have major contribution from C-CH<sub>3</sub> deformation which exhibited a 33  $\text{cm}^{-1}$  isotope shift and large FC

displacements. This study thus exemplifies the power of FSRS to get a more direct insight into the structural dynamics and generates testable hypothesis involving role of in-plane bends. Additionally it also forces one to think of low-frequency motions which could be coupled to such transitions but are absent in the dataset.

## 2) Charge Transfer Dynamics in Intramolecular Electron Transfer

Intramolecular charge transfer reaction is one of the most studied photochemical reaction in artificial molecular systems,<sup>33-36</sup> and it is representative of the challenges the ET reaction presents to the chemists from the perspective of gaining control over its fate via *through space* or *through bond* transfers. 4-(dimethylamino) benzonitrile, DMABN represents a classical example in which the donor amine group is strongly coupled *through bond* to the nitrile group in the para position. On absorption of

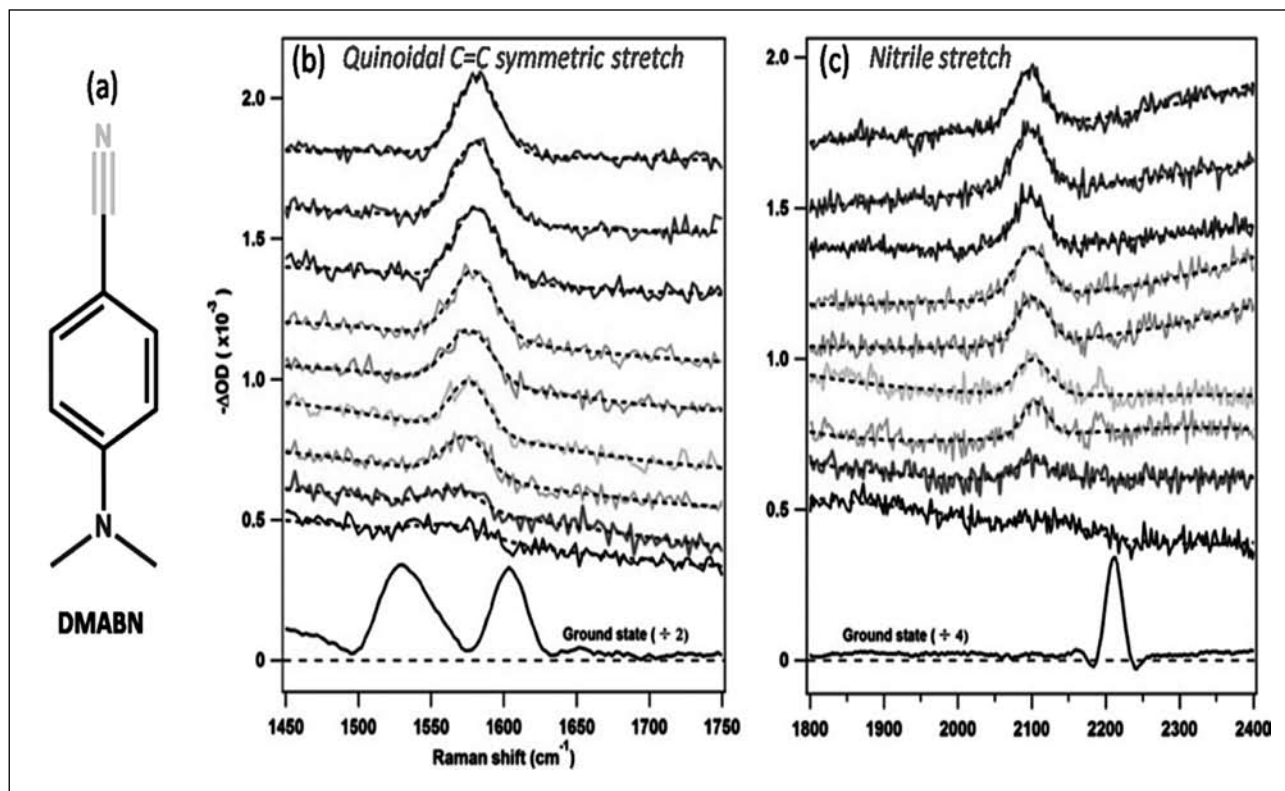


Figure 4. (a) Molecular structure of DMABN with donor amine group and acceptor nitrile group coupled through bond; (b) & (c) FSRS spectra of DMABN in methanol with 330 nm Raman pulse. (b) quinoidal C=C symmetric stretching mode; and (c) nitrile stretching mode. Adapted from reference 32. (Permission required)

UV light photoinduced CT is observed in the excited state. The uniqueness of this system lies in complexity of electronic states manifold, dual fluorescence from locally excited (LE) to CT states and importance of intra-molecular and solvent reorganization.<sup>37-39</sup> After optical excitation to  $S_2$  state,  $L_a$  ( $\pi\pi^*$ ) picosecond relaxation lead it to the LE state which further relaxes to the twisted intramolecular charge transfer (TICT) over next 5-10 ps.<sup>36</sup> TICT state is characterized by quinoidal contraction of the benzene ring and  $90^\circ$  twist of the amine. This system has been probed by various steady state and time-resolved electronic and vibrational techniques that established the twisted quinoidal structure of CT state.<sup>40</sup> But still complete understanding of molecular and solvent modes driving these CT transitions has been questioned for long.

David McCamant and co-workers probed CT dynamics of DMABN in methanol with electronic pump-probe and FSRS using two

different wavelengths for Raman pump, 330 and 400 nm.<sup>41-42</sup> Electronic pump-probe measurements in 280-600 nm window showed three processes leading to the relaxed CT state: (1)  $S_2$  to LE ( $\sim 0.3$  ps); (2) LE to hot CT states ( $\sim 2$  ps); (3) intramolecular vibrational relaxation of hot CT states ( $\sim 6$  ps). In time-resolved FSRS with 400 nm Raman pump, spectral shift for  $1582\text{ cm}^{-1}$  quinoidal C=C stretching vibration was observed for the CT which was attributed to off diagonal coupling to other receiving modes.

Resonance Raman excitation at 330 nm of the excited state absorption band whose transition dipole is parallel to the long molecular axis, vibrational dynamics of three more modes has been captured: (1)  $764\text{ cm}^{-1}$  ring breathing; (2)  $1174\text{ cm}^{-1}$  CH in plane bend; (3)  $2096\text{ cm}^{-1}$  nitrile stretch. With the addition of anharmonic coupling calculations of a model compound using DFT, spectral shifts of different vibrational modes has been assigned to different processes. This clearly gave an insight into the CT dynamics of DMABN but at the same time demands further experimental and theoretical insight. This clearly enunciates that electron transfer reactions are in most cases coupled to the intramolecular vibrations and thereby leads to structural changes during the process.

### 3. Ultrafast ET on dye-semiconductor interface

One of the marvels of chemical reactions operating in biology is the precise optimization of rates under environmental pressure and associated evolutionary constraints. A significant biochemical ET reaction that has inspired many synthetic organic and inorganic chemists for its operative efficiency and timescale is the charge separation reaction in photosynthetic reaction center.<sup>43,44</sup> Spurred by the concept of capturing visible photons for fuel generation in photosynthesis, Michael Graetzel and co-workers designed the dye-sensitized solar cell (DSSC) which comprises of a dye chemisorbed onto Pt electrode coated with nanoporous

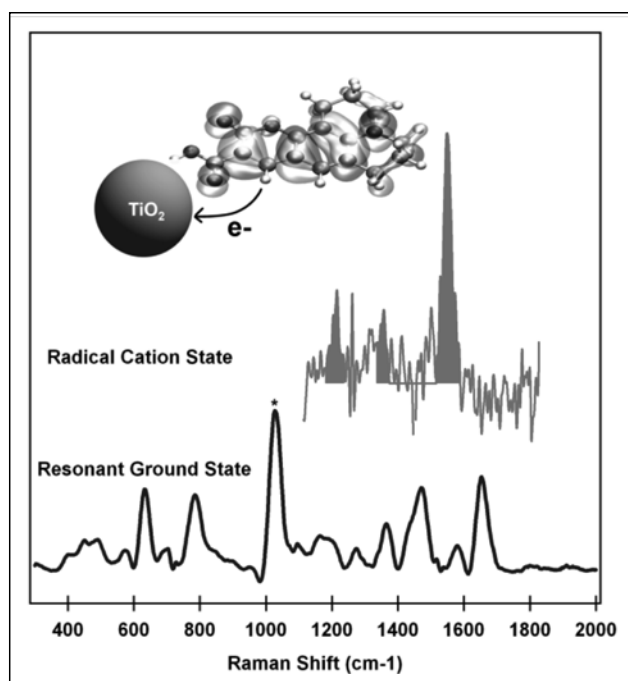


Figure 5: Interfacial ET in C343-TiO<sub>2</sub>: Resonant stimulated Raman spectrum of TiO<sub>2</sub> bound C343 molecules shown in blue indicates the enhanced modes at 632 and 785  $\text{cm}^{-1}$  indicative of large excited state displacements. The FSRS spectrum of the radical cation shows primarily the delocalized C=C stretches and ring bends.

TiO<sub>2</sub>.<sup>45</sup> The major breakthrough in this variant of solar cell was the use of small molecule visible absorbers which could form coordinate-covalent bond with the titania surface and thereby force ultrafast electron injection into the TiO<sub>2</sub> conduction band. However, the productive implementation of such devices have been hindered by the disparity in the injection timescales (10 fs to 100 ps) for various dye structures. This lack of insight in an apparently “simple” chemical reaction where the donor and acceptor are in strong coupling limit emanates from a poor understanding of the molecular mechanism of the process.

To address this critical question in such ultrafast interfacial ET (IET) reactions, Mathies and co-workers employed FSRS to investigate the injection dynamics of photoexcited Coumarin 343 (C343) to anatase titania nanoparticles.<sup>46</sup> Since free C343 is fluorescent, FSRS presents a unique opportunity to look at both the ground state and the time-evolving vibrational structure of the excited molecule. Steady state resonance stimulated Raman spectrum of C343-TiO<sub>2</sub> with Raman excitation at 500 nm showed considerable Raman intensities in the low frequency ring breathing modes at 632 and 785 cm<sup>-1</sup>. In fact, most of the intense modes involve a stretching character in the carbon pi-backbone, and no predominately nitrogen stretching modes are active.

In order to get information on the dynamics of ET and the structure of radical cation, time-resolved vibrational spectra were recorded with a 500 nm phototrigger and Raman excitation at 800 nm, one of which has been depicted in Figure 5. Previous transient absorption work on colloidal C343-TiO<sub>2</sub> identified a 100–200 fs component due to the charge injection process and a 190 ps charge recombination time. The FSRS evolution showed similar time constants along with a new 3 ps time constant assigned to an electron exchange reaction between a neutral free C343 and the incipient hole on the surface bound C343. The rise of the radical cation state occurred at ~125

fs timescale but the poor signal-to-noise ratio in the radical cation spectrum resulted from a lack of resonance enhancement but still showed three peaks at 1549, 1358, and 1205 cm<sup>-1</sup> corresponding to the C–N/C=C stretch, C–H in-plane bend, and CH<sub>2</sub> rock/C–C stretch, respectively. Comparing the frequency of these peaks to calculated DFT frequencies, it was concluded that the hole resides on the carbon backbone rather than on the N-center of C343.

Since the forward ET occurs on a rapid timescale (~100 fs), it is likely that the initial dynamics that lead the system toward the charge-separated state (D<sup>+</sup>A<sup>-</sup>) should happen on part of the surface with high gradient. It is known from Heller’s time-dependent formalism that the vibrational modes with large excited state displacements along the normal coordinate have high resonance Raman scattering cross sections. For these highly displaced modes, the gradient encountered on the excited state potential after absorption leads the system out of the Franck-Condon (FC) region.<sup>47</sup> Thus the ring breathing modes in conjunction with high-frequency carbon-stretching modes (delocalized ring C=C stretch) must be the suspects to drive the system into the CT state. Additionally, the enhanced vibrational modes observed in the resonance Raman spectra do not include significant motion of the nitrogen atom, the donated electron perhaps comes from the pi-bonding backbone rather than the nitrogen center. Evidently the coordinated motion from many carbon atoms is required for this ultrafast electron transfer to happen efficiently. Therefore, resonance Raman spectroscopy shows that it is imperative to consider multiple modes rather than just one to two modes for explaining and predicting the reaction.<sup>48</sup> Thus, unraveling the key nuclear motions which promote the forward ET and retard the recombination can lead to insights on the design of efficient and potentially cheap solar cells.

### Future Prospects

The examples described above clearly emphasizes emphatically that vibrational

structure can hold important clues to the reaction coordinate which electronic spectroscopy can easily overlook. In fact, FSRS has the potential to unravel novel insight into the classic reaction dynamics problem of energy exchange between reactive modes participating in a chemical reaction. Extending the FSRS technique to unravel inter-mode couplings in a wide range of molecules and with higher time resolution would significantly advance our understanding of molecular reaction dynamics. To easily accomplish the detection of anharmonic couplings, ultrashort femtosecond pulses (5 fs) will enable the creation of vibrational wavepackets in a large number of modes either in the ground state or excited state, and coherently pump vibrations up to 2,000  $\text{cm}^{-1}$ .<sup>49,50</sup> The anharmonic coupling between individual low-frequency and high-frequency modes will thus create a complex time-evolving oscillatory pattern in the frequency domain FSRS spectra which would give information on the shape of the potential energy landscape that determine chemical reactivity.<sup>51</sup> Therefore, a direct high precision temporal mapping of the multidimensional potential energy surface along the reaction coordinate should be possible using few cycle pulses. In future, FSRS is poised to tackle more intriguing photoactive biological systems to reveal the structurally encoded anharmonicities of vibrational modes that defines the multidimensional potential energy landscape leading to its functions.

### Acknowledgements

The authors want to acknowledge the organizers of spectroscopy and dynamics mini-symposium for giving the opportunity to present their work in the meeting. This chapter has been written as an expansion of the ideas developed from the talk given by Dr. Jyotishman Dasgupta in the symposium. Mr. Ajay Jha acknowledges the DAE for supporting his graduate assistantship in TIFR, Mumbai.

### References

1. Artem A. Bakulin et al. *Science* 2012, 335, 1340.
2. Fleming GR; Martin JL; Breton J. *Nature* 1988, 333, 190-92.
3. Shank CV. *Science* 1986, 233, 1276-80.
4. Rudi Berera et al. *Photosynth Res* 2009, 101, 105-118.
5. Underwood DF. et al. *J. Phys. Chem. B*, 2001, 105(2), 436-443.
6. Hamaguchi H; Gustafson TL. *Annu. Rev. Phys. Chem.* 1994, 45, 593-622.
7. Dhar L; Rogers JA; Nelson KA. *Chem. Rev.* 1994, 94,157-93.
8. Fayer MD, ed. 2001. *Ultrafast Infrared and Raman Spectroscopy*. New York: Marcel Dekker.
9. Nibbering ETJ; Fidler H; Pines E. *Annu. Rev. Phys. Chem.* 2005, 56, 337-67.
10. Fayer MD. *Annu. Rev. Phys. Chem.* 2009, 60, 21
11. D. W. McCamant; P. Kukura; S. Yoon and R. A. Mathies, *Rev. Sci. Instrum.*, 2004, 75, 4971-4980.
12. J. V. Lockard; A. B. Ricks; D. T. Co and M. R. Wasielewski, *J. Phys. Chem. Lett.*, 2010, 1, 215-218.
13. M. Yoshizawa; H. Aoki and H. Hashimoto, *Bull. Chem. Soc. Jpn.*, 2002, 75, 949-955.
14. D.W. McCamant; P. Kukura and R. A. Mathies, *J. Phys. Chem. A*, 2003, 107, 8208-8214.
15. P. Kukura; D. W. McCamant and R. A. Mathies, *Annu. Rev. Phys. Chem.*, 2007, 58, 461-488.
16. P. Kukura; D. W. McCamant; S. Yoon; D. B. Wandschneider and R. A. Mathies, *Science*, 2005, 310, 1006-1009.
17. D. W. McCamant; P. Kukura and R. A. Mathies, *J. Phys. Chem. B*, 2005, 109, 10449-10457.
18. S. Shim; J. Dasgupta and R. A. Mathies, *J. Am. Chem. Soc.*, 2009, 131, 7592-7597.
19. J. Dasgupta; R. R. Frontiera; K. C. Taylor; J. C. Lagarias and R. A. Mathies, *Proc. Natl. Acad. Sci. U. S. A.*, 2009, 106, 1784-1789.
20. C. Fang; R. R. Frontiera; R. Tran and R. A. Mathies, *Nature*, 2009, 462, 200-204.
21. Cerullo G; De Silvestri S. *Rev Sci Instrum.* 2003, 74, 1-18.
22. Shim S; Mathies RA *Appl. Phys. Lett.* 2006, 89, 121124.
23. R. R. Frontiera; C. Fang; J. Dasgupta and R. A. Mathies *Phys. Chem. Chem. Phys.*, 2012, 14, 405-414.
24. J. Dasgupta; R. R. Frontiera; C. Fang and R. A. Mathies, *Encyclopaedia of Biophysics*, 2012.
25. Zhao B, et al. *Sci China Chem*, 2011, 54, 1989-2008.
26. Keitaro Yoshihara, *Advances in Chemical Physics*, Vol. 107, 371-402.
27. Asahi, T.; Ohkohchi, M.; Mataga, N. *J. Phys. Chem.* 1993, 97, 13132-13137.
28. Asahi, T.; Mataga, N. *J. Phys. Chem.* 1991, 95, 1956-1963.
29. Asahi, T.; Mataga, N. *J. Phys. Chem.* 1989, 93, 6575-6578.
30. Englman, R.; Jortner, J. *Mol. Phys.* 1970, 18, 145-164.
31. Freed, K. F.; Jortner, J. *J. Chem. Phys.* 1970, 52, 6272-6291.
32. Fujisawa T. et al. *J. Phys. Chem. B* 2012, 116, 10453-10460.
33. Lippert, E. *Angew. Chem.* 1961, 73, 695-706.
34. Lippert, E.; Rettig, W.; Bonacic-koutecky, V.; Heisel, F.; Mielke, J. A. *Adv. Chem. Phys.* 1987, 68, 1-173.

35. Grabowski, Z. R.; Rotkiewics, K.; Rettig, W. Chem. Rev. 2003, 103, 3899–4031.
36. Rettig, W. Angew. Chem., Int. Ed. 1986, 25, 971–988.
37. Hättig, C.; Hellweg, A.; Köhn, A. J. Am. Chem. Soc. 2006, 128, 15672–15682.
38. Yoshihara, T.; Galievsky, V. A.; Druzhinin, S. I.; Saha, S.; Zachariasse, K. A. Photochem. Photobiol. Sci. 2003, 2, 342–353.
39. Dahl, K.; Biswas, R.; Ito, N.; Maroncelli, M. J. Phys. Chem. B 2005, 109, 1563–1585.
40. Okamoto, H.; Inishi, H.; Nakamura, Y.; Kohtani, S.; Nakagaki, R. J. Phys. Chem. A 2001, 105, 4182–4188.
41. Rhinehart, J. M.; Mehlenbacher, R. D.; McCamant, D., J. Phys. Chem. B 2010, 114, 14646–14656.
42. Rhinehart, J. M.; Challa, J. R.; and McCamant, D., J. Phys. Chem. B 2012, 116, 10522–10534.
43. Gray HB and Winkler JR Quart. Rev. Biophys. 2003, 36, 341–372.
44. Magnuson A, Anderlund M, et al. Acc. Chem. Res. 2009, 42, 1899–1909.
45. O'Regan B and Gratzel M, Nature 1991, 353: 737–740.
46. Frontiera R.R., Dasgupta J. and Mathies, R.A., J. Am. Chem. Soc. 2009, 131, 15630–15632.
47. Lee S.Y. and Heller E.J., J. Chem. Phys., 1979, 71: 4777–4788.
48. Jortner J., J. Chem. Phys., 1976, 64, 4860–4864.
49. Polli D., Luer L, et al. Rev. Sci. Instrum., 2007, 78, 103108.
50. Fayer M.D., Annu. Rev. Phys. Chem., 2009, 60, 21.
51. Zhu L.Y., Sage J.T., et al. Science 1994, 266, 629.



**Mr. Ajay Jha** received his undergraduate degree in chemistry from Sri Venkateswara College, University of Delhi in 2007. After receiving his masters in organic chemistry from Department of Chemistry, University of Delhi in 2009, he joined Tata Institute of Fundamental Research, Mumbai for Ph.D. under the supervision of Dr. Jyotishman Dasgupta. His interest lies in developing mechanistic understanding of ultrafast electron transfer reactions (ET) in different systems including ET in homogenous solutions, at heterogeneous interfaces and in photosystem II, and capitalizing these understanding to develop molecules for efficient charge separation in molecular devices like dye sensitized solar cell.



**Dr. Jyotishman Dasgupta** received his undergraduate degree in chemistry from Indian Institute of Technology, Kharagpur in 2000. He subsequently carried out his Ph.D. work in the field of photosynthesis at Princeton University, where he looked at the photoassembly of the water-oxidizing  $Mn_4Ca$  cluster in photosystem II under the supervision of Prof. Charles Dismukes. In 2006, he moved to UC Berkeley where he did his postdoctoral work with Prof. Richard A. Mathies. Since 2010, he is an Assistant Professor at the Tata Institute of Fundamental Research, Mumbai. The central theme of his Ultrafast Biophysics and Photomaterials lab is to probe biological electron, proton and atom transfer in order to fabricate bio-inspired molecule-based devices for fuel and electricity generation.

# Molecular Mechanism of DNA-Drug Intercalation: Structural and Dynamical Events, Role of Water and Entropy

Wilbee D. Sasikala and Arnab Mukherjee\*

Department of Chemistry, Indian Institute of Science Education and Research, Pune, India

Phone: +91 (20) 2590 8051, Fax: (+91 (20) 2589 9790)

E-mail: [arnab.mukherjee@iiserpune.ac.in](mailto:arnab.mukherjee@iiserpune.ac.in), [dr.arnab.mukherjee@gmail.com](mailto:dr.arnab.mukherjee@gmail.com)

## Introduction

DNA intercalators, included in the class of chemotherapeutic agents because of its anti-cancer property<sup>1-2</sup>, defined as planar aromatic molecules which inserts between the DNA base pair and get stabilized by stacking interaction with adjacent base pairs<sup>3-4</sup> leading to inhibition of replication and transcription processes thereby causing cell death. They act by interfering the binding of DNA with enzymes such as topoisomerases I/II, helicases and nucleases as well as they often cause mutation and DNA strand breakage<sup>5-10</sup>. As DNA intercalating agents are able to arrest cell division and growth, they are clinically used in the treatment of various kinds of cancers in combination with other chemotherapeutic agents.

The biological activity of anticancer compounds are studied and proved by different experimental studies.<sup>11-23</sup> Thermodynamic and kinetic studies<sup>15-17</sup> were performed using fluorescent spectroscopic methods, while structural investigations were carried out using NMR<sup>18</sup>, crystallography<sup>24</sup>, molecular modelling<sup>20-22</sup>, force spectroscopic methods<sup>23</sup> etc. The crystallographic studies have shown that intercalation leads to lengthening of DNA due to increase in the inter-base pair distance (Rise) (3.4 to 6.8 Å)<sup>24</sup> where the intercalation has happened. The crystal structure shows the final intercalated structure. However, it does not give details of the sequence of events (changes in the DNA parameters as well as conformational changes of the drug) taking place during the intercalation process.

The kinetic studies on different intercalators such as daunomycin and proflavine also remained elusive. Kinetic studies of daunomycin by Chaires et al.<sup>25</sup> suggested a three-step model for intercalation, while Rizzo et al.<sup>26</sup> suggested a five-step process. But the kinetic studies on the intercalation of proflavine to DNA proposed a two step mechanism<sup>15</sup>. In general, the intercalator forms a faster outside bound state first and then slowly inserts between the base pairs to form the intercalated state. For daunomycin, a third step was suggested in which the "reshuffling" of the drug happens in the intercalated state<sup>25</sup>. Two limiting hypothesis<sup>15</sup> emerged from all these studies regarding the mechanism of intercalation: one in which DNA base pairs open up momentarily close to the bound drug due to thermal fluctuations allowing it to enter and the other in which the drug slowly induces the cavity in the DNA without prior base pair opening. Capturing of these dynamical aspects of intercalation was not possible with different spectroscopic methods.

Water also plays an important role in all biological processes such as protein folding, protein-ligand interaction, transport of small molecules etc<sup>27</sup>. The role of water in the intercalated process was also studied experimentally by Chaires<sup>28-29</sup> in the intercalated geometry. However, the changes in number of water molecules as well as the entropy of water and other components during the intercalation process were not addressed.

The theoretical studies on DNA-drug intercalation mainly focused on the overall free energy change of intercalation process<sup>30-31</sup> in

solvent/environment approaches. However, various molecular aspects of intercalation including thermodynamic and kinetic pathway, associated with structural changes to the DNA and role of water and entropy during the intercalation process were not studied even though intercalation process provides a potential drug design strategy towards new anticancer drug design. To address the above problems, we used extensive all atom molecular dynamic simulations with accelerated sampling processes such as metadynamics<sup>32</sup>, well tempered metadynamics<sup>33</sup> and umbrella sampling<sup>34</sup> using proper collective variables (reaction co-ordinates) which could be assumed as the basic reaction pathway.

To understand the mechanism of intercalation, we performed de-intercalation of daunomycin from the intercalated state (crystal structure geometry)<sup>35</sup> by metadynamics and umbrella sampling simulations. The simulations provide a free energy barrier for intercalation process which is in agreement with the experimental results. Pathway of intercalation was found to be from the minor groove bound state to the intercalated state crossing the free energy barrier between the stable minor groove bound state and intercalated state. This study gives detailed information about the structural changes happening during the intercalation process but did not give any insight into the third step where the conformational change of daunomycin occurs. Further investigation on daunomycin intercalation revealed a passage of daunomycin from the minor groove to the intercalation site involving a metastable intermediate and two transition states. In the metastable intermediate state, daunomycin stays in partially intercalated state bending the DNA towards the major groove.

Both the above studies mainly focused on the de-intercalation of daunomycin since direct intercalation from any groove bound state is practically difficult using normal MD simulations as intercalation happens in millisecond time scale.

Further, to probe into the details of sequence of events during the intercalation process as well as to understand whether the drug induces a cavity in the DNA during the intercalation, we have done intercalation of proflavine from minor groove of DNA using well-tempered metadynamics simulations. The results showed that intercalation precedes by drug induced cavity formation and during the intercalation non-stacking parameters of DNA change first followed by the changes in the stacking parameters.

A general enthalpy/entropy balance<sup>36-37</sup> is shown by the thermodynamic analysis of the intercalation<sup>38-40</sup> and other drug-DNA binding processes<sup>41-42</sup>. Based on the experimental evidences Chaires pointed out a thermodynamic feature of drug-DNA binding that intercalation is primarily enthalpy driven and binding to the minor groove is entropy driven<sup>43</sup> and for daunomycin overall entropy change is only -1.1 kcal/mol.<sup>43-44</sup> To capture entropy contributions of the individual components of intercalation process, we used molecular dynamics simulations to calculate configurational entropy of the drug, DNA and water to understand the overall small entropy contribution<sup>45</sup> coming from various components mentioned above.

## Methods

**Umbrella Sampling:** Umbrella sampling<sup>34</sup> is one of the accelerated sampling methods in molecular dynamics simulations where an additional biased potential is applied to study the free energy change along a reaction coordinate or collective variable in complex biological processes where the events happens in millisecond time interval or even higher. Umbrella sampling along a (one or multi-dimensional) reaction coordinate takes a system from one thermodynamic state to another (e.g. reactant and product) giving the pathway of reaction. The intermediate steps between the reactants and products are covered by a series of small windows (defined by the collective variable or reaction coordinate), at each of which

umbrella sampling simulation is performed. From the sampled distribution of the system in each window along the reaction coordinate, the change in free energy in each window can be calculated and combined by weighted histogram analysis method (WHAM).<sup>46-47</sup>

In umbrella sampling, the bias potential is applied in the following form,

$$V_{umb}(s) = \frac{1}{2}k(s - s_0)^2 \quad (1)$$

where,  $k$  is the force constant,  $s$  is the collective variable value at which the restraint is applied,  $s_0$  is the collective variable space.

The unbiased free energy ( $\tilde{F}(s)$ ) obtained by the following equation<sup>48</sup>,

$$\tilde{F}(s) = -\frac{1}{\beta} \ln N(s) - V_{umb}(s) \quad (2)$$

where,  $N(s)$  is the histogram of the visited configurations in the collective variable space,  $V_{umb}(s)$  is the applied bias potential,  $\beta = \frac{1}{k_B T}$  where  $k_B$  is the Boltzmann constant and  $T$  is the temperature.

**Metadynamics:** Metadynamics<sup>32</sup> is an accelerated sampling method for rapid computation of multidimensional free-energy surfaces of complex biological processes which happens in millisecond time scale, where normal molecular dynamic simulations often fail because of complex free energy surface. The metadynamics algorithm assumes that the system can be described by the reaction coordinate (called as collective variables, CV) along which the reaction happens. During the simulation, the position of the system in the configurational space, determined by the collective variables, is calculated and a Gaussian potential is added to the energy landscape of the system to avoid revisiting the already sampled region in the free energy surface.

The metadynamics potential<sup>32</sup> ( $V_G(s, t)$  at a particular time,  $t$  is equal to,

$$\omega \sum_{t'=\tau_G, 2\tau_G, 3\tau_G, \dots} \exp\left(-\frac{(s(x) - s(x_G(t')))^2}{2\delta s^2}\right) \quad (3)$$

where,  $\omega$  = height of the Gaussian,  $\delta s$  = width of the Gaussian,  $\tau_G$  = frequency at which the Gaussian is added,

$s(x)$  = Conformational space described by the collective variable (CV),  $s(x_G(t))$  value taken by the collective variable at time  $t'$ ,  $t$  = sampling time.

Free energy surface  $F(s)$  in the conformational space  $s(x)$  is the opposite of the sum of all Gaussian potential.<sup>32</sup> So,

$$F(s) \sim -\lim_{t \rightarrow \infty} V_G(s(x), t) \quad (4)$$

Finally, one gets the free energy profile as a function of the collective variables. The accuracy and speed of sampling can be altered by changing two parameters such as Gaussian height and Gaussian width mentioned above as well as the time interval between additions of two Gaussian functions.

**Well tempered metadynamics:** In normal metadynamics simulation, the free energy does not converge to a definite value leading to an average error. Continuing a simulation irreversibly pushes the system to regions of configurational space which are not physically relevant. To solve this problem well tempered metadynamics<sup>33</sup> is developed which has the advantage of controlling the regions of the free energy surface which are physically relevant.

In case of well-tempered metadynamics, the Gaussian height is rescaled during the simulation according to the following equation<sup>20</sup>,

$$\omega = \omega_0 \exp\left(-\frac{V_G(s(x), t)}{k_B \Delta T}\right) \quad (5)$$

$\omega_0$  = initial Gaussian height,  $k_B$  = Boltzmann's constant,  $\Delta T$  = a parameter with dimension of temperature.

Free energy surface is estimated as<sup>32-33</sup>,

$$\tilde{F}(s, t) = -\frac{T + \Delta T}{\Delta T} V_G(s(x), t) \quad (6)$$

$T + \Delta T$  is called CV temperature, simulation temperature,  $\frac{T + \Delta T}{T}$  is called bias factor.

## Methodology

### Description of the Collective Variables:

Figure 1a shows the schematic representation of DNA and drugs with the collective variables description.  $\hat{c}$  is the vector from the center of mass (COM) of intercalating base pair (C6, G7, C19 and G18) to COM of drug.  $\hat{d}$  is the unit vector

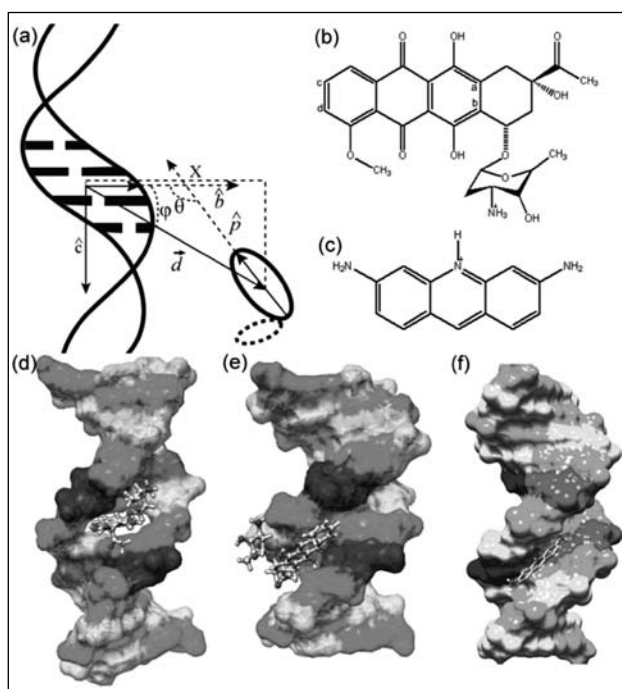


**Figure 1** Schematic representation of collective variables and initial configurations. (a) Schematic of DNA and the drugs (daunomycin-with solid oval shaped aglycon ring and dashed oval shaped sugar moiety; proflavine represented by the solid oval shape only). It also shows the construction of collective variables and  $Y$ . (b) and (c) are structures of daunomycin and proflavine respectively. (d), (e) and (f) shows the intercalated geometry of daunomycin in DNA, minor groove bound state of daunomycin and proflavine in DNA respectively.

from the COM of intercalating base pairs to COM of two sugars which lie more towards the minor groove of intercalating base pairs.  $\hat{p}$  is the unit vector from the COM of two atoms (a, b as shown in figure 1 b) of daunomycin to COM of other two atoms (c, d as shown in figure 1 b) of daunomycin.  $\hat{c}$  is body-fixed vector from the COM of intercalating base pairs to the COM of the 3'-terminal base pairs (C12 and G13).  $X = \hat{b} \cdot \hat{d}$ ,  $\varphi = \cos^{-1} \hat{b} \cdot \hat{d}$ ,  $\theta$  corresponds to the angle between the unit vectors  $\hat{b}$  and  $\hat{p}$ .  $Y$  is the

scalar product of  $\hat{c}$  and  $\hat{d}$ . The collective variable  $X$  defines the position of the drug in the minor or major groove side of DNA. +ve  $X$  indicates that drug is in the minor groove side of the DNA and -ve  $X$  shows that the drug is in the major groove side of the DNA.  $\varphi$  represents the position of the drug along the helical axis of DNA.  $\varphi$  value between  $0^\circ$  to  $90^\circ$  denotes that drug moves along the DNA in the minor groove and between  $90^\circ$  to  $180^\circ$  denotes that drug moves along the DNA in the major groove.  $\theta$  measures the angle between the vector which corresponds to the long axis of daunomycin molecule and the unit vector. In the intercalated state  $\theta$  is  $90^\circ$ . The collective variable  $Y$  describes the movement in the direction of the helical axis.

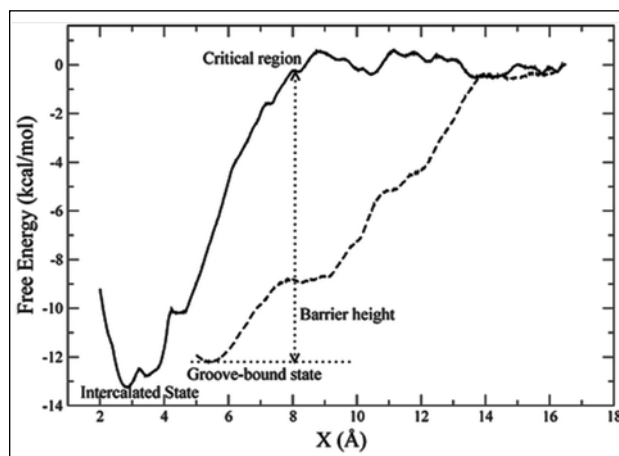
**Simulation Protocol:** For intercalated state of daunomycin<sup>35</sup> we have taken the crystal structure geometry in 12 base pair BDNA. To obtain minor groove bound state we performed docking of proflavine and daunomycin to BDNA using docking software AutoDock<sup>50</sup> and HEX<sup>51</sup> respectively. The force field parameters for DNA are generated using AMBER99/parmbsc0<sup>52-53</sup> force field. For proflavine and daunomycin the force field parameters are generated using general amber force field (GAFF)<sup>54</sup> after optimization and partial charge calculation in Gaussian<sup>55</sup> using the basis set HF/6-31G\*. The generated topology and co-ordinate files from XLEAP module of AMBER<sup>56</sup> was converted to GROMACS<sup>57</sup> format using amb2gmx.pl program<sup>58</sup>/. Rest of the simulation protocol is same for all the simulations for de-intercalation, intercalation and entropy calculations. The drug-DNA complex was put in a large cubic box ( $\sim 70$  Å in each direction) and solvated with TIP3P water model<sup>59</sup>. Sodium and chloride ions were added to neutralize the negative charge on the DNA and positive charge on the drug. The whole system was then energy minimized and heated to 300 K with position restraint on the heavy atoms of DNA and drug. After energy minimization a series of consecutive equilibration and energy minimization is done with position restraint

(25 kcal/mol/Å<sup>2</sup> to 0.5 kcal/mol/Å<sup>2</sup>). Finally an unrestrained equilibration is done for 1ns at constant temperature (300 K) and pressure (1 bar) using Berendsen thermostat and Nose-Hoover barostat respectively<sup>60-62</sup>. The final equilibrated system was then taken for further metadynamics and umbrella sampling for de-intercalation of daunomycin, well-tempered metadynamics for intercalation of proflavine from minor groove side of DNA. For entropy calculations for daunomycin intercalation normal molecular dynamics simulation was used. For molecular dynamics simulations we have used GROMACS software<sup>57</sup> patched with metadynamics software PLUMED<sup>48</sup> with appropriate modification in the code to incorporate our new collective variables. For metadynamics and well-tempered metadynamics simulations the value of Gaussian height and width were calculated based on fluctuations of the collective variables during the initial equilibration. For well tempered metadynamics simulations, we used bias factor 15 for intercalation and dissociation from minor groove bound state.

## Results and Discussions

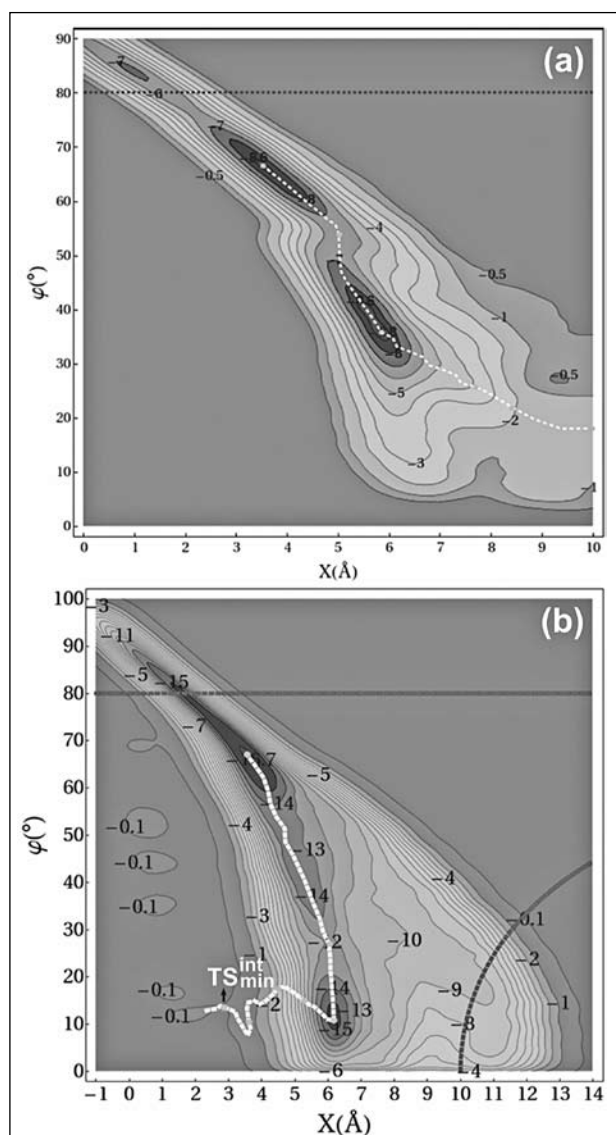
**Two-step Intercalation Process through Minor Groove-Bound State:** To find out the mechanism of intercalation we performed de-intercalation from intercalated (initial configuration of intercalated state shown in figure 1d) to free state by umbrella sampling simulations along the chosen collective variable  $X$ . We did 35 simulations to achieve DNA-drug separation. To get a complete picture of intercalation process, umbrella sampling simulations were done starting from minor groove bound state (initial configuration of the minor groove bound state shown in figure 1e) to complete separation of the drug from DNA. After the umbrella sampling simulations the potential of mean force (PMF) is generated using weighted histogram analysis method (WHAM) along the chosen reaction coordinate  $X$ .

Figure 2 shows the PMF of intercalation and minor groove bound state formation of



**Figure 2** Potential of mean force (PMF) of umbrella sampling simulations along the reaction coordinate  $X$ <sup>49</sup>. The completely dissociated state ( $X \sim 16$  Å) is considered to be the reference free energy value. The solid line represents the PMF for intercalation from completely dissociated state and the dotted line represents the PMF of minor groove bound state formation from completely dissociated state. The decrease in the value of  $X$  from 16 Å to 2 Å represents that drug moves closer to the DNA.

daunomycin to DNA. The free energy difference between the intercalated and minor groove bound state is  $\sim -13.2$  kcal/mol. After further corrections on this free energy value it is compared with the experimental value and corrected value found to be  $-12.3$  kcal/mol which is in agreement with the experimental value  $\sim -9.4$  kcal/mol<sup>63</sup>. The detailed analysis of the PMFs showed that the drug first reaches minor groove by downhill process and for the intercalation the drug has to orient to insert the aglycon portion of the daunomycin inside the base pairs. This happens at a critical distance of  $X \sim 8$  Å. So the free energy barrier for intercalation from the critical region is obtained by taking a difference between the free energy value at the critical region ( $X \sim 8$  Å which corresponds to  $-0.3$  kcal/mol) and free energy of minor groove bound state ( $-12.2$  kcal/mol) giving rise to a barrier of  $11.9$  kcal/mol which is in reasonable agreement with experimental value  $14.9$  kcal/mol<sup>64</sup>. So here, drug follows a minimum free energy pathway along the minor groove bound state and then crosses the barrier by changing the orientation and the distance to get intercalated.<sup>49</sup>



**Figure 3** Free energy surface (FES) of intercalation and dissociation processes. (a) Shows the FES for dissociation and (b) shows the FES for intercalation process which also shows the transition state for intercalation. The free energy values are written on the contour lines in kcal/mol. The white lines show the minimum free energy path (MFEP) for intercalation and dissociation processes. The blue dotted line represents the configurational restraint on the collective variable  $X$  and  $\phi$ .

To understand intercalation mechanism in detail and to prove the above observations we did intercalation of another anticancer agent proflavine from outside of the DNA since the previous study focused on to the intercalation mechanism by de-intercalating daunomycin from the intercalated state. As intercalation happens in

millisecond time scale, performing intercalation from outside bound state is computationally very difficult to achieve. So to get the intercalated state, well-tempered metadynamics simulations were chosen to avoid sampling of the nonphysical region in the free energy surface by the use of appropriate configurational restraint on the collective variables  $X$  (to prevent the drug going out of minor groove) and  $\phi$  (to prevent the drug to go to the end of DNA). To obtain the free energy stability of the minor groove bound state, well tempered metadynamics simulations were again done to dissociate proflavine to a completely separated state using two collective variables  $X$  and  $\phi$ . The initial configuration of the minor groove bound state for both intercalation and dissociation is shown in figure 1f.

Figure 3 shows the free energy surfaces for dissociation and intercalation of proflavine from minor groove bound state. The free energy of the minor groove bound state is -8.8 kcal/mol which is in agreement with the experimental value -6.8 kcal/mol<sup>65</sup>. This shows that the drug goes to the stable minor groove bound state through a downhill minimum free energy path shown by the white dotted line in the FES shown in figure 3a which corroborates with our previous studies on daunomycin. The FES for intercalation from minor groove side is shown in figure 3b. The free energy barrier for intercalation from minor groove bound state is 16.9 kcal/mol which is in good agreement with the experimental values 12.5 to 15.1 kcal/mol<sup>65-67</sup>. To understand the mechanism of intercalation, we calculated the minimum free energy path (MFEP) using the algorithm of Ensing et al<sup>68</sup>. The MFEP calculation captured the transition state for intercalation as shown in figure 3b. Here also, the drug reaches the minor groove bound state by downhill process and get inserted between the base pairs by crossing the energy barrier for intercalation.<sup>69</sup>

### Emergence of third step of intercalation for daunomycin:

Kinetic studies on daunomycin proposed that intercalation happens by 3 step mechanism

where initial outside bound state formation happens first and finally the “reshuffling” of daunomycin in the intercalated state<sup>64</sup> happens. But previous umbrella sampling studies on the intercalation of daunomycin to DNA were not able to capture the re-orientation of daunomycin in the intercalated state<sup>49</sup>. To capture this event, we performed both metadynamics and umbrella sampling simulations starting from the intercalated state (here also de-intercalation is done). Metadynamics is done to generate the pathway between minor groove bound state and intercalated state using the collective variables  $X$  (describes the distance from the DNA,  $Y$  (movement along the DNA helical axis) and  $\theta$  (orientation of anthraquinone ring of daunomycin). Figure 4a shows the 2D FES for de-intercalation process using three collective variables  $X$ ,  $Y$  and  $\theta$ .

The 2D free energy surface is generated by averaging over the values along the  $Y$  coordinate. Looking at the free energy surface we can see that there exists an intermediate state (IM)

between two transition states (TS2 and TS1). This IM state has achieved after drug moved from the intercalated state by  $\sim 4.5$  Å and rotated about  $\sim 40^\circ$  in  $\theta$  with respect to the intercalated state. Values of DNA parameters for different states are summarized in the Table 1.

**Table 1 Shows DNA parameters of different states during the de-intercalation process.**

Parameters	IC	TS1	IM	TS2	MG1
rise C6pG7 (Å)	7.4	7.3	6.0	5.5	3.8
roll C6pG7 (deg)	-2	28	44	42	8
$\sum$ roll A5-T8 (deg)	-2	40	45	44	7
twist C6pG7 (deg)	38	25	28	29	39
$\sum$ twist A5-T8 (deg)	81	74	84	84	99

The high Roll value ( $44^\circ$ ) of IM state indicates that opening of the base pair happened towards the minor groove side and this causes bending of the DNA towards the major groove. This has happened because of the rotation of the

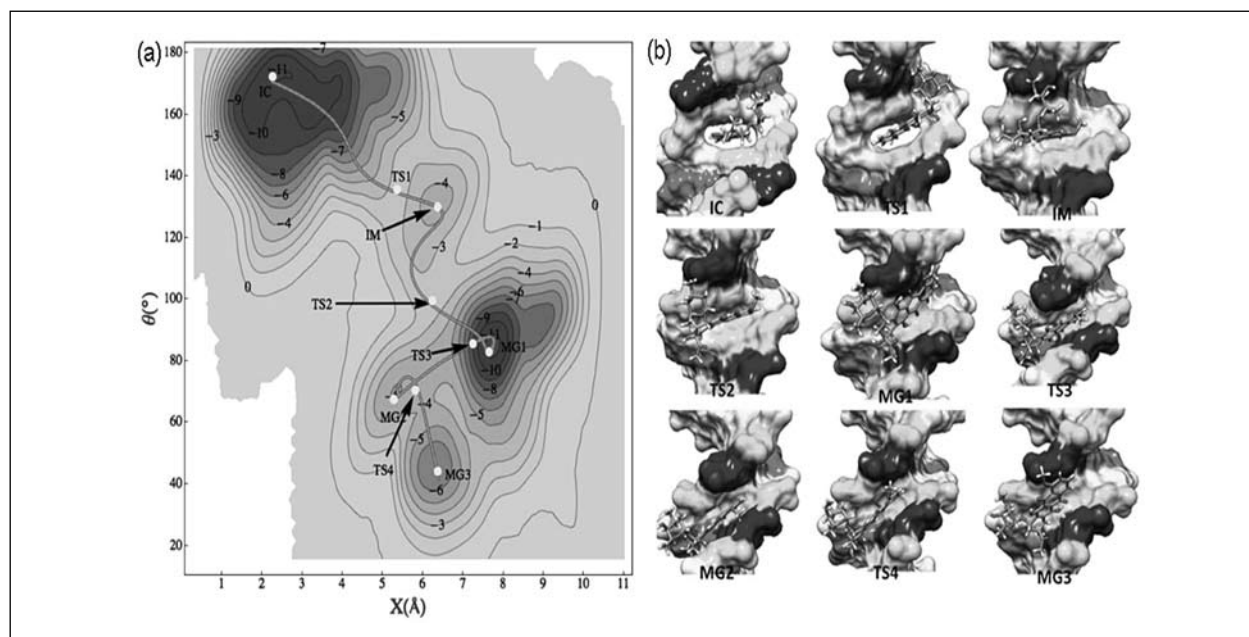


**Figure 4** Shows 2D FES of de-intercalation and configurations corresponding to different states. (a) FES of de-intercalation obtained using the collective variables  $X$ ,  $Y$  and  $\theta$ . The free energy value is represented in kcal/mol on each contour line. The red line shows the MFEP and red spots indicates intercalated state (IC), intermediate states (IM), transition states (TS) and minor groove bound states (MG) along MFEP. (b) Shows configurations corresponding to green spots along MFEP in a sequential manner.

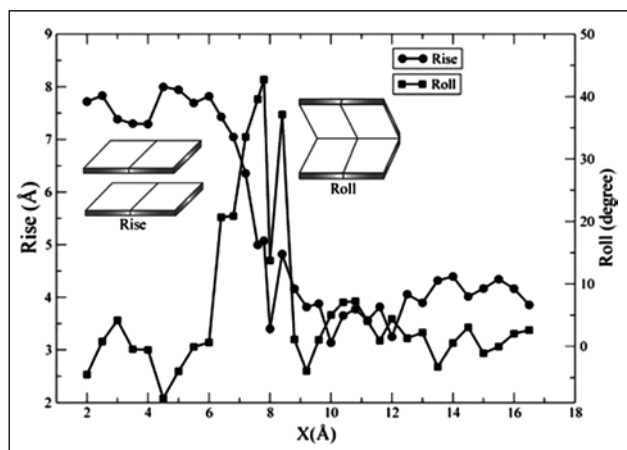


**Figure 5** Shows the changes in the DNA parameters Rise and Roll during the intercalation from outside along the reaction co-ordinate X. The inset figures show the schematic representation of Rise and Roll.

daunomycin (reflected as lower  $\theta$  value) in the partial intercalated state (characterized by a low Rise  $\sim 6$  Å) which is taken as the intermediate state (see figure 4 b). The stability of this intermediate state is  $\sim 4$  kcal/mol proving the concept of reorientation of molecule in the intercalated state as a third step in the intercalation process<sup>70</sup>.

**Analysis of structural changes to the DNA during intercalation process:** The analysis of different DNA base pair step parameters such as Twist, Slide, Shift, Roll, Rise and Buckle shows the structural changes to DNA during intercalation process. Figure 5 shows average value of base pair step parameters Rise and Roll in each umbrella sampling window for the intercalation of daunomycin.

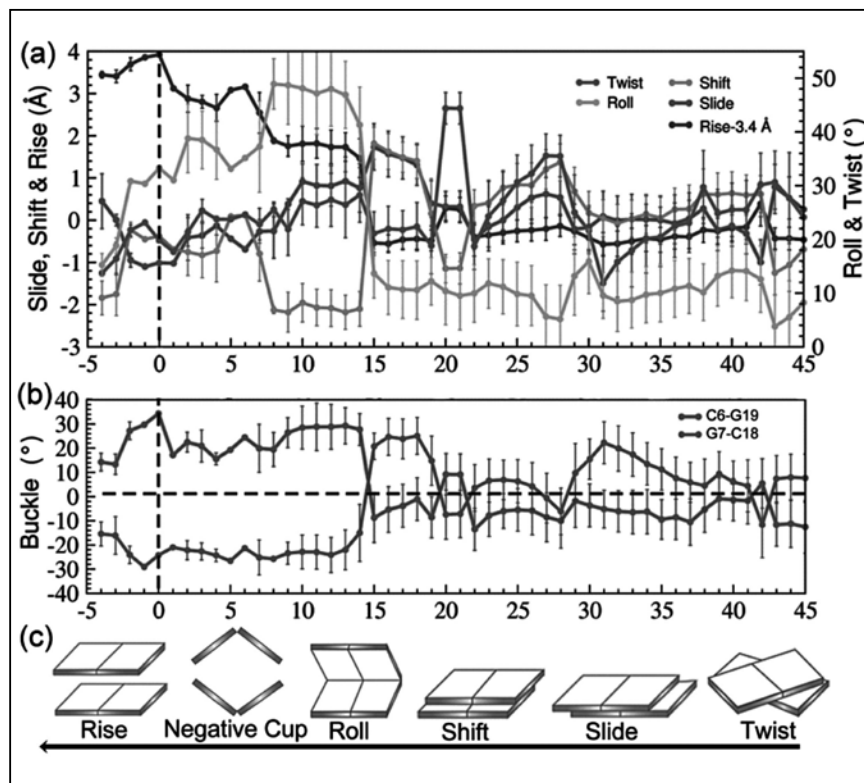


**Figure 6** Analysis of DNA base pair step parameter during intercalation along MFEP. (a) Shows the changes in the base pair step parameters (C6:G19) Slide, Shift, Rise, Roll and Twist along MFEP. (b) Shows the change in the Buckle (C6:G19 in red and G7:C18 in green) during the intercalation process showing positive and negative cup. (c) Shows the schematic of different base pair step parameters in the order of the sequence of changes happening during the intercalation process. The vertical dotted line represents the transition state for intercalation. The standard deviation is also shown.

From outside to the intercalated state along X till  $\sim 8.5$  Å, the fluctuation in Roll and Rise is around their normal values. But for X lower than  $8.5$  Å, the Roll slowly increases indicating the opening of the base pairs towards the minor groove and then finally Rise increases showing the insertion of daunomycin into the base pairs<sup>49</sup>.

The above analysis shows that first Roll increases and then Rise increases during the intercalation process but the study was not able to capture the sequence of changes happening to other base pair step parameters. To understand the sequence of events taking place with respect to the DNA, we have done a detailed analysis on the direct intercalation of proflavine to DNA from minor groove bound state. We performed cluster analysis on the structures centered on

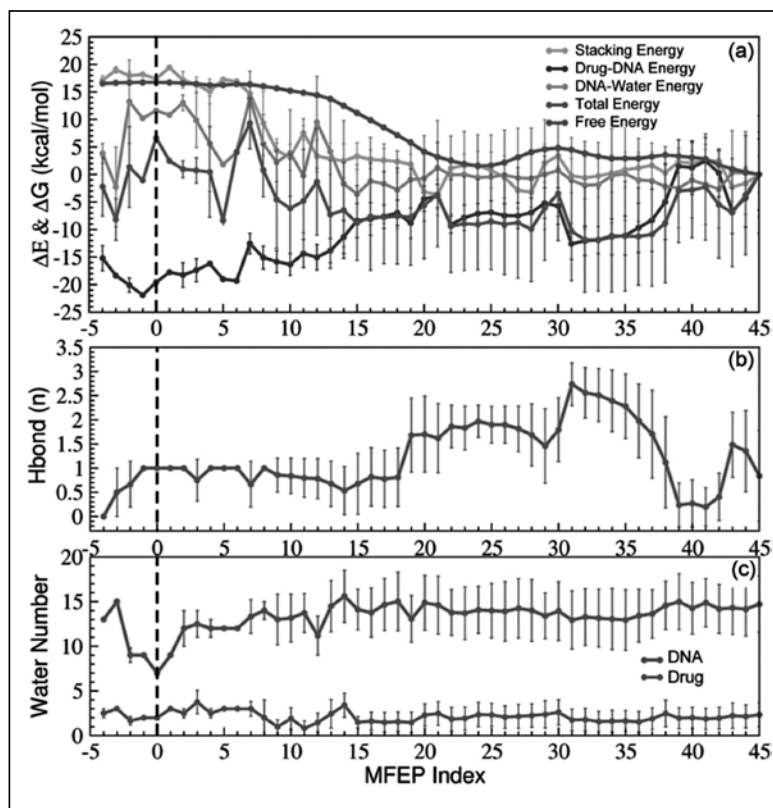


**Figure 7** Analysis of different energy components, hydrogen bonding and water number during the intercalation of proflavine. (a) Comparison of different energy components during the intercalation process along MFEP. Figures (b) and (c) show the hydrogen bonding interaction between bases of DNA and amino groups of proflavine along MFEP and the number of water molecules around DNA and proflavine respectively. The vertical dashed line shows the transition state for intercalation. MFEP index 45 represents the minor groove bound state and MFEP index 0 represents intercalated state. From minor groove bound state to intercalated state the MFEP value decreases.

each of the points in the MFEP and collected the trajectory corresponding to the structures with lowest RMSD value and performed analysis on all DNA parameters using the program CURVES<sup>71</sup>. The figure 6 shows the different DNA base pair step parameters along MFEP for the intercalation of proflavine from minor groove bound state.

The fluctuation of the base pair step parameters reflects a sequential process that follows a minimum the base-stacking penalty pathway. Twist attains lowest value at MFEP index 31 (figure 6a). Change in Twist is followed by increase in Slide and Shift. Largest shift is

followed by a sudden increase of Roll (thus releasing the linear force into an angular motion), where the drug rotates and inserts between the base pairs. In the final phase of intercalation, Roll and Slide decreases followed by buckle changing from positive to negative cup (see figure 6b). The presence of proteins and drugs in the intercalation cavity is known to cause buckling in the DNA<sup>72</sup>. Buckle in negative cup reflects in a sudden increase in Rise.

However, buckle does not cost base-stacking<sup>73</sup> and therefore serves as a remedial measure to avoid energetically costly Rise. Finally, Rise increases showing the insertion of proflavine into the DNA. So the detailed analysis of base pair step parameters shows that the intercalation happens through drug induced cavity formation which defies natural fluctuation hypothesis of DNA base pair opening during intercalation.<sup>69</sup>

**Drug Induced Minimum Base Stacking Penalty Pathway:** The detailed analysis of DNA parameters showed that intercalation happens through drug induced cavity formation by changing the non stacking DNA base pair step parameters (Twist→Shift/Slide) first and latter changing the stacking DNA base pair step parameters (Buckle/Roll → Rise). Analysis of the different energy parameters (Figure 7) with respect to the changes in the DNA base pair parameters showed that intercalation follows a base stacking penalty pathway where the increase in energy due to the un-stacking of base pair during insertion of proflavine is compensated by the decrease in the energy between drug and bases which is stabilized by stacking.

Initially, there is a decrease in the Coulombic energy (figure 7 a) because of the hydrogen bonding interaction between amino groups of

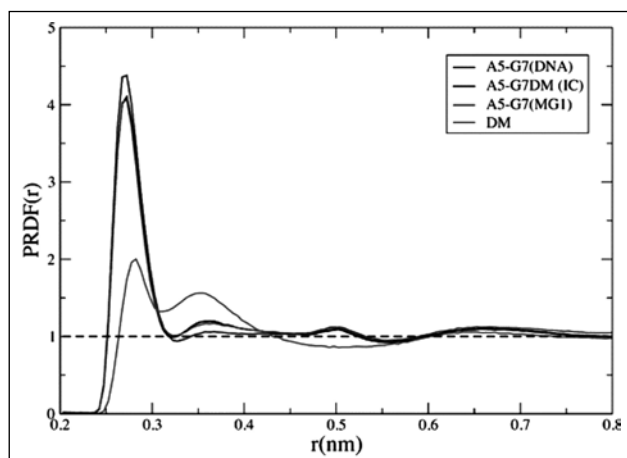


**Figure 8** Shows the proximal radial distribution function (PRDF) for free DNA, intercalated state (IC), minor groove bound state (MG1) and free daunomycin (DM)<sup>45</sup>.

proflavine and bases (figure 7 b). Up to MFEP 18, the DNA-drug energy is lower because of hydrogen bonding interaction between drug and DNA. Here the stacking energy between the bases almost remains same. At MFEP index 14, there is a sharp increase in the Roll and the drug rotates and inserts into the base pair as shown in figure 6. This decrease the stacking interaction between the intercalating base pairs and energy increases as shown in figure 7a. However, this increase in stacking energy is compensated by the decrease in the energy between drug and DNA

which stabilizes the total energy. So the major contribution to the free energy barrier comes mainly from the desolation energy because of the presence of less number of water molecules in the first hydration shell of intercalating base pair (figure 7 c) in the transition state. Here, rest of the barrier contribution may come from entropy.<sup>69</sup>

**Role of water and entropy balance in the intercalation process:** By using experimental techniques, thermodynamic aspects (both enthalpy and entropy) of intercalation process is already studied.<sup>25</sup> But the various entropic component analyses for intercalation process are still not studied. Here, the study on the various entropy component of intercalation process is carried out by doing molecular dynamics simulations on intercalated state of daunomycin in DNA, minor groove bound state of daunomycin to DNA, free DNA, free drug (daunomycin) and bulk water. For calculation of entropy both quasi-harmonic approximation (QH)<sup>74-76</sup> and permutation reduction method (PR)<sup>77</sup> has been applied. Total change in entropy ( during the binding process can be written as follows,

$$(\Delta S_{F \rightarrow B}) = S_B - S_F = \Delta S_{F \rightarrow B}^{drug-DNA} + \Delta S_{F \rightarrow B}^{water}$$

**Table 3** Shows water entropy values for binding of DM to minor groove and intercalation site of DNA.

Properties	IS (A5-G7DM)	MGS (A5-G7DM)	DNA (A5-G7)	DM	Bulk (IS)	Bulk (MGS)
Entropy/vibrational modes (kcal/mol)	1.89	1.87	1.86	1.90	1.93	1.93
$n_X^{water}$ (average water number)	126 ( $\pm 5.4$ )	128 ( $\pm 5.8$ )	111 ( $\pm 4.9$ )	58 ( $\pm 4.1$ )	43	41
$TS_{vib}$ (kcal/mol)	701.5	704.8	608.7	318.4	238.3	226.6
$T\Delta S_{F \rightarrow B}^{water}$ (kcal/mol)	12.7	4.3	0.0	0.0	0.0	0.0

where, entropy change due to daunomycin (DM) binding to DNA is written as  $\Delta S_{F \rightarrow B}^{DM-DNA} = S_B^{DNA} + S_B^{DM} - S_F^{DNA} - S_F^{DM}$ . Subscript F denotes the free state and B denotes the bound state.

The entropy change of water is calculated as  $\Delta S_{F \rightarrow B}^{water} = S_{DM-DNA}^{water} + S_F^{water} - S_{DNA}^{water} - S_{DM}^{water}$

where  $S_X^{water}$  denotes the water entropy around the system mentioned by the subscript "X".

Figure 8 shows the proximal radial distribution function (PRDF) of the selected regions of the systems such as free DNA, intercalated state (IC), minor groove bound state (MGI) and free daunomycin (DM). The PRDF gives measure of hydration layer and it gives the distribution of water molecules orthogonal to the local surface of the selected regions. For the calculation of PRDF of water molecules around free DNA, only A5-G7 triplet was selected because DM forms strong interaction with these three base pairs. Here the first coordination shell of water molecules around the triplet A5-G7 ends at 0.33nm. Free daunomycin shows a bimodal distribution which ends at 0.55 nm. In the IC and in the MGS, peak shows a small hump around 0.35 nm which shows the effect of daunomycin on the intercalated and minor groove bound states. The distribution of water molecules around DNA, IS and MGS is not conspicuous after 0.43 nm. So the size of the hydration layer is taken to be 0.43 nm for further calculations.

**Table 2 Difference in total entropy of DNA and DM in different bound states.**

TS (kcal/mol)	IS	MGS	Free state
DNA (A5-G7)	183.8	157.6	165.9
DM	55.6	51.6	59.1
Entropy ( $T\Delta S_{DM-DNA}$ )	14.4	-15.8	0.0

Table 2 shows the total entropy contribution of DNA and DM for different bound states such

as intercalated state and minor groove bound state as well as free state. The analysis showed that intercalation leads to increase in entropy of DNA and principal component analysis showed that entropy largely originates from the back bone of DNA. Due to the binding of DM to the minor groove, DM loses entropy of 9.1 kcal/mol and it loses entropy of 3.6 kcal/mol by forming the intercalated state. Due to the binding of DM to the minor groove of DNA, DNA loses entropy of 9.4 kcal/mol. So the overall entropy contribution from DM and DNA for intercalation and minor groove bound state is 14.4 kcal/mol and -15.8 kcal/mol.

Water entropy (shown in Table 3) is calculated for the systems such as free drug (DM), A5-G7 triplet of DNA, triplet-DM complex in the intercalated and minor groove bound state.

The number of water molecule expelled to the bulk water during the binding of DM to DNA is calculated by subtracting the water around the complex from water around DNA and DM separately using the equation,  $n_F^{water} = n_{DM}^{water} + n_{DNA}^{water} - n_{IS,MGS}^{water}$ .

**Table 4 Overall entropy changes for intercalation and minor groove bound state formation.**

Ts (kcal/mol)	IS	MGS	Exptl <sup>43</sup>
DM-DNA (vibrational)	14.4	-15.8	
Water (vibrational)	12.7	4.3	
translation	-14.6	-14.6	
rotation	-11.4	-11.4	
Total entropy change	1.1	-37.5	-1.1

Table 4 shows the overall entropy change for the intercalation process of DM to DNA. It shows the overall entropy of water as well as DM-DNA system. The entropy estimate for daunomycin intercalation to DNA is found to be 1.1 kcal/mol which is in excellent agreement with the experimental value -1.1 kcal/mol<sup>43</sup>. But the estimate for minor groove bound state formation is too negative to form any stable state.

## Conclusion

The extensive all atom simulations of different DNA-drug systems provided the detailed molecular mechanism of intercalation process, its thermodynamics and kinetic details, structural and conformational changes to the DNA and drug as well as an insight into the entropy components of intercalation processes. The initial study on daunomycin-DNA system showed that the intercalation happens through a two step mechanism where the drug moves to the minor groove of DNA by free energetically downhill process and finally intercalation happens through an activated process. The study also showed that Roll of DNA base pair increases first and then drug insertion happens to increase the Rise for complete intercalation. Pursuing the study on the daunomycin intercalation to DNA showed that there exists a third step for daunomycin intercalation in which it undergoes reorientation in the half intercalated state to form the final stable intercalated structure. We were able to capture the direct intercalation of proflavine to DNA by using well-tempered metadynamics simulations with the appropriate collective variable selection and configurational restraint. The detailed analysis of structural parameters of DNA showed that intercalation happens through a drug induced minimum base stacking penalty pathway where the increase in the de-stacking energy between the base pair is compensated by decrease in stacking energy between drug and DNA during the intercalation process. Thereby, the intercalation mechanism points towards drug induced cavity formation rather than natural fluctuation hypothesis of DNA causing the instantaneous base pair opening. Moreover, the study on the various entropy contributions showed that entropy balance occurs in the intercalation process as a result of the cancellation of various entropy contributions of the binding partners and water. The overall entropy for intercalation process is found to be 1.1 kcal/mol which is in excellent agreement with the experimental value -1.1 kcal/mol<sup>43</sup>

and shows that intercalation is entropy driven process.

As intercalation is a significant process through which small molecules and proteins interact with DNA, the above detailed mechanistic and free energetic study on various aspects of molecular detail of intercalation will help designing newer intercalating agents which could be used in the treatment of various cancers and microbial infections.

## Acknowledgement

The work presented here was partly done in IISER pune and partly in previous institutes of AM. Funding from IISER Pune and other sources are gratefully acknowledged. AM would like to thank the collaborators of the work: James T. Hynes, R. Lavery, M. Wilhelm, K. Zakrzewska, and B. Bouvier.

## References

1. Weiss, R. B. *Semin. Oncol.* **1992**, *19*, 670-86.
2. Minotti, G.; Menna, P.; Salvatorelli, E.; Cairo, G.; Gianni, L. *Pharmacol. Rev.* **2004**, *56*, 185-229.
3. Lerman, L. S. *J. Mol. Biol.* **1961**, *3*, 18-30.
4. Strekowski, L.; Wilson, B. *Mutat. Res.* **2007**, *623*, 3-13.
5. Tewey, K. M.; Rowe, T. C.; Yang, L.; Halligan, B. D.; Liu, L. F. *Science* **1984**, *226*, 466-468.
6. Denny, W. A.; Baguley, B. C. *Curr. Top. Med. Chem.* **2003**, *3*, 339-53.
7. Crow, R. T.; Crothers, D. M. *J. Med. Chem.* **1994**, *37*, 3191-3194.
8. Böhner, R.; Hagen, U. *Biochimica et Biophysica Acta (BBA) - Nucleic Acids and Protein Synthesis* **1977**, *479*, 300-310.
9. Sarris, A. H.; Niles, E. G.; Canellakis, E. S. *Biochimica et Biophysica Acta (BBA) - Nucleic Acids and Protein Synthesis* **1977**, *474*, 268-278.
10. Eron, L. J.; McAuslan, B. R. *Biochimica et Biophysica Acta (BBA) - Nucleic Acids and Protein Synthesis* **1966**, *114*, 633-636.
11. Snyder, R. D.; Ewing, D. E.; Hendry, L. B. *Environ. Mol. Mutagen.* **2004**, *44*, 163-73.
12. Snyder, R. D.; Hendry, L. B. *Environ. Mol. Mutagen.* **2005**, *45*, 100-5.
13. Ferguson, L. R.; Denny, W. A. *Mutat. Res.* **2007**, *623*, 14-23.
14. Wilson, W. R.; Harris, N. M.; Ferguson, L. R. *Cancer Res.* **1984**, *44*, 4420-31.
15. Li, H. J.; Crothers, D. M. *J. Mol. Biol.* **1969**, *39*, 461-&.
16. Ramstein, J.; Ehrenberg, M.; Rigler, R. *Biochemistry* **1980**, *19*, 3938-3948.
17. Bereznyak, E.; Gladkovskaya, N.; Khrebtova, A.; Dukhopelnikov, E.; Zinchenko, A. *Biophysics* **2009**, *54*, 574-580.

18. Tang, P.; Juang, C. L.; Harbison, G. S. *Science* **1990**,249, 70-2.
19. Neidle, S.; Jones, T. A. *Nature* **1975**,253, 284-285.
20. Nuss, M. E.; Marsh, F. J.; Kollman, P. A. *J. Am. Chem. Soc.* **1979**,101, 825-833.
21. Neidle, S.; Pearl, L. H.; Herzyk, P.; Berman, H. M. *Nucl. Acids Res.* **1988**,16, 8999-9016.
22. Swaminathan, S.; Beveridge, D. L.; Berman, H. M. *J. Phys. Chem.* **1990**,94, 4660-4665.
23. Paik, D. H.; Perkins, T. T. *Ang. Chem. Int. Ed.* **2012**,51, 1811-1815.
24. Neidle, S.; Jones, T. A. *Nature* **1975**,253, 284-285.
25. Chaires, J. B. *Biopolymers* **1985**,24, 403-19.
26. Rizzo, V.; Sacchi, N.; Menozzi, M. *Biochemistry* **1989**,28, 274-282.
27. Fukuyama, H.; Bihan, D. L., *Water: The Forgotten Biological Molecule*. Pan Stanford Publishing: 2011.
28. Qu, X.; Chaires, J. B. *J. Am. Chem. Soc.* **1999**,121, 2649-2650.
29. Qu, X.; Chaires, J. B. *J. Am. Chem. Soc.* **2001**, 123, 1-7.
30. Baginski, M.; Fogolari, F.; Briggs, J. M. *J. Mol. Biol.* **1997**,274, 253-267.
31. Trieb, M.; Rauch, C.; Wibowo, F. R.; Wellenzohn, B.; Liedl, K. R. *Nucl. Acids Res.* **2004**,32, 4696-703.
32. Alessandro, L.; Francesco, L. G. *Rep.Prog. Phys.* **2008**,71, 126601.
33. Barducci, A.; Bussi, G.; Parrinello, M. *Phys. Rev. Lett.* **2008**, 100, 020603.
34. Torrie, G. M.; Valleau, J. P. *J. Comp. Phys.* **1977**,23, 187-199.
35. Wang, A. H.-J.; Ughetto, G.; Quigley, G. J.; Rich, A. *Biochemistry* **1987**,26, 1152-1163.
36. Breslauer, K. J.; Remeta, D. P.; Chou, W.-Y.; Ferrante, R.; Curry, J.; Zaunczkowski, D.; Snyder, J. G.; Marky, L. A. *Proc. Natl. Acad. Sci. USA* **1987**,84, 8922-8926.
37. Qu, X.; Ren, J.; Riccelli, P. V.; Benight, A. S.; Chaires, J. B. *Biochemistry* **2003**,42, 11960-11967.
38. Huang, Y. M.; Phillips, D. R. *Biophys. Chem.* **1977**,6, 363-368.
39. Chaires, J. B.; Dattagupta, N.; Crothers, D. M. *Biochemistry* **1982**,21, 3933-40.
40. Remeta, D. P.; Mudd, C. P.; Berger, R. L.; Breslauer, K. J. *Biochemistry* **1993**,32, 5064-5073.
41. Chaires, J. *Biopolymers* **1997**,44, 201-15.
42. Rentzeperis, D.; Marky, L. A.; Dwyer, T. J.; stanger, B. H. G.-; Pelton, J. G.; Wemmer, D. E. *Biochemistry* **1995**,34, 2937-2945.
43. Chaires, J. B. *Arch. Biochem. Biophys.* **2006**,453, 26-31.
44. Ren, J.; Jenkins, T. C.; Chaires, J. B. *Biochemistry* **2000**,39, 8439-47.
45. Mukherjee, A. *J. Phys. Chem. Lett.* **2011**,2, 3021-3026.
46. Kumar, S.; Rosenberg, J. M.; Bouzida, D.; Swendsen, R. H.; Kollman, P. A. *J. Comput. Chem.* **1992**,13, 1011-1021.
47. Roux, B. *Comput. Phys. Commun.* **1995**,91, 275-282.
48. Bonomi, M.; Branduardi, D.; Bussi, G.; Camilloni, C.; Provasi, D.; Raiteri, P.; Donadio, D.; Marinelli, F.; Pietrucci, F.; Broglia, R. *Computer Physics Communications* **2009**,180, 1961-1972.
49. Mukherjee, A.; Lavery, R.; Bagchi, B.; Hynes, J. T. *J. Am. Chem. Soc.* **2008**,130, 9747-9755.
50. Morris, G. M.; Huey, R.; Lindstrom, W.; Sanner, M. F.; Belew, R. K.; Goodsell, D. S.; Olson, A. J. *J. Comput.l Chem.* **2009**,30, 2785-2791.
51. Mustard, D.; Ritchie, D. W. *Proteins* **2005**,60, 269-274.
52. Wang, J.; Cieplak, P.; Kollman, P. A. *J. Comp. Chem.* **2000**,21, 1049-1074.
53. Perez, A.; Marchan, I.; Svozil, D.; Sponer, J.; Cheatham, T. E., III; Laughton, C. A.; Orozco, M. *Biophys. J.* **2007**,92, 3817-3829.
54. Wang, J.; Wolf, R. M.; Caldwell, J. W.; Kollman, P. A.; Case, D. A. *J. Com. Chem.* **2004**,25, 1157-1174.
55. Frisch, M. J.; Trucks, G. W.; Schlegel, H. B.; Scuseria, G. E.; Robb, M. A.; Cheeseman, J. R.; Montgomery, J. A.; Vreven, T.; Kudin, K. N.; Burant, J. C., et al., *Gaussian 03, Revision C.02*. 2003.
56. Case, D. A.; Darden, T. A.; T.E. Cheatham, I.; Simmerling, C. L.; Wang, J.; Duke, R. E.; Luo, R.; Walker, R. C.; Zhang, W.; Merz, K. M., et al. *AMBER 11*, University of California: San Francisco, 2010.
57. Hess, B.; Kutzner, C.; van der Spoel, D.; Lindahl, E. *J. Chem. Theor. Comput.* **2008**,4, 435-447.
58. Sorin, E. J.; Pande, V. S. *Biophys. J.* **2005**,88, 2472-93.
59. Jorgensen, W. L.; Chandrasekhar, J.; Madura, J. D.; Impey, R. W.; Klein, M. L. *J Chem Phys* **1983**,79, 926-935.
60. Berendsen, H. J. C.; Spoel, D. v. d.; Vandrunen, R. *Comput. Phys. Commun.* **1995**,91, 43-56.
61. Nose, S. *Molecular Physics* **1984**,52, 255-268.
62. Hoover, W. G. *Physical Review A* **1985**,31, 1695-1697.
63. J.B.Chaires. *Biochemistry* **1996**,35, 2047-2053.
64. Chaires, J. B.; Dattagupta, N.; Crothers, D. M. *Biochemistry* **1985**,24, 260-267.
65. Ramstein, J.; Ehrenberg, M.; Rigler, R. *Biochemistry* **1980**,19, 3938-3948.
66. Ramstein, J.; Leng, M. *Biophys. Chem.* **1975**,3, 234-240.
67. C Ciatto, M. D. A., G Natile, F Secco, M Venturini. *Biophys J.* **1999**,77, 2717-2724.
68. Ensing, B.; Laio, A.; Parrinello, M.; Klein, M. L. *J. Phys. Chem. B* **2005**,109, 6676-6687.
69. <http://pubs.acs.org/doi/abs/10.1021/jp307911r>.
70. Wilhelm, M.; Mukherjee, A.; Bouvier, B.; Zakrzewska, K.; Hynes, J. T.; Lavery, R. *J. Am. Chem. Soc.* **2012**,134, 8588-8596.
71. Lavery, R.; Moakher, M.; Maddocks, J. H.; Petkeviciute, D.; Zakrzewska, K. *Nucl. Acids Res.* **2009**,37, 5917-5929.
72. Victor, J.-M.; Ben-Haim, E.; Lesne, A. *Phys. Rev. E* **2002**,66, 060901.
73. Christopher A, H. *J.M ol. Biol.* **1993**,230, 1025-1054.
74. Karplus, M.; Kushick, J. N. *Macromolecules* **1981**,14, 325 - 332.
75. Andricioaei, I.; Karplus, M. *J. Chem. Phys.* **2001**,115, 6289 - 6292.
76. Schlitter, J. *Chem. Phys. Lett.* **1993**,215, 617-621.
77. Reinhard, F.; Grubmuller, H. *J. Chem. Phys.* **2007**,126, 014102.



**Wilbee D. Sasikala** obtained her M.Pharm in Pharmaceutical Chemistry from Govt. Medical College, Thiruvananthapuram, Kerala, India in 2008. She did lectureship at Pushpagiri Medical College, Kottayam, Kerala, 2008-2009. She joined as a Ph.D. student in Chemistry in 2010. She is currently working on the mechanistic study of intercalation of small molecules into DNA.



**Dr. Arnab Mukherjee** obtained his M.Sc. in Chemical Sciences from Indian Institute of Science, Bangalore, India in 2001 and completed his Ph.D. in Theoretical/Computational Chemistry from Solid state and Structural Chemistry Unit of Indian Institute of Science, Bangalore, India in 2005. He carried out his post doctoral research at Ecole Normale Supérieure, Paris, France, from 2005 to 2007 and at the University of Colorado, Boulder from 2007 to 2009. He joined as Assistant Professor at Indian Institute of Science Education and Research (IISER), Pune, India in 2010. His research interests mainly focus on the mechanisms of reactions in biological systems using computational methods. He is a recipient of Indo-French Fellowship.

# Laser Based Spectroscopic Techniques to Investigate Photodissociation Dynamics

Prakash D. Naik, Hari P. Upadhyaya, Awadhesh Kumar  
*Radiation & Photochemistry Division, Bhabha Atomic Research Centre  
Trombay, Mumbai – 400 085, India*

## Abstract

Photodissociation is a simple reaction, which furnishes the dynamical insight of the reaction system. The photodissociation process provides a simplistic view of unimolecular reaction and correlation between the dynamical information and features of potential energy surface. Many of the correlations are valid for a bimolecular process as well. The population of individual states provides the microscopic details about the dissociation process. A brief description of laser photolysis-laser induced fluorescence and resonance enhanced multiphoton ionization- time of flight mass spectrometer developed in our laboratory, to obtain partitioning of the available energy into the product states, is presented in this article. The analysis of data to obtain information on photodissociation dynamic, especially distribution of the available energy into product states, is elucidated. Finally, the dynamics information is correlated to features of dissociative potential energy for some typical molecular systems.

## I. Introduction:

A photodissociation reaction is a unimolecular reaction, where the energy requirement for the reaction (fragmentation) is obtained from the absorbed photon by the molecule. When compared with the bimolecular reaction, where provides the required energy above the threshold and leads the reaction towards the product side via a transition state, the photodissociation from an excited molecule corresponds to the latter half of the bimolecular reaction. To explain the reaction dynamics it is better to explain the molecules in terms of the landscape, a plot of potential energy as a function of various molecular coordinates, known as potential energy surface (PES). Molecules have a ground electronic state, the lowest energy electronic state, and a large number of excited electronic states, each having its characteristic PES. The features of PES and the point of access on it by an absorbed photon determine the outcome of the prepared excited state. If the access point lies in a pond and has no crossing with any dissociative surface, either repulsive or having mountain peak (transition

state) lower than the accessed point, then we expect either fluorescence or phosphorescence from the excited molecule. If the access point lies on the steep slope of an excited state surface, then the molecule get fragmented on this surface and the process called direct dissociation takes place. The other processes involving crossing over to a dissociative surface, either through the intersection of two excited states or through the avoided crossing of two excited states, are called indirect dissociation. To obtain the microscopic information, state resolved measurements are employed, where the populations of individual states are probed to obtain the microscopic details about the dissociation process. The kind of distribution of the available energy partitioning into the product states indicates the nature of the dissociation process, a non-statistical distribution suggests a direct dissociation, where dissociation occurs on a time scale shorter than the rotational period of the molecule. On the other hand, a statistical distribution points out the complex nature of a dissociation mechanism, with the dissociation lifetime longer than the rotational

period of the molecule. We have developed and employed two versatile techniques, laser induced fluorescence and resonance enhanced multiphoton ionization- time of flight mass spectrometer, to probe the partitioning of the available energy among different states of a photofragment, and deduced the photodissociation dynamics of some atmospherically important molecules.

In this article, we have presented a brief description of laser photolysis-laser Induced fluorescence (LP-LIF) and resonance enhanced multiphoton ionization- time of flight mass spectrometer (REMPI-TOF) facilities developed in our laboratory. The analysis of data to obtain the microscopic details of the photodissociation process, especially distribution of the available energy into product states, is also discussed. Finally, the dynamics information is correlated to features of the dissociative potential energy surface for some typical molecular systems.

## II. EXPERIMENTAL

### 1. Laser Photolysis Laser Induced Fluorescence Spectroscopy for photodissociation Dynamics investigation

The method based on fluorescence phenomenon, laser-induced fluorescence (LIF) technique, has now become the most widely used laser diagnostic technique in many research fields.<sup>1,2</sup> LIF technique involves the absorption of radiation of a very precise wavelength by atomic/molecular species, and monitoring of subsequent emission from the excited species. It serves as a state selective probe of chemical species. In order to apply the LIF technique to a given chemical species, to measure its state specific concentration, it is desirable that the band system to be accessed by the LIF technique is spectroscopically well studied and analyzed. In UV-visible LIF technique, the population of molecules from a rovibrational state in the ground state is transferred to a rovibrational state in the excited electronic state, using a laser tuned to the requisite wavelength. It is possible to excite from a particular rovibrational state in the ground state

to a particular rovibrational state in the excited state in case of a gaseous medium, provided the spectral bandwidth of the laser employed is less than the rotational-state spacing.

The excitation source generally used in the LIF technique is a tunable dye laser, or an optical parametric oscillator, which has an advantage over the conventional light source in terms of spectral brightness and width. The usefulness of LIF as a diagnostic tool results from the fact that the intensity of the fluorescence signal,  $I_{\text{lif}}$ , is proportional to the population of the species in the excited state, which is related to the initial ground state population before laser excitation. Although, in principle, it can be used for detecting single molecular species, in practice, for most of the systems one might obtain sensitivity of  $10^6$  particles per cubic centimeter.

The schematic of the setup developed at Radiation & Photochemistry Division, B.A.R.C. for investigating photodissociation dynamics of atmospherically important molecules producing OH radical on photoexcitation, is shown in Figure 1. The photolysis laser employed is an excimer laser (Lambda Physik Model Compex-102, Fluorine version). The probe beam is the second harmonic output of a dye laser (Quantel, TDL90), pumped by the second harmonic (532 nm) of a seeded Nd:YAG laser (Quantel, YG980 E-20). The dye laser is operated with DCM(4-dicyanomethylene-2-methyl-6-(*p*(dimethylamino)styryl)-4*H*-pyran) special dye, with the fundamental wavelength tuning range of 600–640 nm. The photolysis and the probe laser beams traverse orthogonally through two pairs of windows to intersect at the centre of the reaction chamber, which is made of stainless steel and equipped with five arms and three ports for a pressure transducer, gas inlet and a vacuum pump. The two orthogonal pairs of arms are provided with  $\text{MgF}_2$  and quartz windows at the Brewster angle, to facilitate transmission with reduced scattering of the photolysis and the probe beams, respectively. The fifth bottom arm is used to collect the fluorescence. The fluorescence is

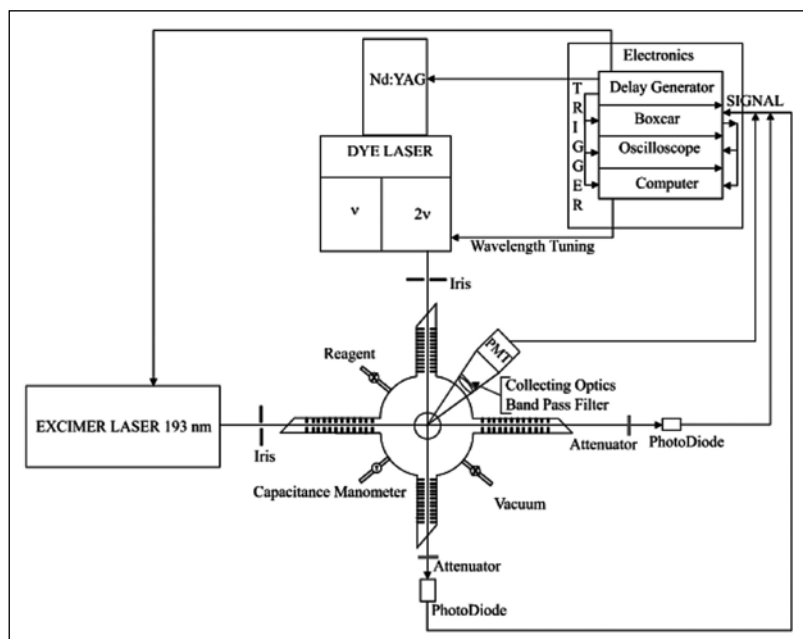


Figure 1: Schematic diagram of the LP-LIF experimental set-up.

collected by a 38 mm diameter lens of focal length 50mm, and detected by a photomultiplier tube (PMT, Hamamatsu, model R 928P). A band-pass filter ( $\lambda_{\text{centre}} = 310 \text{ nm}$ , FWHM (full width at half maximum) =  $\pm 10 \text{ nm}$ ,  $\%T_{310 \text{ nm}} = 10$ ) is placed between the collecting lens and the PMT, to cut off the light scattered from the photolysis laser.

The fluorescence signal is gate-integrated by a boxcar (SRS 250), which involves the integration of the signal within a specific time window and averaging the repetitive signal to improve the signal-to-noise ratio, for 30 or 100 laser shots, and fed into an interface (SRS 245) for A/D conversion. A PC is used to control the scan of the dye laser via an RS232 interface and to collect data through a GPIB interface, using a control and data acquisition program. To correct for the laser intensity fluctuations, both the pump and the probe lasers are monitored by photodiodes, and the fluorescence intensities are normalized. The laser frequency is calibrated using an optogalvanic cell (Fe-Ne), with an accuracy of  $\pm 0.3 \text{ cm}^{-1}$ . The spectral resolution of the probe laser is  $0.06 \text{ cm}^{-1}$ . The vapour of the compound flowed through the reaction chamber at a flow velocity of approximately  $10 \text{ cm s}^{-1}$ .

The pressure was maintained at less than 100 mTorr, which was measured using a capacitance gauge (Pfeiffer vacuum). The OH fragment was probed state-selectively by exciting the  $A^2\Sigma \leftarrow X^2\Pi (0,0)$  transition of OH (306–309 nm) and monitoring the subsequent  $A \rightarrow X$  fluorescence. Both the laser beams were unfocused and attenuated to prevent saturation and multiphoton events and the LIF signal was confirmed to be linearly proportional to the laser power. Further, for a main branch and the adjacent satellite branch lines probing the population of the same state, the ratio of their LIF intensities should be equal to the ratio of their Einstein coefficients, if there is no saturation

in the LIF signals. The Einstein coefficients for the main branches are around 10 times higher than those for their satellite branches. Hence, the saturation in LIF intensities was estimated from the ratio of their intensities, and was found to be negligible. The LIF spectra were measured at pump-probe delays of 50 and 200 ns, and found to be identical, thereby ensuring that the collisional relaxation was negligible. The LIF intensities were measured as a function of the substrate pressure, and found to be linear with the substrate sample used. Substrates (>98.0% purity) were used as supplied, after performing several freeze-pump-thaw cycles. During irradiation, the windows of the photolysis laser developed a thick coating from the deposits of some photoproducts, which were cleared regularly during the experiment to avoid the attenuation of the laser energy.

The typical LIF spectra, with appropriate assignments,<sup>3</sup> are shown in Figure 2 for the (0,0) band of the A-X system of OH, produced from acetic acid on photodissociation at 193 nm. The P, Q and R branches refer to rotational transitions with  $\Delta N = -1, 0$  and  $1$ , respectively. The subscripts 1 and 2 represent the transitions

$\Delta J=N+1/2 \leftarrow \Delta J=N+1/2$  and  $\Delta J=N-1/2 \leftarrow \Delta N-1/2$ , respectively, whereas the subscripts 21 and 12 represent the transitions  $\Delta N-1/2 \leftarrow \Delta N+1/2$  and  $\Delta N+1/2 \leftarrow \Delta N-1/2$ , respectively. Thus, the transitions represented by subscript 1 and 21 originate from  $\prod_{3/2}$ , whereas those represented by 2 and 12 originate from the  $\prod_{1/2}$  spin-orbit state. According to the parity selection rule ( $+\leftrightarrow -$ ), the Q-branch arises from the  $\prod^- (A')$  state, while the P and R branches originate from the  $\prod^+(A'')$  state. The relative populations of the OH fragment were determined by normalizing the respective peak area of the rotational lines with respect to pump and probe laser intensities, pressure change, if any, and the respective Einstein absorption coefficients  $B_{ij}$ .<sup>4</sup> The spin-orbit and the  $\Lambda$ -doublet ratios were calculated from the relative populations of the different states. The translational energy associated with the OH fragment was calculated from the Doppler profiles of the rotational lines. In the following section, we will describe some of the important parameters monitored, and discuss their implications.

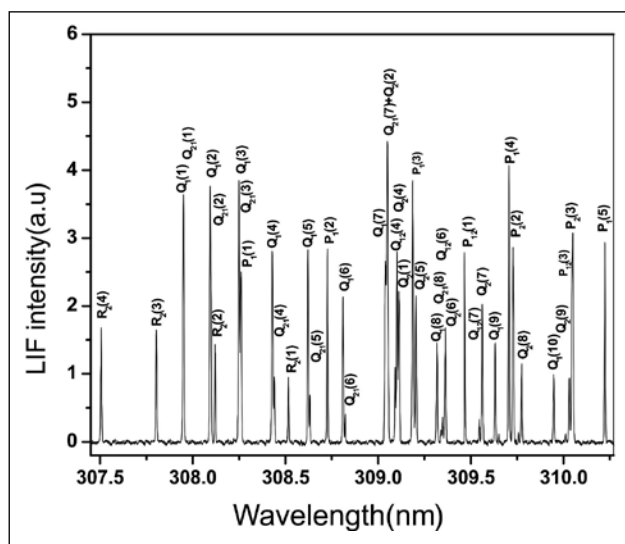


Figure 2. A typical LIF excitation spectrum of the (0,0) band of the  $A^2\Sigma^+ \leftarrow X^2\Pi$  system of the nascent OH product from photodissociation of unsaturated alcohol.

### 1.1 Rotational State Distribution:

The nascent rotational state populations of OH radicals generated on photodissociation

were used to construct a Boltzmann plot, for obtaining the rotational temperature of nascent OH fragments. The average rotational energy,  $\langle E_R \rangle$ , of the OH fragment can be estimated after summing over the rotational excitation in a particular vibrational state populated,

$$\langle E_R \rangle = \sum P(J'') E_R(J'') \quad (1)$$

where  $P(J'')$  is probability of the rotational state distribution and  $E_R(J'')$  is the energy of a given rotational level  $J''$  in the selected vibrational level.

### 1.2 Estimation of Vibrational State Distribution:

Assuming a Boltzmann distribution, a vibrational temperature can be obtained from the ratio of the normalized LIF intensities of the same rotational excitation line of the various vibrational levels.

### 1.3 Average translational energy of OH

Molecular velocity of the fragments leads to the Doppler broadening of the LIF lines. The averaged translational energy of the photoproduct OH can be estimated using widths of Doppler broadened rotational lines. The typical Doppler profile of the  $Q_2(6)$  line of OH is shown in Figure 3. After correcting the Doppler profile of the rotational lines for the probe laser linewidth, the linear Doppler width  $\Delta v_D$  is related to the temperature ( $T_r$ ) by the equation,<sup>1</sup>

$$\Delta v_D = 7.16 \times 10^{-7} v_0 \sqrt{\frac{T_r(OH)}{m_{OH}}} \quad (2)$$

where  $v_0$  and  $m_{OH}$  represent the centre frequency of the rotational line and the mass of OH, respectively. The average translational energy in OH,  $E_T(OH)$ , is given by eq. (3),

$$E_T(OH) = \frac{3}{2} k T_r(OH) \quad (3)$$

### 1.4 Spin-Orbit State Distribution

The spin-orbit ratio, generally known as the  $F_1/F_2$  ratio, which gives the relative population in ( $\prod_{3/2}$ ) and ( $\prod_{1/2}$ ) states, was obtained from the ratio of the populations,  $P_1(N'')/P_2(N'')$ ,  $Q_1(N'')/$

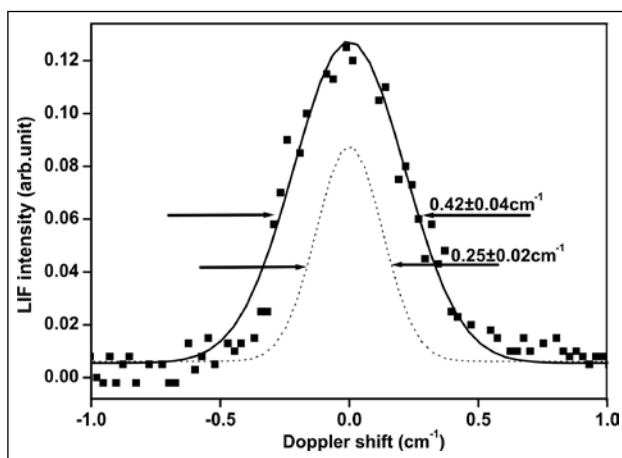


Figure 3: A typical Doppler profile of  $P_1(2)$  line of the  $A^2\Sigma^+ \leftarrow X^2\Pi (0,0)$  system of the OH radical produced in dissociation of unsaturated alcohol with 193 nm laser. The dotted line represents the laser spectral profile.

$Q_2(N'')$ , and so on. For  $F_1(N'')$  and  $F_2(N'')$ , the  $J''$  values are not the same, hence the population was normalized with a statistical weight factor,  $2J'' + 1$ .

### 1.5 Population of the $\Lambda$ -doublets

The  $\Lambda$ -doublets arise from the orientation of the  $\pi$ -lobes of OH with respect to the plane of rotation. In the  $\Pi^+(A')$  state, the  $\pi$ -lobe lies in the plane of rotation, while in the  $\Pi^-(A'')$  state, the  $\pi$ -lobe is perpendicular to the plane of rotation. The doublet ratio  $[\Pi^-(A'')/\Pi^+(A')]$  was obtained from  $Q_1(N'')/P_1(N'')$  or  $Q_1(N'')/R_1(N'')$ . For  $Q_1(N'')$ ,  $P_1(N'')$  and  $R_1(N'')$ , since the  $J''$  values are the same, normalization of populations is not required. The relative populations of the  $\Lambda$ -doublets provide information about the exit channel dynamics during the breaking of the chemical bond.

## 2. REMPI -Time-of-flight mass spectrometer

We have developed a molecular beam time-of-flight mass spectrometer system (MB-TOF-MS), Figure 4, for measuring the photodissociation dynamics of channels forming atomic species and used extensively for obtaining the photodissociation dynamics of halogen

atom (Cl, Br) formation. A supersonic beam of reactant of interest was generated from a pulsed nozzle + skimmer arrangement, which intersects a laser beam in the ionization region of the TOF assembly. A detailed description of the experimental setup is given in our previous paper.<sup>5</sup> In brief, a pulsed supersonic molecular beam was generated using a solenoid valve, with a 0.8 mm nozzle and 500  $\mu$ s opening time, and a 1.9 mm diameter conical skimmer. A Time-of-flight mass spectrometer (TOF-MS), two-stage Wiley-McLaren type,<sup>6</sup> was mounted vertically, perpendicular to the horizontal MB, with 18 mm dual microchannel plates as detector. The MB was characterized using a fast ion gauge (FIG). The vapours of reactant, seeded in helium, was obtained by bubbling helium through a sample maintained at room temperature. The contribution to the measured TOF signal from cluster photofragmentation was minimized by performing experiments at a low stagnation pressure ( $< 1000$  Torr), and using only the rising part of the molecular beam pulse. We have employed a single colour laser for both photodissociation of the parent molecule and ionization of the atomic photoproducts. A Nd:YAG laser (YG-981-C, Quantel), operating at 20 Hz, pumped dye laser (TDL 90, Quantel, using rhodamine 101 dye) was employed for generating the requisite laser beam. The fundamental dye laser output, after frequency-doubling in a KDP crystal, was mixed with the fundamental output of the Nd:YAG laser to obtain an output in the range 230-236 nm. A set of four Pellin-Broca prisms was used to separate the above laser output from the rest of laser beams. Doppler broadening of the transitions studied was always well within the above laser bandwidth. The laser beam was passed through a converging lens of 200 mm focal length, and the distance between the lens and the interaction zone was adjusted to obtain the best ratio of on- and off-resonant signals.

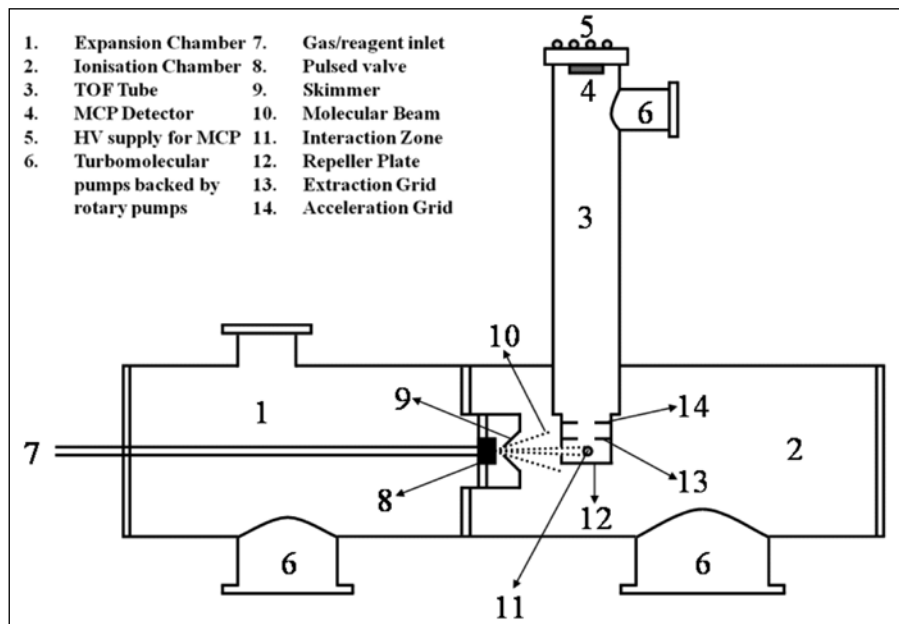


Figure 4: Schematic of REMPI-TOF setup.

All the instruments were time synchronized using a digital delay/pulse generator of 20 ps pulse resolution. The ion signal from MCP was fed to a boxcar gate integrator and after averaging for 30 laser pulses, passed on to an interface (SRS 245) for A/D conversion. A PC was used to control the scan of the dye laser via an RS232 interface, and collect data from SRS 245, through a GPIB interface, using a control and data acquisition program. For obtaining TOF spectrum, the MCP signal was fed to a 500 MHz digital oscilloscope (LeCroy 9350A), which was interfaced to a Pentium PC. The contributions to the signal from pump-oil related background and the multiphotonic processes were removed by subtracting the off-resonant signals from the on-resonant signals. The laser power was monitored, using a power meter, and was typically 50–100  $\mu\text{J}/\text{pulse}$ . The power dependence measurements were performed by integrating the Cl/Br atom REMPI spectra.

A double Fresnel rhomb was used for rotation of the laser beam polarization entering the chamber. TOF profiles were taken for three different experimental configurations, *vertical* (laser polarization  $\parallel$  detection axis),

*horizontal* (laser polarization  $\perp$  detection axis), and *magic angle* (laser polarization at  $54.78^\circ$  to the detection axis).

### 2.1 Analysis of TOF profile

The measured TOF profile corresponds to the component of the photofragment that speeds along the TOF-MS axis, which defines the lab frame Z axis. The speed component results from the averaging of the angular distribution over the photofragment speed distribution  $g(v)$ , and is given as,<sup>7-9</sup>

$$f(v_z, \chi) = \int_{|v_z|}^{\infty} \frac{g(v)}{2v} \left[ 1 + \beta P_2(\cos \chi) P_2\left(\frac{v_z}{v}\right) \right] dv \quad (4)$$

where  $v_z$  is the velocity component along the Z axis,  $v$  is the recoil speed of the fragments,  $\beta$  is the anisotropy parameter,  $P_2(\cos \chi)$  is the second Legendre polynomial, and the  $\cos(\chi) = \hat{\epsilon} \cdot \hat{z}$ , used in the above equation is the projection of the pump laser electric field,  $\hat{\epsilon}$ , on the detector axis,  $\hat{z}$ , which is also defined as the angle between the dissociation laser polarization and the Z axis.

The major task of the analysis procedure is to extract the photofragment speed distribution,  $g_i(v)$ , and anisotropy,  $\beta_i$ , of each decay channel  $i$  active in the photodissociation, and hence contributing to the experimental TOF profiles  $I(v_z, \chi)$ . We have used an intrinsically numerically stable forward convolution method. The detail of the adopted procedure has been described elsewhere.<sup>5</sup> Here, an initial c.m. photofragment speed distribution  $g_i(v)$  was assumed for each active decay channel  $i$  and modeled with the functional form,<sup>10,11</sup>

$$g_i(v) = (f_T)_i^{a_i} [1 - (f_T)_i]^{b_i} \quad (5)$$

where  $(f_i)_i$  is the fraction of the available energy channeled into translational modes,  $E_i^{trans} / E_i^{avail}$ , and  $a_i$  and  $b_i$  are adjustable parameters. By adjusting anisotropy parameter  $\beta_i$  and weight for each decay channel,  $f(v_z, \chi)$  was simultaneously calculated for the geometries  $\chi=0^\circ, 54.78^\circ$  and  $90^\circ$ . Convolution of  $f(v_z, \chi)$  with the instrument response function yielded the simulated TOF profiles, which were compared with the experimental results. The photofragment speed distribution,  $P(v)$ , were converted into the center-of-mass translational energy distribution,  $P(E_T)$  and the average translational energy were calculated. Typical REMPI-TOF profiles of  $\text{Cl}(^2P_{3/2})$  produced from the 234 nm photodissociation of chlorinated hydrocarbon are depicted in Figure 5., for the geometries  $\chi=0^\circ, 54.78^\circ$  and  $90^\circ$  and the corresponding photofragment center-of-mass translational energy distribution,  $P(E_T)$  in Figure 6.

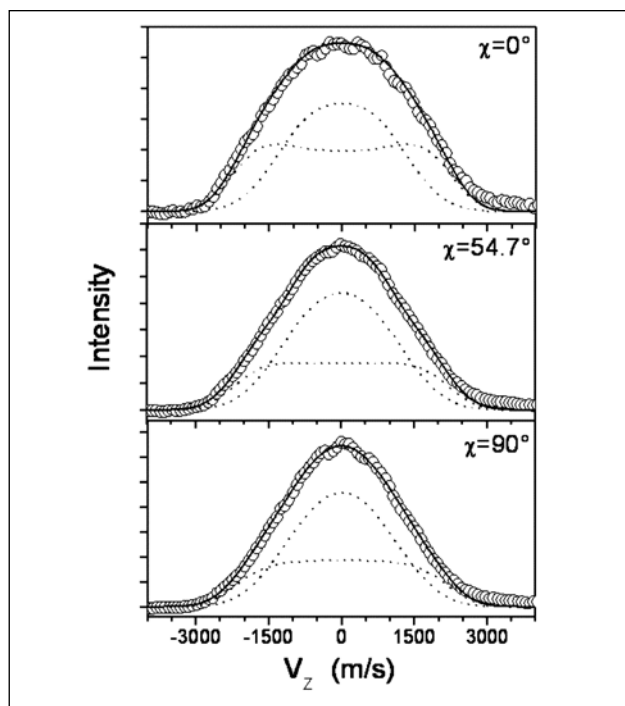


**Figure 5.** Typical REMPI-TOF profiles of  $\text{Cl}(^2P_{3/2})$  produced from the 234 nm photodissociation of chlorinated hydrocarbon. The circles are the experimental data, the dashed lines are forward convolution fit for two different channel and the solid line shows the sum. Three panels, namely, upper, middle and lower panels correspond to experimental geometries with  $\chi = 0^\circ, \chi = 54.7^\circ, \chi = 90^\circ$  respectively.

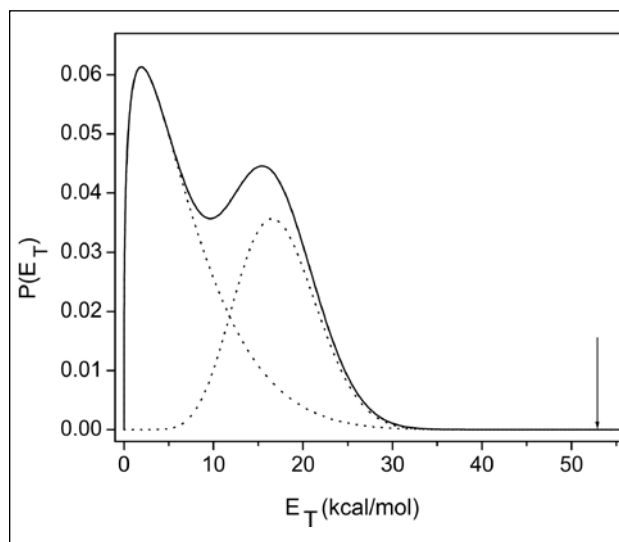


**Figure 6.** Photofragment centre-of-mass translational energy distribution of chlorine atom  $\text{Cl}(^2P_{3/2})$  elimination channel for the 234 nm dissociation of chlorinated hydrocarbon. The dashed lines indicate the speed distributions for the fast and slow component; the solid line shows the sum.

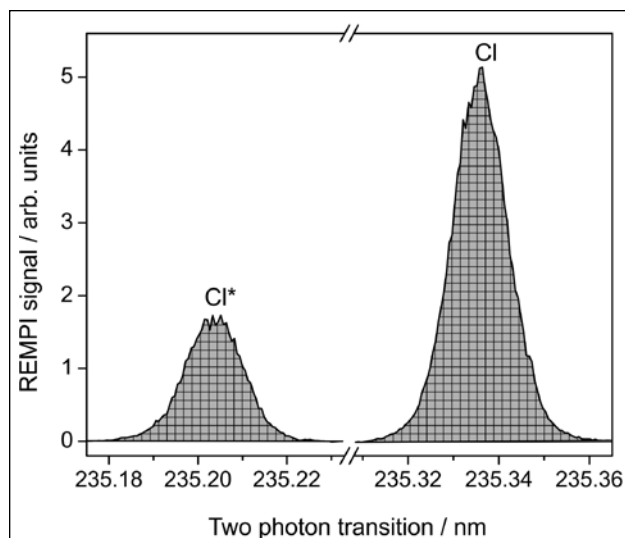


**Figure 7.** Profiles of  $\text{Cl}$  and  $\text{Cl}^*$  atoms produced in the 234 nm laser photolysis of chlorinated hydrocarbon used for the determination of their ratio.

## 2.2 Spin-orbit branching ratio

The ground  $X(^2P_{3/2})$  and the spin-orbit excited  $X(^2P_{1/2})$  atomic halogen photoproducts were scanned in the region of their two photon transitions, a typical scan is shown in Figure 7. The ion intensity due to a species  $X$ ,  $S(X)$ , is obtained by integrating the measured ion signal

intensity over the proper range containing the Doppler width and the probe laser bandwidth. The ratio of number density of  $X^*$ ,  $N(X^*)$  and  $X$ ,  $N(X)$  species is related to the measured ion intensity ratio by an expression,

$$\frac{N(X^*)}{N(X)} = k \frac{S(X^*)}{S(X)} \quad (6)$$

where  $k$  represents the relative ionization probability.

## DISCUSSIONS

### 1. Energy partitioning and dynamics of dissociation process

The available energy in the photodissociation process is related to the photolysis photon wavelength by the relation,  $E_{\text{avl}} = E_{\text{int}}(\text{reactant}) + h\nu - D_0$ , where  $E_{\text{int}}(\text{reactant})$  is the initial internal energy of the reactant molecule,  $h\nu$  is the photolysis photon energy, and  $D_0$  is the dissociation energy of the molecule for forming the fragments in their lowest possible energy states from the lowest possible energy state of the reactant molecule. The available energy is partitioned into the fragments internal energy, electronic ( $E_E$ ), vibrational ( $E_V$ ) and rotational ( $E_R$ ), and relative translational energy ( $E_T$ ). In most of the cases, the fragments are in electronically ground state and the fraction of the available energy in vibrational ( $f_V$ ) and rotational ( $f_R$ ) and relative translational energy ( $f_T$ ) are estimated from  $E_i/E_{\text{avail}}$ .

### 2. Triatomic system

The simplest molecular system, which correlates the partitioning of the available energy in internal and translational states of the photofragments is triatomic species. In many triatomic molecule the energy partitioning is mapped by probing the diatomic system, state selectively. Table. 1 shows the energy partitioning in some of typical triatomic molecular systems. On the first glance it seems that the preferred box (mode) for the available energy deposition is either translational or vibrational mode, while

rotation is moderate, in most of the cases. On relating the energy disposal on type of the bond cleaved during the dissociation process, it is observed that the cleavage of a single bond between the atoms leads to high translational and low vibrational energy energy release, while the cleavage of multiple bonds between the atoms releases greater energy in vibration and lower in translation. The above simple generalization arises due to the nature of transition state in the cleavage of single and multiple bonds, which are loose and tight, respectively. This generalization is somewhat crude, as the dissociation process involves the trajectory of the molecule on the adiabatic or non adiabatic potential energy surface/s and thus the nature of dissociating bond should not be the sole criterion. This is clearly seen by the exception to the above bond type-energy disposal relationship by some of the molecular systems. It is quite obvious that the features on the potential energy surface should play a role in energy disposal mechanism and as a simple step in this direction the structure of the reactant molecule, the transition state, if any, and fragment molecules, should be invoked to explain the energy partitioning.

#### 2.1 Energy deposition in vibrational mode

In the excitation process in which quasi-equilibrium BC distance in ABC, on the upper surface is rather different from that in the fragment BC molecule, the diatomic fragment BC is vibrational excited. In Franck-Condon model, the wave function of the parent molecule is projected onto the quasistable vibrational wave functions of the upper state and not onto fragment wave functions. Thus, in molecules where the probability of delocalization of electronic energy is very high, the available energy largely flows into the vibration modes of the photofragment.

#### 2.2 Energy deposition in rotational mode

Despite possibility of V and R coupling due to coriolis forces, the overall rotational excitation in the photoexcited molecules remain small, because of extremely small time that the molecule

spends in the transition state region. The overall parent rotation remains small up to a moment of actual bond cleavage and only when the molecule actually dissociates, the bending type vibrations and torsions couple with the parent rotation and evolve into the product rotation and orbital angular momentum.

There are three ways to channelize the available energy into rotational mode of photofragments. Firstly, a part of the rotational angular momentum of the parent is mapped as rotational angular momentum of the diatomic fragment. Secondly, if the parent molecule is linear and has low frequency bending vibration, a lot of energy is stored in these vibrational manifolds, which on dissociation gets converted into photofragment rotational energy. Third and the most important driving force for rotational excitation is the torque exerted during the bond cleavage process. The torque in a simple bond cleavage process, as in triatomic ABC, is generated due to the antibonding repulsion between atoms attached to the cleaved bond or change in ABC bond angle in the excited state. The magnitude of torque depends on the force applied, the length of the *lever arm* connecting the axis to the point of force application, and the angle between the force vector and the lever arm. If molecule in the excited state is bent, the torque exerted will be more and hence more rotational excitation of photofragments.

### 2.3 Energy deposition in translational mode

It is observed that when a dissociative surface is repulsive in nature then the excess energy is consumed in separating the fragments, and thus it ends up as translational energy of the fragments. Similarly, if there is an exit barrier on the dissociative surface, connecting the parent molecule to fragments, the barrier energy flows into the translational mode, while descending the potential energy barrier. A simple bond cleavage reaction on the ground state PES, usually doesn't encounter an exit barrier and translational mode is populated statistically.

## 3. Some Typical Cases

### 3.1 Photolysis of H<sub>2</sub>O

The photodissociation of water below 193 nm has been studied extensively. It is interesting to observe from Table 1 that at 153 nm excitation of H<sub>2</sub>O, the fragment OH is produced with very low rotational energy,  $f_R=0.04$ , while at 130 nm, OH is formed with very high rotational energy,  $f_R=0.8$ . The formation of the OH fragment with low rotational energy can be easily explained on the basis of non availability of low frequency bending vibrational mode in the parent molecule, H<sub>2</sub>O, and small length of the lever arm of the force exerted during O-H bond cleavage process, as the centre of mass in H<sub>2</sub>O is very close to the central atom, O atom, resulting into very small torque. However, very high rotational energy in the OH fragment, at 130 nm excitation, is quite puzzling. The features of excited state PES, generated theoretically, have thrown light on this unusual high rotational energy in the photofragment. At 130 nm, the accessed electronic state is B <sup>1</sup>A' state, and on this state, the equilibrium geometry of H<sub>2</sub>O is collinear. Thus immediately after the excitation the molecule changes from the bent structure (ground state geometry) to the collinear structure generating a torque, and as dissociation is very fast, due to conical intersection to the ground state, the torque will result into rotational excitation of the photofragment OH.

### 3.2 Photolysis of ClCN

The available energy partitioning in the photofragments of ClCN, on excitation at 193 and 147 nm, has been determined and found to be greatly dissimilar, Table 1. At 147 nm excitation of ClCN, the fraction of the available energy partitioned in rotational is 0.2, similar to that of other XCN, however at 193 nm, a much higher fraction is partitioned in the rotational states. This is unexpected as molecule is 16 valence electron systems and as per Walsch rule it should be a linear molecule. For obtaining such a large rotational excitation, the molecule must attain a nonlinear configuration during or before bond cleavage on the excited surface.

**TABLE 1. : Average energy partitioning in photofragments states**

Molecule	$\lambda$ -photo-lysis	Channel	$f_T$	$f_v$	$f_R$
H <sub>2</sub> S	193 <sup>12</sup>	H + HS	0.96	0.04	0
H <sub>2</sub> O	157 <sup>13</sup>	H + OH	0.96	0	0.04
H <sub>2</sub> O	130 <sup>14</sup>	H + OH	0.14	0.06	0.80
ICN	266 <sup>15</sup>	I + CN	0.90	0	0.10
ICN	147 <sup>16</sup>	I + CN	0.63	0.18	0.19
CINO	347 <sup>17</sup>	Cl + NO	0.70		
CINO	193 <sup>18</sup>	Cl + NO	0.30	0.59	0.11
CINO	150 <sup>18</sup>	Cl + NO	0.81	0.05	0.14
OCS	157 <sup>19</sup>	S + CO	0.16	0.84	0
CICN	193 <sup>20</sup>	Cl + CN	0.52	0.03	0.45
CICN	147 <sup>16</sup>	Cl + CN	0.72	0.08	0.20
NO <sub>2</sub>	337 <sup>21</sup>	O + NO	0.3	0.51	0.16
NO <sub>2</sub>	248 <sup>22</sup>	O + NO	0.5	0.85	

### 3.3 Photolysis of CINO

The photodissociation dynamics of CINO has been studied at various wavelength of excitation, Table 1. Being a molecule with valence structure, the cleavage of the Cl-N single bond forming Cl + NO is expected to release the major fraction of the available energy into product translational. Although  $f_T$  of 0.81 and 0.70 were measured at 150 and 347 nm excitation, respectively,  $f_T$  at 193 nm is just 0.3. These surprising results were explained from the theoretical studies of excited state PES. The studies predicted a direct dissociation at 347 nm and cross over from the prepared Rydberg state to the repulsive surface at 150 nm, thus channelizing a major fraction of the available energy into product translational. However, at 193 nm the dissociation seems to be indirect, where the prepared excited quasistable state crosses over to either triplet or vibrational hot ground state. This results into reduction of the preferential flow of available energy in the translational mode substantially.

### 3.4 Photolysis of Acetic acid

Acetic acid was photolysed at 193, 200 and 218 nm and OH was observed as a primary photofragment.<sup>23-25</sup> The decomposition dynamics leading to the OH formation channel was probed by determining the available energy partitioning in internal and translational states of OH. It was found that most of the available energy is deposited as translational energy of the fragments. At the above excitation wavelengths, the transition is <sup>1</sup>(n, P\*), where the electron localised on the non-bonding carbonyl oxygen is promoted to the anti-bonding carbonyl carbon, thus giving a pyramidal excited state as compared to the planar ground state geometry. In pyramidal geometry the carbonyl C=O bond is extended, resulting into cleavage of stronger C-O single bond over the weaker C-C single bond. The energy partitioning indicates the existence of an exit barrier of 13 kcal/mol, which has been confirmed recently, by a theoretical calculation.

### 3.5 Photolysis of PCl<sub>3</sub>

The photodissociation dynamics of phosphorus trichloride (PCl<sub>3</sub>) has been studied in a supersonic beam by resonance enhanced multiphoton ionization (REMPI), using time-of-flight (TOF) mass spectrometry.<sup>5</sup> The study is focused on the nascent state of the primary chlorine atom, formed on excitation of the (n,  $\sigma^*$ ) transition of the molecule around 235 nm. Dissociation of PCl<sub>3</sub> and the REMPI detection of chlorine atoms are performed, using the same laser around 235 nm. The photofragments, namely, Cl(<sup>2</sup>P<sub>3/2</sub>) and Cl\*(<sup>2</sup>P<sub>1/2</sub>), the recoil anisotropy parameter  $\beta$ , and the spin-orbit branching ratio for chlorine atom elimination channels, have been determined. Polarization-dependent and state-specific TOF profiles are converted into kinetic energy distributions, using a least-squares fitting method, taking into account the fragment anisotropies. The anisotropy parameters for Cl and Cl\* are characterized by values of  $0.0 \pm 0.05$  and  $0.20 \pm 0.05$ , respectively. Two components, namely, the fast and the slow, are observed in the speed distribution ( $P(v)$ ) of Cl and Cl\* atoms,

formed from different potential energy surfaces. The average translational energies for the Cl and Cl\* channels for the fast component are 29.7 and 30.6 kcal/mol, respectively. Similarly, for the slow component, the average translational energies for the Cl and Cl\* channels are 9.5 and 9.1 kcal/mol, respectively. The energy partitioning into the translational modes is interpreted with the help of an impulsive model, for the fast component, and a statistical model, for the slow component. Apart from the chlorine atom elimination channel, molecular chlorine (Cl<sub>2</sub>) elimination is also observed in the photodissociation of PCl<sub>3</sub>. The observation of the molecular chlorine in the dissociation process and the bimodal translational energy distribution of the chlorine atom clearly indicate the existence of a crossover mechanism from the initially prepared state to the ground state.

#### IV. CONCLUSIONS

We have presented the laser based sensitive and state selective techniques, laser photolysis-laser Induced fluorescence and resonance enhanced multiphoton ionization-time of flight mass spectrometer, for obtaining distribution of the available energy partitioning into the product states. From the correlation between the energy partitioning in product states and excited state surface, it can be concluded that the shape of the excited state PES and its interaction with other nearby states decides the energy distribution. The repulsive nature or the presence of an exit barrier directs the major part of the available energy in translational mode. The cross over to the vibrationally hot ground state usually ends up with moderate energy in the translational mode. The presence of tight transition state on the dissociative surface leads to high vibrational energy in fragments. The rotational energy in the fragments depends on the presence of low frequency bending modes in non-spectator moiety in the parent molecule, rotational energy of the parent molecule and lever arm of the bond cleavage force.

#### ACKNOWLEDGMENTS

Authors sincerely acknowledge the support and encouragement from Dr. P.N. Bajaj, Dr S.K. Sarkar and Dr T. Mukherjee throughout the course of this work.

#### REFERENCES

1. Demtroder, W. Laser spectroscopy (Springer, New Delhi) **2004**.
2. Dagdigan, P. J.; Cruse, H.W.; Schultz, A.; Zare, R. N. *J. Chem. Phys.* **1974**, 61, 4450
3. Dieke, G. H.; Crosswhite, H. M. *J. Quant. Spectr. Radiat. Transfer* **1961**, 2, 97.
4. Chidsey, I. L.; Crossley, D. R. *J. Quant. Spectr. Radiat. Transfer* **1980**, 23, 187.
5. Upadhyaya, H. P.; Saha, A.; Kumar, A., Naik, P. D.; Bajaj, P.N. *J. Phys. Chem. A* **2010**, 114, 5271.
6. McMillen, D. F.; Golden, D. M. *Ann. Rev. Phys. Chem.* **1982**, 33, 493.
7. McGivern, W. S.; Li, R.; Zou, P.; North, S. W.; *J. Chem. Phys.* **1999**, 111, 5771.
8. Vasudev, R.; Zare, R. N.; Dixon, R. N.; *J. Chem. Phys.* **1984**, 80, 4863.
9. Dubs, M.; Bruhlmann, U.; Huber, J. R.; *J. Chem. Phys.* **1986**, **84**, 3106.
10. Bracker, A. S.; North, S. W.; Suits, A. G.; Lee, Y. T. *J. Chem. Phys.* **1998**, 109, 7238.
11. North, S. W.; Marr, A. J.; Furlan, A.; Hall, G. E. *J. Phys. Chem. A* **1997**, 101, 9224.
12. Hawkins, W. G.; Houston, P. L.; *J. Chem. Phys.* **1982**, 76, 729.
13. Andresen, P.; Ondrey, G. S.; Titze, B.; Rothe, E.W.; *J. Chem. Phys.* **1984**, 80, 2548
14. Carrington, T.; *J. Chem. Phys.*, **1964**, 41, 2012.
15. Krieger, W.; Hager, J.; Pfab, J.; *Chem. Phys. Lett.* **1982**, 85, 69.
16. Ashfold, M. N. R.; Simons, J. P. *J. Chem. Soc., Faraday Trans. I*, **1978**, 274, 280.
17. Busch, G. E.; Wilson, K. R. *J. Chem. Phys.* **1972**, 56, 3655.
18. Lahmani, F.; Lardeux, C.; Solgadi, D. *J. Chem. Phys.* **1982**, 77, 276.
19. Ondrey, G. S.; Kanfer, S.; Bersohn, R. *J. Chem. Phys.* **1983**, 79, 179.
20. Halpern, I. B.; Jackson, W. M. *J. Phys. Chem.* **1982**, 86, 3528.
21. Zacharias, H.; Geilhaupt, M.; Meier, K.; Welge, K. H. *J. Chem. Phys.* **1981**, 74, 218.
22. Slinger, T. G.; Bichel, W. K.; Dyer, M. J. *J. Chem. Phys.* **1983**, 79, 2231.
23. Naik, P.D.; Upadhyaya, H. P.; Awadhesh, K.; Sapre, A. V.; Mittal, J. P. *Chem. Phys. Lett.* **2001**, 340, 116.
24. Hunnicutt, S.S.; Waits, L.D.; Guest, J.A. *J. Phys. Chem.* **1991**, 95, 562.
25. Hunnicutt, S.S.; Waits, L.D.; Guest, J.A. *J. Phys. Chem.* **1989**, 93, 5188.

	<p><b>Prakash D. Naik</b> was born in 1959 in Karwar, India. He received his B.Sc. in Chemistry in 1980 from Karnataka University, Dharwar, India and M.Sc. in Chemistry in 1983 from University of Mumbai, India. He is currently working as a Scientific Officer in Radiation &amp; Photochemistry Division of Bhabha Atomic Research Centre, Mumbai, India. He received his Ph.D. degree in Chemistry from University of Mumbai in 1992. He worked for a period of 1.5 years at Institute of Physical Chemistry, University of Heidelberg, Germany in the area of photodissociation and reaction dynamics with Prof. J. Wolfrum during 1992–1993. His research interests focus on laser-induced dissociation dynamics involving small polyatomic molecules and kinetics of atmospherically important reactions in gas phase. His current research activity is extended to include interfacial structure and dynamics studies, using vibrational sum-frequency generation technique.</p>
	<p><b>Hari P. Upadhyaya</b> was born in 1965 in Guwahati, India. He received his B.Sc. in Chemistry in 1987 from North Eastern Hill University, Shillong, India and M.Sc. in Chemistry in 1990 from University of Delhi, India. He is currently working as a Scientific Officer in Radiation &amp; Photochemistry Division of Bhabha Atomic Research Centre, Mumbai, India. He worked for a period of 1 year at Institute of Physical Chemistry, University of Heidelberg, Germany in the area of photodissociation and reaction dynamics with Prof. J. Wolfrum during 1997–1998. Subsequently, he received his Ph.D. degree in Chemistry from University of Mumbai in 2001. In his post-doctoral studies, he worked with Prof. Tim K. Minton, Montana State University, USA for a period of 2 years, in the area of reaction dynamics using cross beam technique during 2004–2006. His current research interests focus on photodissociation and reaction dynamics involving small polyatomic molecules as well kinetics of atmospherically important reactions in gas phase. He is also interested in studies on interfacial structure and dynamics, using sum-frequency generation technique.</p>
	<p><b>Awadhesh Kumar</b> was born in 1964 in Bihar, India. He received his BSc in Chemistry in 1985 from University of Delhi, India and MSc in Chemistry in 1987 from Indian Institute of Technology, Kanpur, India. He is currently working as a Scientific Officer in Radiation &amp; Photochemistry Division of Bhabha Atomic Research Centre, Mumbai, India. He received his Ph.D. degree in Chemistry from University of Mumbai in 1995. He worked for a period of 2 years at National Tsing Hua University, Hsinchu, Taiwan with Prof. Yuan Pern Lee. His research interests focus on dynamics of gas phase reactions induced by lasers using resonant four-wave mixing, laser-induced fluorescence and resonance-enhanced multiphoton dissociation with special reference to atmospherically important free radical species. Recently, he has extended his work to understanding the structure and dynamics at interfaces employing a nonlinear sum-frequency generation technique.</p>

## Hydrogen Energy

“I believe that water will one day be employed as fuel, that hydrogen and oxygen which constitute it, used singly or together, will furnish an inexhaustible source of heat and light, of an intensity of which coal is not capable. I believe that when the deposits of coal are exhausted, we shall heat and warm ourselves with water. Water will be then coal of future.”

(Jules Vernes; 1870, L'ile Myste'rieux)

The prophecy of the great science fiction writer Jules Vernes is coming true after nearly one and half century. Hydrogen is now considered as the fuel of 21 st century and onwards. Several automobile companies have made models based on hydrogen fuel. In the city of Rickjavic, the capital of Iceland, buses are running on hydrogen fuel.

Hydrogen produced from water is a sustainable production system. Electrolysis: method of separating water into hydrogen and oxygen. Renewable sources can be used to power electrolyzers (wind, hydro, solar and tidal energy) to produce hydrogen. It is independent of petroleum products and is nonpolluting. The

by products of the fuel cell process are WATER & HEAT. High temp. fuel cell system can be set up as a co-generator, with the waste energy used for heating.

Hydrogen does not exist in nature like nitrogen or oxygen. It has to be generated from water or some other source. A common industrial process is steam reforming reaction in which water and methane react at 800-900°C to give hydrogen and carbon dioxide. The major source of hydrogen is water and available techniques to generate hydrogen from water are electrolysis, photolysis and thermolysis. Efforts are going on throughout the world to utilize solar energy to split water to generate hydrogen and oxygen. Thr general schematic of hydrogen generation and utilization as fuel is given in figure 1.

Hydrogen is known as perfect fuel, clean burning, non polluting, non green house. It is non exhaustible fuel source. Several photochemical methods have been tried out to split water in to hydrogen and oxygen. The photochemical cycle is given in figure 2.

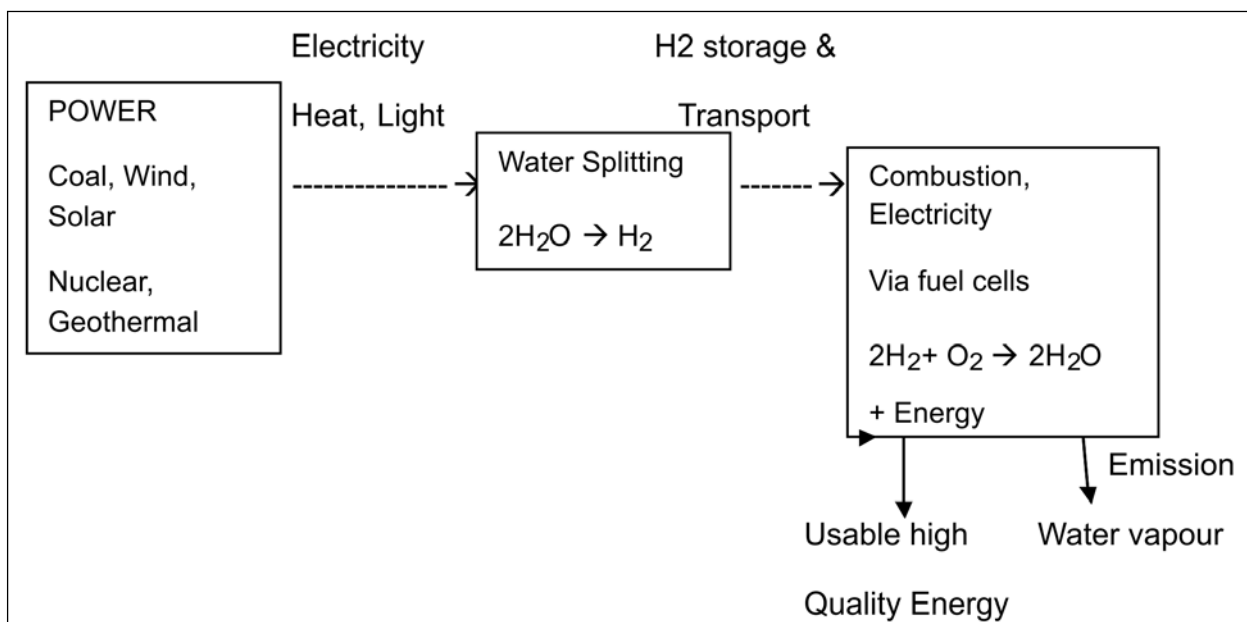


Figure 1

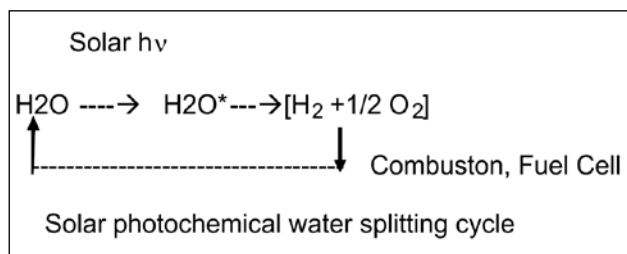


Figure 2

Some of these methods are given below.

- 1) Photooxidation of ferrous ions  
 $H\nu < 250 \text{ nm}$   
 $2\text{Fe}^{2+} + 2\text{H}_2\text{O} \rightarrow 2\text{Fe}^{3+} + 2\text{OH} + \text{H}_2$   
 Low molar extinction coefficient  $\sim 28 \text{ M}^{-1} \text{ cm}^{-1}$ , Energy requirement high  $> 2.5 \text{ eV}$   
 Impractical, mechanism; doubtful.
- 2) Photooxidation of ammonium sulfite  
 $(\text{NH}_4)_2\text{SO}_3 + \text{H}_2\text{O} \xrightarrow{-h\nu/\text{uv}} (\text{NH}_4)_2\text{SO}_4 + \text{H}_2$   
 No catalyst Efficiency UV  $\rightarrow \text{H}_2$  ; 30%  
 $\text{H}_2\text{O} + \text{SO}_3^{2-} \xrightarrow{-h\nu} \text{SO}_4^{2-} + \text{H}_2$   
 $\text{SO}_3^{2-} + \text{H}_2\text{O} \xrightarrow{-h\nu} \text{SO}_4^{2-} + \text{H}_2$   
 Sulfite; 0.8-1M; Temp; 50-70°C
- 3) Photocatalytic Decomposition:  $\text{TiO}_2$ :  
 Semiconductor, ( $\text{TiO}_2$  has 2 forms rutile and anatase)  
 Light absorption transfers electron from valance band to conduction band  $\lambda > 390 \text{ nm}$   
 $\text{TiO}_2 \xrightarrow{-h\nu} [\text{H}^+\text{vb} + \text{e}^- \text{cb}]$  ( $\lambda \sim 390 \text{ nm}$ ) Charge separation formation of hole & electron pair  
 $\text{H}^+\text{vb} + \text{H}_2\text{O} \rightarrow \frac{1}{4} \text{O}_2 + \text{H}^+$   
 $\text{H}^+ + \text{e}^- \text{CB} \rightarrow \frac{1}{2} \text{H}_2$

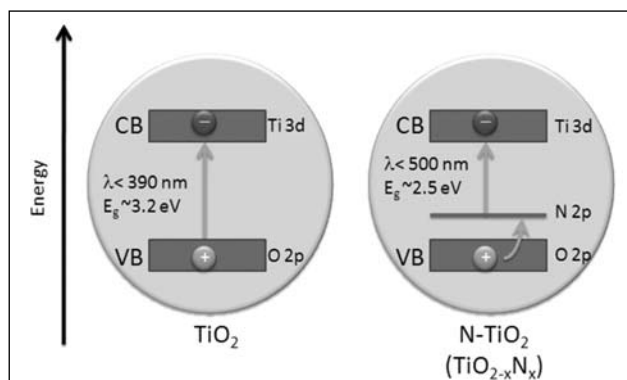


Figure 3

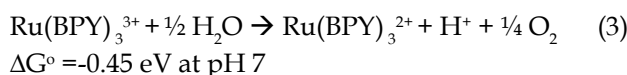
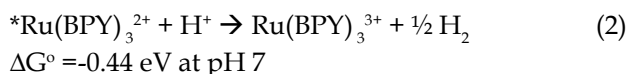
The semiconductor particles are doped with some atoms e.g. nitrogen (figure 3) to decrease the band gap so that visible light can be used to split water molecules.

4) Other photocatalytic systems being tried are as follows;

- a)  $\text{NaTiO}_3$ ;La b)  $\text{K}_2\text{Ta}_3\text{B}_2\text{O}_{12}$  c)  $(\text{Ga}_{0.82}\text{Zn}_{0.18})$   
 $(\text{N}_{0.82}\text{O}_{0.18})$  d)  $\text{Pt}/\text{TiO}_2$
- e) GaN-Sb Alloy f) silicon nanocrystals g) Cobalt based systems

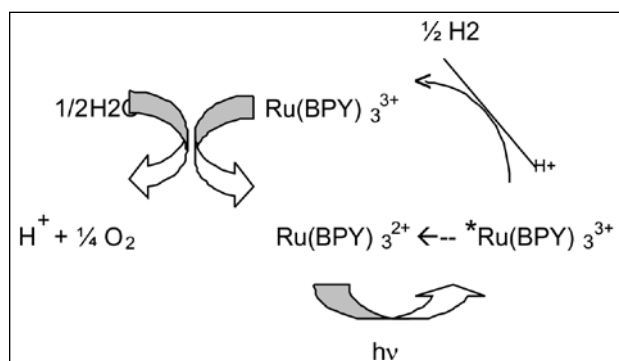
e.g. Rurhenium bipyridyl complex

This complex absorbs in the visible region and can utilize good fraction of solar radiation. Its excited state is good reductant. Hence it can reduce  $\text{H}^+$  to H atom.



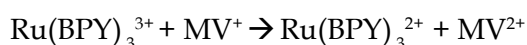
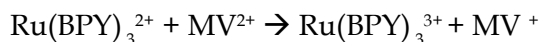
The  $\text{Ru}(\text{BPY})_3^{3+}$  species generated is strong oxidant to oxidize water.

In a cyclic way this can be represented as;



The cyclic process does not work since the reaction 1 is slow due to 2 electron nature of the reaction and short lifetime (microsecond times) of  $\text{*Ru}(\text{BPY})_3^{2+}$

To overcome this problem and to prolong the lifetime of the complex another species (Methyl Viologen  $\text{MV}^{2+}$ ) is added.



This type of cyclic process would be useful.

In some cities like Reykjavik (Iceland), Amsterdam (Netherlands), Hamburg & Stuttgart (Germany), Barcelona & Madrid (Spain) Porto (Portugal), Stockholm (Sweden) etc. buses have been running on hydrogen energy. In Denmark, Japan, Australia etc. experimental hydrogen stations are already operating. Hydrogen powered bicycles and scooters with fuel cells have been operating. They can run at 30KMPH for 70-100KM.

A typical schematic for combined wind, geothermal and solar powered generation of

hydrogen and its utilization is show below (Figure 4):

A large amount of work is being carried out in this direction throughout the world and soon solar energy is expected to form major source of energy in the world.

COMPILED BY

**A.V. SAPRE**

404/SERENADE/NEAR SYNGENTA BUILDING/BANER?PUNR 411045

**Information sources:**

1. V. Balzani, G. Bergamini, S. Campagna & Puntorieru,, Topics in Current Chemistry; Photochemistry of Co-ordination Compounds Vol.280 p 1-36.
2. K. Honda et al Bull. Chem Soc. Japan, 48 (1975) 1041.
3. P.N. Moorthy, J.P. Mittal, M.D. Karkhanawala, A.V. Sapre, T. Mukherjee, S.K. sarkar and P.V. Kamat; Proc. Nat. Solar Energy Convention Calcutta (1976) 131-4.
4. Avinash Sapre ISRAPS Bulletin: 18/1 & 2, 2006 p 72
5. Several internet sites: with grateful acknowledgement

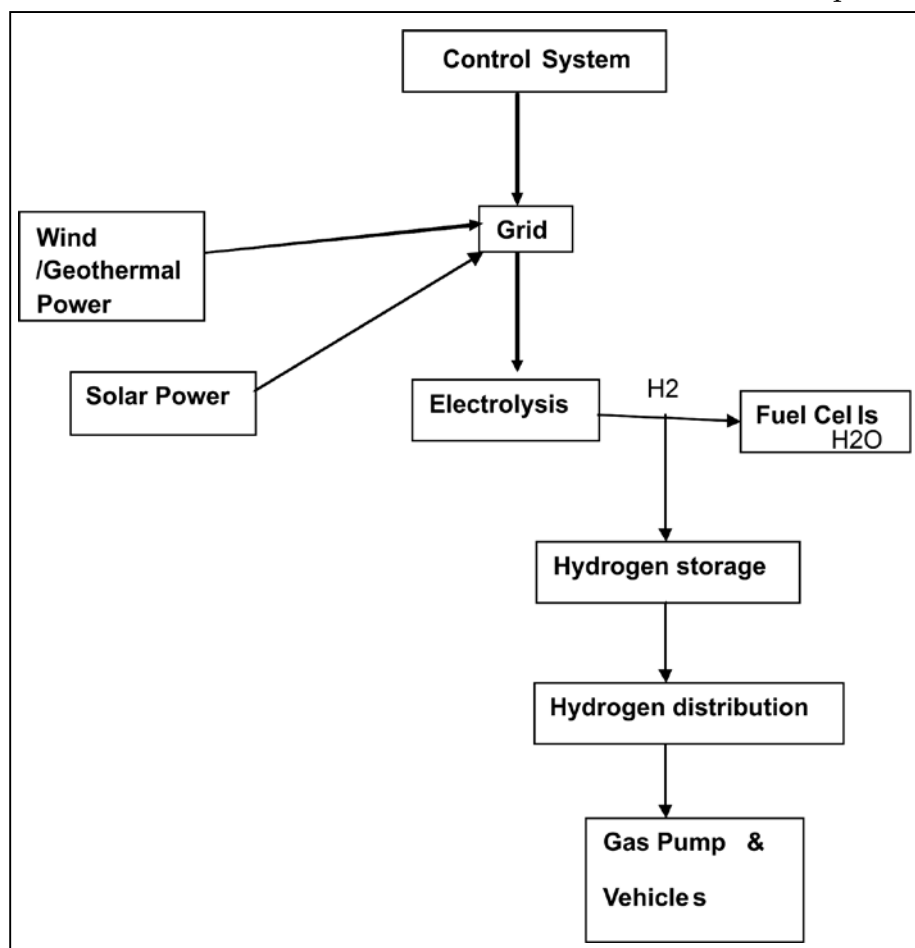


Figure 4



## Contents

Message from the President and Secretary, ISRAPS	1
Editor's Desk	2
Femtosecond Dynamics of Intramolecular Charge Transfer and Exciton Migration <i>Dipak K. Palit</i>	6
Femtosecond Stimulated Raman Spectroscopy: A potential tool to monitor chemical reaction dynamics <i>Ajay Jha &amp; Jyotishman Dasgupta</i>	16
Molecular Mechanism of DNA-Drug Intercalation: Structural and Dynamical Events, Role of Water and Entropy <i>Wilbee D. Sasikala and Arnab Mukherjee</i>	26
Laser Based Spectroscopic Techniques to Investigate Photodissociation Dynamics <i>Prakash D. Naik, Hari P. Upadhyaya, Awadhesh Kumar</i>	40
Hydrogen Energy	52

*Published by* ISRAPS, C/o RPCD, BARC, Mumbai 400 085